Virtual Model of Power Skiving Cutting Mechanics

by

Pierce McCloskey

A thesis
presented to the University of Waterloo
in fulfillment of the
thesis requirement for the degree of
Master of Applied Science
in
Mechanical and Mechatronics Engineering

Waterloo, Ontario, Canada, 2019

Author's Declaration

I hereby declare that I am the sole author of this thesis. This is a true copy of the thesis, including any required final revisions, as accepted by my examiners.

I understand that my thesis may be made electronically available to the public.

Abstract

Power skiving is a high-speed gear cutting operation which involves feeding a rotating cutting tool into a synchronously rotating workpiece at an angled orientation, creating a continual chip removal cutting action. It is capable of quickly machining both internal and external gears. The process has recently gained more interest from industry due to its potential to increase the productivity of gear manufacturing. However, power skiving is prone to vibrations and chatter, requiring stiff, well-controlled machine tools for effective implementation. Furthermore, methods for planning power skiving processes have not matured as much as those for more traditional machining processes, such as milling, turning, and drilling, which creates difficulties for its implementation.

Mechanistic models to predict cutting forces and other process outcomes have been widely used for traditional machining operations. These models can be invaluable in industry as tools to aid in the planning and optimization of cutting operations in order to maximize quality, minimize tool wear, and to reduce process time, among other measures of performance. The basis of these models is always the accurate prediction of cutting forces. This sort of modelling has not previously been performed for power skiving, and would be a valuable addition to research into the process.

The kinematics of power skiving are straightforward, but result in a complex cutting action. A power skiving process consists of multiple passes at set radial depths of cut. The workpiece and tool rotate as a pair of meshing gears, and the tool is fed axially along the width of the gear at a radial cutting depth. The tool is oriented at a cross-axis angle with respect to the workpiece so that the rotational motion results in the cutting edge being fed through the tooth gaps of the gear to remove material. Homogeneous transformation matrices are established to be able to represent points and vectors in a tool, workpiece, or machine coordinate system. A wide range of local cutting conditions occurs due to the relative velocity between the tool and workpiece, which has been calculated. The kinematics of power skiving are modelled and validated by comparing simulated tool positions with axial position data from the controller of a DMG NT5400 DCG mill-turn machine during experimental trials.

Cutting force predictions are made by applying the kinematics in a dexel-based cutter-workpiece-engagement engine to extract data representing a 3D uncut chip. The dexel data comprising the chip is then used to create a two-dimensional point cloud by intersecting the dexels and their outer contours with the established tool rake geometry. Delaunay triangulation is used on the point set to create a cross-section of the chip, with a set size threshold eliminating triangles that are unlikely to be part of the geometry. The chip geometry triangles are associated with points along the discretized cutting edge, and an oblique model using the local cutter geometry and relative velocity establishes the local cutting forces, their component directions (tangent, feed, and radial), and cutting angles (rake and inclination). The local cutting forces across the cutting edge are summed to create a total cutting force prediction. During experimental trials, data was captured using a wireless force measurement system and then filtered to reduce the noise. The measured cutting forces are compared to those produced by the model. It is found that predictions are made within 4–10% average RMS error, and 10–15% peak RMS error for cases where the tool geometry and coefficients are well defined. More trials are needed, however, to validate processes with thinner chips as well as helical and internal gears.

To reduce the computation time for simulation results, a partial workpiece simulation is used. A workpiece representing a single gear tooth gap is used in the simulation, and the results are processed using superposition to reconstruct the forces for a full cylindrical workpiece. While a 2–3% error was introduced (in numerically stable cases), in large part due to transient effects in the starts and ends of passes. This method reduced the simulation time by around 93%. The partial workpiece is then used to perform a simulation with alternating ramping-in and constant-depth passes on a wide workpiece. The results of this simulation establish a relationship between previous cutting depth, incremental cutting depth, and cutting parameters (in this thesis, the average total cutting force). With these relationships, new power skiving processes are planned by setting target thresholds and determining the incremental cutting depths. Planning was successfully performed to create processes with more consistent forces compared to the traditional planning approach, though more intelligent process limit targets are still being explored.

Acknowledgements

I would like to thank and acknowledge the contributions of the members of the Machine Dynamics group at the Advanced Manufacturing Research Centre of the University of Sheffield, especially Dr. Erdem Ozturk, Dr. Luke Berglind, and Mr. Steven Staley. In my time as an intern at the AMRC, I was able to gain valuable experience and knowledge relating to the practical implementation of power skiving under the skilled guidance of my colleagues there. As mentioned in this thesis, Dr. Berglind also contributed invaluable ideas for extensions to the virtual power skiving model.

I also want to thank Ontario Drive and Gear for the support and gear industry knowledge provided to me throughout the course of my research.

I would like to thank Mr. Andrew Katz, my colleague in the Precision Controls Lab at the University of Waterloo whose work was fundamental to my own. His work in modelling gear shaping formed the basis for my subsequent work into modelling power skiving, and his continual generous support and guidance for my work was crucial.

I would also like to thank both Professor Kaan Erkorkmaz and Professor Fathy Ismail for supervising this project. The ideas and direction provided by them in both the academic and research areas of my education have greatly aided me.

Finally, I want to thank all my colleagues in the Precision Controls Lab, my family, and my friends for their support and encouragement throughout my studies.

Dedication

To my parents and my sister.

Table of Contents

List of Figures . . . . . **xii**

List of Tables . . . . . **xiii**

Nomenclature . . . . . **xiv**

1 Introduction **1**
- 1.1 Power Skiving 1
- 1.2 Objective of Thesis 3
- 1.3 Outline of Thesis Topics 4

2 Literature Review **5**
- 2.1 Introduction 5
- 2.2 Modelling of Common Cutting Operations 6
- 2.3 Modelling of Gear Machining Operations 9
- 2.4 Power Skiving Research 11
  - 2.4.1 Tool Design and Sources of Error 11
  - 2.4.2 Modelling of the Power Skiving Process 12
- 2.5 Conclusions 12

3 Kinematics of Power Skiving **15**
- 3.1 Introduction 15
- 3.2 Gear Geometry and Terminology 16
- 3.3 Cutter and Workpiece Geometry 20
  - 3.3.1 Cutting Tool Geometry 20

3.3.2 Workpiece Geometry . . . 22
3.4 Kinematic Model . . . 23
3.4.1 Power Skiving Process Parameters . . . 25
3.4.2 Coordinate System Transformations . . . 28
3.4.3 Relative Cutting Velocity . . . 31
3.5 Validation of Kinematic Model . . . 34
3.6 Conclusions . . . 35

4 Cutting Force Prediction . . . 36
4.1 Introduction . . . 36
4.2 Cutting Force Model . . . 37
4.2.1 Orthogonal Cutting Model . . . 37
4.2.2 Oblique Cutting Model . . . 38
4.2.3 Orthogonal-to-Oblique Cutting Force Coefficients . . . 39
4.2.4 Kienzle Cutting Force Coefficients . . . 41
4.3 Cutter-Workpiece Engagement . . . 42
4.4 Cutting Tool Representation . . . 45
4.4.1 Tool Rake Geometry . . . 45
4.4.2 Discretized Cutting Edge . . . 47
4.4.3 In-Engine Tool Representation . . . 49
4.5 Uncut Chip Geometry . . . 51
4.5.1 Dexel Nail Intersection . . . 51
4.5.2 Contours of Dexel End Points . . . 53
4.5.3 Engaged Cutting Edge Nodes . . . 56
4.5.4 Triangulation of Point Cloud . . . 57
4.5.5 Uncut Chip Geometry Comparison . . . 59
4.6 Calculation of Cutting Forces . . . 59
4.6.1 Local Cutting Force Conditions . . . 59
4.6.2 Force Prediction in the Virtual Model . . . 64
4.7 Experimental Validation . . . 66
4.7.1 Experimental Trial Setup . . . 67
4.7.2 Data Processing of Force Measurements . . . 69

4.7.3 Determination of Cutting Coefficients . . . 73
4.7.4 Accuracy of Cutting Force Prediction . . . 78
4.8 Conclusions . . . 84

5 Process Planning Using Virtual Model . . . 85
5.1 Introduction . . . 85
5.2 Simulation Efficiency Improvement . . . 86
5.2.1 Cutting a Partial Workpiece . . . 86
5.2.2 Superposition of Partial Workpiece Results . . . 87
5.2.3 Results of Partial Workpiece Simulation . . . 89
5.3 Process Planning Using Gradual Radial Feed . . . 91
5.3.1 Gradual Radial Feed Simulation . . . 95
5.3.2 Interpretation of Results . . . 97
5.3.3 Force-Limited Process Planning . . . 101
5.3.4 Results . . . 105
5.4 Conclusions . . . 107

6 Conclusions and Future Work . . . 109
6.1 Conclusions . . . 109
6.2 Future Work . . . 111

References . . . 113

A Summary of Experimental Trial Parameters . . . 128

List of Figures

1.1 An overview of the motion and progression of an example power skiving process. 2

2.1 Force diagram for orthogonal cutting. 7
2.2 Z-buffer method to calculate cutter-workpiece engagement geometry. . 9
2.3 Cutter-workpiece engagement calculation for a shaper model using a dexel-based engine. 10
2.4 Power skiving chip geometry from CAD-based model 13
2.5 Measured (left) and predicted (right) total power skiving cutting forces by Spath and Hühsam. 13

3.1 Overview of basic gear tooth geometry definitions. 17
3.2 Normal and transverse planes of gear-equivalent spur and helical racks. 18
3.3 Effects of a profile shift on gear tooth geometry. 20
3.4 Examples of spur (left) and helical (right) power skiving cutters. . . . 21
3.5 Design angles on power skiving tools. 22
3.6 Definitions of workpiece representation geometry. 23
3.7 Overview of the kinematics for external and internal skiving. 24
3.8 Adjustment of rotation speed to cut helix angle. 27
3.9 Coordinate systems and their relationships in power skiving. 28
3.10 Cutting action from the rotation of the power skiving cutter. 32
3.11 Calculation of relative velocity of a point on the cutter tool. 33
3.12 DMG MORI NT5400 DCG mill-turn machine. 34
3.13 Simulated and measured axis commands (Trial 25). 35

4.1 Orthogonal cutting model. 38

4.2 Oblique cutting model. 39
4.3 Dexel representation of a shape in one and two directions. 43
4.4 Representation of tool and workpiece in the ModuleWorks engine. . . 44
4.5 Results of linear and spherical linear tool position interpolation. . . . 44
4.6 Extraction of dexel representation of uncut chip geometry. 45
4.7 Rake geometry of the cutting tool. 46
4.8 Generation of the cutting edge of a spur power skiving tool. 48
4.9 Generation of the cutting edge of a helical power skiving tool. 50
4.10 Triangular representation of cutting tool. 51
4.11 Dexel nail intersection with tool rake geometry. 52
4.12 Poor estimation of cross-section geometry using only nail intersections. 54
4.13 Procedure to generate outer contours in xy plane. 55
4.14 Improved cross-section geometry estimation with outer contour. . . . 55
4.15 Creation and intersection of uncut chip contours from dexel end points. 56
4.16 Triangulation of chip geometry points and association with nearest nodes. 58
4.17 Comparison of collected and simulated chip geometry for Trial 20. . . 60
4.18 Oblique cutting model applied to tool cutting edge. 61
4.19 Approximation of local rake vector angle on a conical tool face. . . . 63
4.20 Cutting force component directions along cutting edge. 65
4.21 Local rake and inclination angles during one tooth pass. 65
4.22 Cutting force predictions generated during simulation. 66
4.23 Experimental setup for power skiving cutting force measurement. . . 67
4.24 Workpiece geometry for power skiving trials. 68
4.25 Overview of the SPIKE system and its dimensions. 69
4.26 SPIKE system bending moment, torque, and force readings (Trial 8). 70
4.27 Initial calculated force measurements from the SPIKE system (Trial 8). 72
4.28 Drift compensation for SPIKE z-axis measurements (Trial 20). 74
4.29 Processed force measurements from SPIKE data (Trial 8). 75
4.30 Peak force discrepancies using the orthogonal-to-oblique cutting model (Trial 8). 76

4.31 Comparison of simulated and measured cutting forces for Trial 7. . . 80
4.32 Comparison of simulated and measured cutting forces for Trial 8. . . 82
4.33 Comparison of simulated and measured cutting forces for Trial 20. . . 83

5.1 Partial workpiece used to decrease CWE computation time. 87
5.2 Comparison of cutting force predictions from partial and full workpiece simulation for Trial 8. 88
5.3 Method of using partial simulation to estimate full simulation cutting force results. 90
5.4 Comparison of cutting force predictions from full and partial workpiece simulations for Trial 8. 92
5.5 Radial feed scheme for process planning. 96
5.6 Total cutting force during ramp-in simulation. 98
5.7 Average total cutting force results from process study. 98
5.8 Average total cutting force as a function of incremental cutting depth. 100
5.9 Linear fit of ramp-in and constant depth data. 101
5.10 Average linear fits for ramp-in simulation data. 102
5.11 Total cutting force during a traditionally-planned process (Trial 6). . 103
5.12 Procedure to develop a force-limited cutting scheme. 104
5.13 Total cutting force from planned force-limited processes (Trial 8). . . 107
5.14 Total cutting force from planned force-limited processes with force-per-chip-width constraint (Trial 20). 108

List of Tables

4.1 Cutting coefficients used for simulation of experimental trials. 79
4.2 Summary of prediction accuracy for Trial 7. 79
4.3 Summary of prediction accuracy for Trial 8. 81
4.4 Summary of prediction accuracy for Trial 20. 84

5.1 Prediction differences due to partial workpiece simulation. 93
5.3 Comparison of full and partial simulation times. 94
5.4 Example limits used for process planning. 106

A.1 Workpiece parameters for power skiving trials. 129
A.2 Tool parameters of experimental power skiving trials. 129
A.3 Kinematic parameters of power skiving trials using Dathan tool. . . . 130
A.4 Kinematic parameters of power skiving trials using Sandvik tool. . . . 137

Nomenclature

Symbol	Description	Unit
α_n	Normal / local rake angle	$^\circ$
α_r	Rake angle	$^\circ$
A	Undeformed chip area	mm^2
β	Helix angle	$^\circ$
b	Gear width / undeformed chip width	mm
$\gamma_{n/t}$	Normal / transverse pressure angle	$^\circ$
$d_{0,i}$	Total cutting depth of previous pass	mm
d_c/d_i	Total cutting depth of a power skiving pass	mm
d_{cg}	Distance between tool and workpiece centres	mm
Δd_i	Incremental cutting depth of a pass	mm
$d_{p/b/a/d}$	Pitch / base / addendum / dedendum diameter	mm
ϵ	Gear type indication; $+1$ for external, -1 for internal	
h	Uncut chip thickness	mm
$h_{a/d}$	Addendum / dedendum height	mm
i	Inclination angle	$^\circ$
η	Chip flow angle	$^\circ$
$\theta_{c/g}$	Cutter / workpiece rotation	$^\circ$
K_{tc}, K_{fc}, K_{rc}	Oblique model cutting coefficients	$\frac{\mathrm{N}}{\mathrm{mm}^2}$
K_{te}, K_{fe}, K_{re}	Oblique model edge coefficients	$\frac{\mathrm{N}}{\mathrm{mm}}$
K_u, u, K_v, v	Kienzle model cutting coefficients	–

Symbol	Description	Unit
$m_{n/t}$	Normal / transverse gear module	mm
N_c/N_g	Number of cutter / gear teeth	–
$r_{p,b,a,d}$	Pitch / base / addendum / dedendum radius	mm
Σ	Cross-axis angle	°
t_p	Time between consecutive cutting tooth passes	mm
v_c	Cutting speed	$\frac{\text{m}}{\text{min}}$ or $\frac{\text{mm}}{\text{sec}}$
v_f	Axial feed rate	$\frac{\text{mm}}{\text{WPR}^*}$
x	Profile shift coefficient	–
Ψ	Tool tilt angle	°
$\omega_{c/g}$	Tool / gear rotation speed	rpm or $\frac{\text{rad}}{\text{s}}$

*WPR = workpiece revolution

Chapter 1

Introduction

1.1 Power Skiving

Power skiving is a high-speed method of manufacturing gears that uses a toothed cutter (generally with an involute tooth profile) to rapidly machine the teeth of a desired gear. The tool and workpiece rotate in tandem at a high speed, which in conjunction with an angled orientation (the cross-axis angle) of the cutting tool to the workpiece creates a generative cutting motion (see Figure 1.1) to produce the desired gear geometry. Cutting is performed in several passes, wherein the tool is set at a radial cutting depth and fed axially along the face of the gear at a set feed rate.

Power skiving was originally developed and patented in 1910 [1], though only recently have advances in machine tool stability and control allowed the process to be more effectively implemented in industrial gear manufacturing. Compared to the two most common modes of gear machining – gear shaping and hobbing – power skiving has significant advantages. The cutting action results in continual material removal (in contrast to the interruption in cutting present in gear shaping) and the geometry of the tool and workpiece setup allows the manufacture of internal, external, spur, and helical gears (whereas the geometry of a hobbing tool precludes the creation of internal gears) [2]. It is estimated that, compared to shaping or hobbing, gears can be produced 2 – 10 times faster using power skiving [3–5].

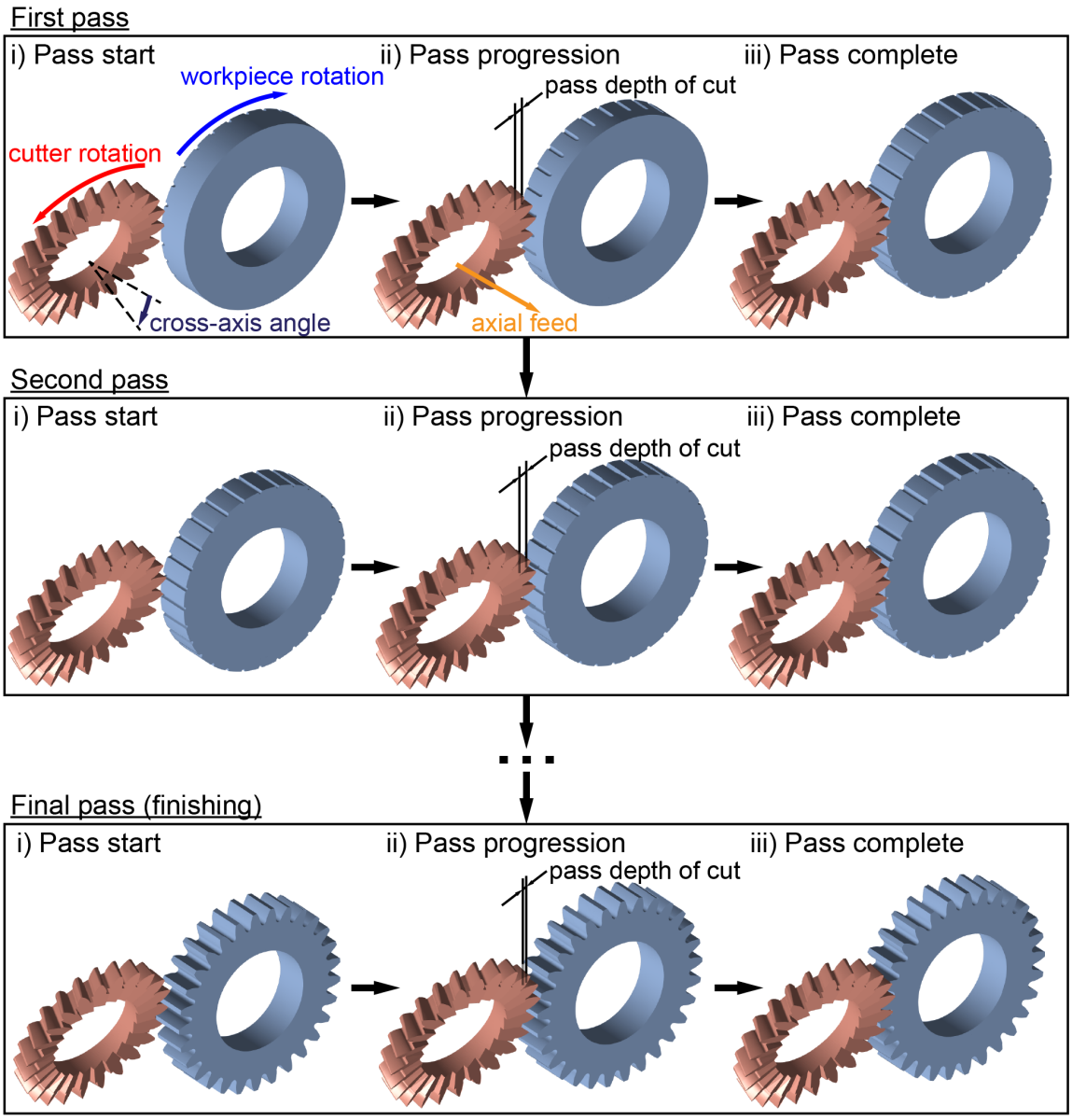

Figure 1.1: An overview of the motion and progression of an example power skiving process.

Research into the power skiving continues to find ways of overcoming the inherent technological challenges of the process, such as tool vibrations, servo motor synchronization, and tool life, and has generated further interest from within the gear machining industry [6]. Addressing these issues requires a fundamental understanding of the kinematics and cutting forces present during machining. However, due to the complexity of the kinematics and geometry of power skiving, analytical methods for investigating cutting forces and tool deflections are exceptionally difficult to implement. Therefore, an accurate virtual model would be the preferred tool used for the study of issues in the implementation of power skiving.

Virtual models of cutting processes such as power skiving are valuable for industry application. Using a virtual model to plan and optimize these processes avoids the time and expenses of trial-and-error methods of processes planning [7]. An extension of this application is the idea of the "digital twin", wherein the model is integrated into a virtual representation of a machine tool which is in turn paired with the sensor data of a real machine tool, allowing for both the monitoring and prediction of the machine tool's behaviour [8].

1.2 Objective of Thesis

The objective of this thesis is to research the cutting mechanics of power skiving for implementation in a virtual model. This model will be able to integrate the kinematics of a defined power skiving process to predict undeformed chip geometry, cutting forces, tool deflection, and chatter or forced vibrations. Furthermore, through the information obtained from the simulation of the process, the virtual model will be able to serve as a basis for future research on process planning, stability analysis and tool wear for gear machining via power skiving. The thesis is organized into sections based on the major topics covered by the research into the power skiving model.

1.3 Outline of Thesis Topics

A literature review is presented in Chapter 2, covering research related to the modelling of general machining, gear machining, and power skiving. The literature related to power skiving is further divided into topics relating to tool design and error influence, as well as work into mechanistically modelling the skiving process.

Chapter 3 covers the development of the kinematic model of power skiving. Geometric definitions of the tool-and-workpiece setup are described, and transformations between the tool, workpiece, and machine coordinate systems are developed using homogeneous transformation matrices using the specified system geometry. The relative velocity between the tool's cutting edge and the workpiece is also calculated.

In Chapter 4, the kinematic model is applied to a dexel-based discrete solid modelling engine. Undeformed chip geometry for each time step in the model is obtained in dexel format, and an approximated two-dimensional chip cross-section is determined. By applying the oblique cutting force model along the tool's edge, resulting force predictions are calculated for the power skiving process and compared to the measured cutting forces from a number of trials.

An initial process planning procedure is outlined in Chapter 5. First, the computational efficiency of the simulation is enhanced by using a partial workpiece to predict cutting forces for the cutting of a single tooth gap. The cutting forces for a full workpiece are then constructed using superposition. The partial workpiece is used in a process planning simulation, wherein the width of the desired workpiece is extended, and skiving passes are performed which alternate between a gradual radial feed into the gear and a normal pass with a set radial depth. Cutting forces and other results are then mapped based on a relationship between the total cut depth and the incremental cut depth of a pass. The mapped results are then used to predict theoretical results of a series of skiving passes, which allows for the planning of a power skiving process by setting one or more target values for the predicted cutting forces or other parameters.

Chapter 2

Literature Review

2.1 Introduction

The modelling of cutting processes is a broad topic in the field of machining research. In general, literature regarding these models has covered the application of analytical cutting force predictions, the modelling of elastic deformations and dynamic effects including vibrations, and the use of solid modelling engines to more accurately predict cutter-workpiece engagement. This work is often synthesized to create robust time-domain simulations of various machining operations. As an outcome, these cutting force models are able to be applied in industry to predict process stability, tool wear, tool life, and part quality, as well as to aid in process planning and optimization.

Research has traditionally focused on more common cutting processes, such as milling, turning, and drilling; however, recent work has been done to apply similar modelling methods to gear cutting process like gear shaping, hobbing, and power skiving. Despite its geometric and kinematic complexity as well as its relative lack of adoption in industry, power skiving is receiving increased attention in literature.

This chapter contains a review of relevant literature in the field of machining research. Section 2.2 covers the development of models for common machining processes such as milling, drilling and turning. Section 2.3 discusses how machining

models have been applied to gear cutting processes. Section 2.4 is a review of current research into the power skiving process, including tool design and its effects on error, kinematic and geometric analyses, and simplified mechanistic models.

2.2 Modelling of Common Cutting Operations

In order to correctly predict dynamics and final part quality, a process model must be able to accurately predict the cutting forces in the machining operation. Fundamental to this is the determination of uncut or undeformed chip geometry, which in many cases can be done analytically using the known cutter geometry and process kinematics. The chip geometry is then combined with a cutting model – for example the orthogonal cutting model as described by Merchant [9] or an oblique model using orthogonal test data [10] – and the known tool kinematics to calculate the cutting force estimate. Due to differing local geometry along the cutting edge, this procedure is generally performed along discretized sections of the cutting tool, and local cutting force predictions are summed to determine resultant total forces. This method of cutting force prediction has been successfully implemented for a number of common machining operations including end milling [11–14], face milling [15], drilling [16, 17], turning [18, 19], and boring [20]. Kaymakci et al. further proposed a unified model to cover these common cutting operations [21]. A similar methodology has also been implemented in more specialized processes such as multi-point thread turning [22] and orbital drilling [23]. Similar modelling work has been done to study forces in the more complex five-axis milling [24] and turn-milling [25] applications.

Cutting force predictions can be used to model tool deflections. This allows for the prediction of final part geometry and form deviations from a cutting operation, and can also increase force simulation accuracy by taking into account changes in uncut chip geometry due to the tool's deflection. Sutherland and Devor [26] as well as Armarego and Deshpande [27] used a flexible model of a milling tool to calculate deflection and the subsequent alteration of the chip thickness, with the former work showing an improvement in the surface error prediction. Smith and Tlustly [28] categorized this approach as "instantaneous force with static deflection feedback,"

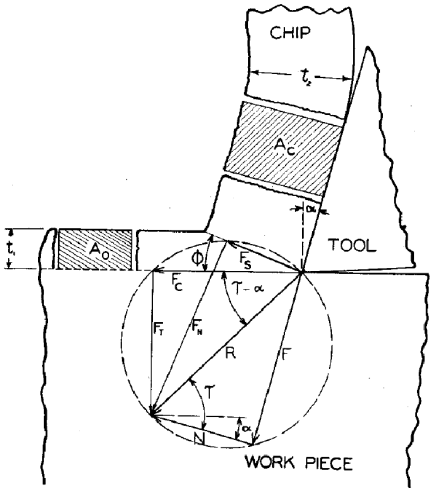

Figure 2.1: Force diagram for orthogonal cutting (from [9]).

and proposed a "regenerative force, dynamic deflection model" to be used in a time-domain simulation. This model represents the modal parameters of the cutter – as well as the workpiece and spindle, if parameters are known – as mass-spring-damper systems whose displacement responses are modelled based on the predicted cutting force, with the resulting surfaces being used in subsequent uncut chip geometry determination. This model allows dynamic and vibratory displacements to be modelled accurately. A similar method was used by Budak and Altintas [29] in combination with a milling tool modelled as a cantilevered beam, which was integrated with a flexible workpiece model developed by Altintas et al. [30] to create a time domain simulation which was compared against analytical chatter stability predictions for milling [31].

Understanding the dynamics of a machining operation is key for process planning, as forced vibrations and chatter can be encountered if an adverse set of process parameters is chosen. These vibrations result in poor surface quality on the final machined part as well as rapid tool wear development. Regenerative chatter, which is a self-excited vibration of the tool caused by subsequent cuts creating an increasingly oscillatory workpiece surface due to dynamic deflections [32], can be difficult to predict as it is heavily influenced by the specific geometry, kinematics, and pa-

rameters of a given process as well as the modal characteristics of the machine tool. Tlusty and Ismail produced time-domain simulations of vibrations in milling [33] and Tlusty et al. used the simulation approach to produce more accurate predictions of "stability lobes" [34] to determine the boundaries of stable cutting parameters. Time-domain simulations, however, are computationally expensive as they require small time steps to ensure numerical stability of the results. In general, analytical solutions are favoured for stability lobes due to the speed of computation. Dynamic models have been studied for a number of operations, including milling [35–38], drilling [39], turning [40], turn-milling [41], multi-point thread turning [42], and boring [43]. Kilic and Altintas further proposed a unified simulation model for metal cutting operations [44]. Extensions into special cases for milling have been studied as well, such as low-immersion milling [45] and milling considering a flexible tool and workpiece [46].

In classical process modelling literature, the uncut chip geometry is often determined analytically, generally using simplified representations of the real cutting tool geometry in order to reduce the complexity of the equations. With the advent of more powerful computers, however, the ability to use solid geometry modellers allowed researchers to extract more accurate representations of uncut chip geometry. In general, for discrete-time models, the chip geometry is extracted by using a swept volume generated by the modelled cutter movement, as described by Wang and Wang [47]. The interference between the swept volume and the workpiece volume is the uncut chip. There are a number of ways to represent the workpiece geometry, but the two main categories are exact solid modellers and discrete volume solid modellers. One exact modelling strategy is constructive solid geometry (CSG), where solids are represented by boolean combinations of primitive shapes such as spheres or boxes, which has been used in a number of papers investigating milling [48–51]. Another exact solid modelling method is boundary representation (B-rep), wherein the outer surfaces of a solid are described by equations, which has been used by Imani and Elbestawi in a similar milling study [52]. Mesh representation, such as that found in finite element method (FEM) simulation approaches, is a method of discrete workpiece representation using smaller volume elements, and has been used

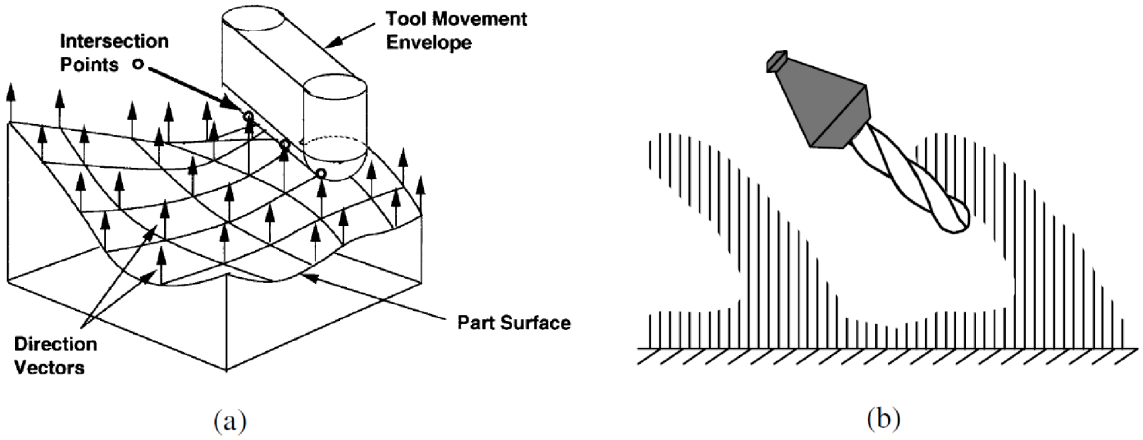

Figure 2.2: Z-buffer method to calculate cutter-workpiece engagement geometry (from [59]).

for focused modelling of cutting mechanisms by Limido et al. [53] and also to model flexible workpieces in a number of publications [54–56]. Kim et al. [57] as well as Lee and Ko [58] and Fussell et al. [59] have used the discrete Z map method of solid modelling, where vertically-oriented line segments describe the workpiece geometry (see Figure 2.2). An extension of the Z map method into three orthogonal directions, known as the dexel method, was studied by Hui [60] and has been implemented in research such as that by Boess et al. [61] and Berglind et al. [62]. Exact modelling, though accurate in the workpiece representation, is computationally expensive when determining the cutter-workpiece engagement. Discrete solid modelling approaches are usually faster, though a measure of accuracy is lost.

2.3 Modelling of Gear Machining Operations

One of the two most common gear cutting methods, hobbing, has been extensively studied for the estimation of cutting forces. Simulations with cutting force predictions have been developed by Abood [63], Bouzakis [64], and Komori [65], with the latter emphasizing the importance of avoiding chip crushing to reduce tool wear.

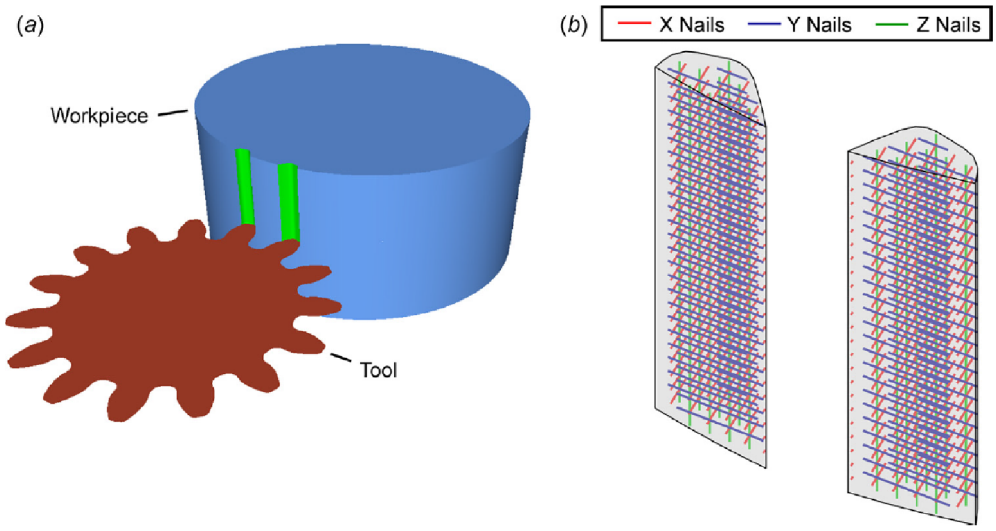

Figure 2.3: Cutter-workpiece engagement calculation for a shaper model using a dexel-based engine (from [74]).

Bouzakis later extended the developed hobbing model by coupling it with FEM simulation to more accurately model chip flow [66], while Tapoglou and Antoniadis used the same fundamental modelling approach and applied it in a computer-aided-design (CAD) solid modelling environment [67]. An FEM-based model to predict hobbing tool wear was also proposed by Dong et al. [68]. Klocke and colleagues used a unique chip geometry calculation by representing the workpiece as parallel planes, which was used to investigate tool wear [69], process design [70], final part quality [71], and online tool monitoring [72].

Despite its similarly widespread adoption in industry, gear shaping has not been the subject of much research in the field of process modelling. A dexel-based model was first proposed by Erkorkmaz et al. [73] in order to predict cutting forces in internal spur gear shaping. This work was later expanded by Katz to include helical and external cases [74, 75] (see Figure 2.3) as well as elastic deformations and final part quality predictions [76].

Other cutting mechanics research has been performed for less common gear manufacturing processes. Cutting forces for generative grinding were presented in research

by Klocke [77], Brecher [78], and Hübner [79]. Brecher and colleagues presented a number of works outlining the mechanistic modelling of bevel gear cutting [80–82]. More models of gear machining operations using similar cutting force prediction strategies as those presented above include gear broaching [83], gear shaving [84], gear form milling [85], face-hobbing [86], and gear honing [87].

2.4 Power Skiving Research

2.4.1 Tool Design and Sources of Error

Investigations into tool design and factors influencing geometric errors of the final workpiece are a common topic in power skiving literature. For these papers, the basic kinematics and geometry of the power skiving system are generally represented analytically. Guo et al. presented methods for tool correction by altering pressure angles [88] and later by using B-splines to define the cutting edge [89]. Guo et al. studied the inherent error in traditional skiving cutters and proposed a method to regrind the cutting edge to improve final part geometry [90]. A tool design defined by Shih defined the flank faces of the tool as having profile-shifted involute shapes with respect to the nominal cutting edge in order to reduce inaccuracy caused by regrinding the tool [91]. Tsai developed a mathematical model for defining the skiving cutter [92]. These novel tool adjustments and designs would improve the accuracy of the final gear geometry; however they are difficult to manufacture using current methods.

The effects of process parameters on final gear form errors are presented by Zheng et al. [93], who observed the theoretical error effects of changing tool offset, tool tilt, and cross-axis angle in a power skiving system. Similar research on errors due to tool offsetting was performed by Guo et al. [94]. Tachikawa demonstrated the effect of pitch runout of the skiving tool on the final quality of the part [95].

2.4.2 Modelling of the Power Skiving Process

A number of studies have developed process simulation models to study phenomena in power skiving. The kinematics of skiving have been studied in a majority of research papers about the operation, including the analysis of internal spur gear skiving presented by Kojima and Nishijima [96] and the rigid-body modelling of power skiving on a 6-axis mill-turn machine tool developed by Tsai and Lin [97]. Meshing equations commonly used for gear geometry definition are also used as a basis for the analysis of certain local cutting parameters on the cutting edge, such as the rake angle, clearance angle, and cutting depth, and the effects of process parameters on the local geometry. Such research has been published by Guo [98], Moriwaki [99], and Uriu [100]. Guo et al. [101, 102] integrated a solid modelling engine to perform similar analyses.

A number of process models and cutting force predictions for power skiving have been presented in literature. A three-dimensional FEM model was employed by Schulze et al. [103] to model the chip formation mechanism during a single cut of one tooth. Kimme et al. used a radially-oriented dexel-based solid modelling engine to find the final resulting workpiece in skiving [104] and Tapoglou used a CAD modeller similar to past hobbing research [105] (see Figure 2.4) to find uncut chip geometry; however, neither papers presented cutting force predictions for the process. Spath and Hühsam used a simplified force resultant force calculation to predict cutting forces based on the tool rotation [106] (see Figure 2.5). Tachikawa et al. used analytical methods to calculate normalized cutting forces in order to perform an analysis of the harmonics for vibration avoidance [107]. Klocke et al. used a planar workpiece representation to find uncut chip geometry in power skiving, and used the model results to compare the effects of altering process parameters [108].

2.5 Conclusions

Based on the literature review presented, there is a clear lack of a complete and accurate process model for gear power skiving. Cutting forces in power skiving have

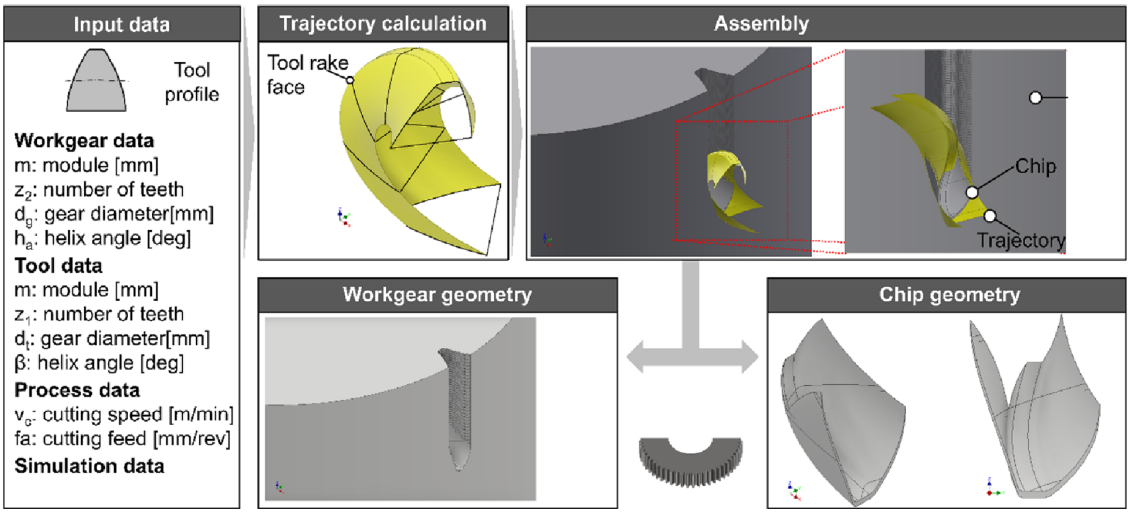

Figure 2.4: Power skiving chip geometry from CAD-based model (from [105]).

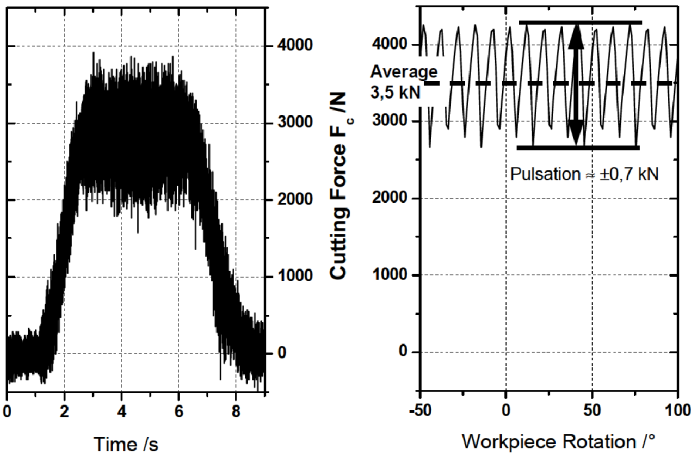

Figure 2.5: Measured (left) and predicted (right) total power skiving cutting forces by Spath and Hühsam (from [106]).

not been thoroughly studied and modelled, and additional effects such as elastic deformations and vibrations have not been analyzed. The virtual model described in this thesis, therefore, is a novel application of the mechanistic process modelling approach to power skiving, and there is also potential for future research into the various key aspects of the power skiving process to be derived from the model, such as the prediction of static and dynamic deflections, form error, and process stability.

Chapter 3

Kinematics of Power Skiving

3.1 Introduction

For any mechanistic model of a cutting operation, establishing the correct geometric and kinematic relationships between the workpiece and cutter is essential to achieving accurate process predictions. Key aspects of the establishment of a correct kinematic model include the accurate description of the tool and workpiece motion, the relationships between the tool, workpiece, and machine coordinate systems, and the relative velocity between the cutter and the part. Once properly defined, the kinematic model can be integrated with a mechanistic cutting model to obtain cutting force predictions.

The kinematics of power skiving are uniquely complex due to the synchronous rotations of the cutting tool and gear. Furthermore, differing machining cases (internal and external gears, helical and spur gears) require adjustments to be made to the kinematic model. A generalized description of the geometry, motions, and coordinate transformations covering the possible power skiving cases is thus necessary.

This chapter provides a full description of the geometric and kinematic derivations of the power skiving process for the virtual model. Section 3.2 provides an overview of gear terminology that will be used to describe the geometry of both the cutting tool

and workpiece of a power skiving system. Section 3.3 establishes the key geometric features of the two aforementioned components of the power skiving process. The kinematics of power skiving are described in detail in Section 3.4, and the subsequent validation of this model is presented in Section 3.5.

3.2 Gear Geometry and Terminology

As power skiving is a cylindrical gear cutting process, it is important to first establish basic gear geometry and its associated terminology to provide context for the derivation of power skiving geometry and kinematics. Fundamentally, cylindrical gears can be categorized as external or internal, and also as spur or helical. External gears are those which have teeth on the outer surface of a cylinder, and internal gears have teeth on the interior surface of a ring. Figure 3.1 shows basic gear geometry definitions and how these features differ for internal and external gears. A variable (ϵ_g) can also be established for later use with the skiving model to differentiate between the internal and external gear cases:

$$\epsilon_g = \begin{cases} 1 & \text{for external gear} \\ -1 & \text{for internal gear} \end{cases} \tag{3.1}$$

The teeth of spur gears run parallel along the rotating axis of the gear, while the teeth of helical gears follow a helical profile along the cylindrical surface of the gear. For helical gears, two planes are considered when analyzing the geometry – a transverse plane that is normal to the axis of rotation, and a normal plane that oriented perpendicularly to the helical profile of the gear teeth. The two planes are shown in Figure 3.2 using equivalent racks.

In general, the geometry for a gear is specified on the normal plane. The key parameters that define a gear are its normal module (m_n), number of teeth (N), normal pressure angle (γ_n), helix angle (β) and its face width (b). To be able to accurately model a gear, however, it is useful to be able to convert some parameters into the transverse plane.

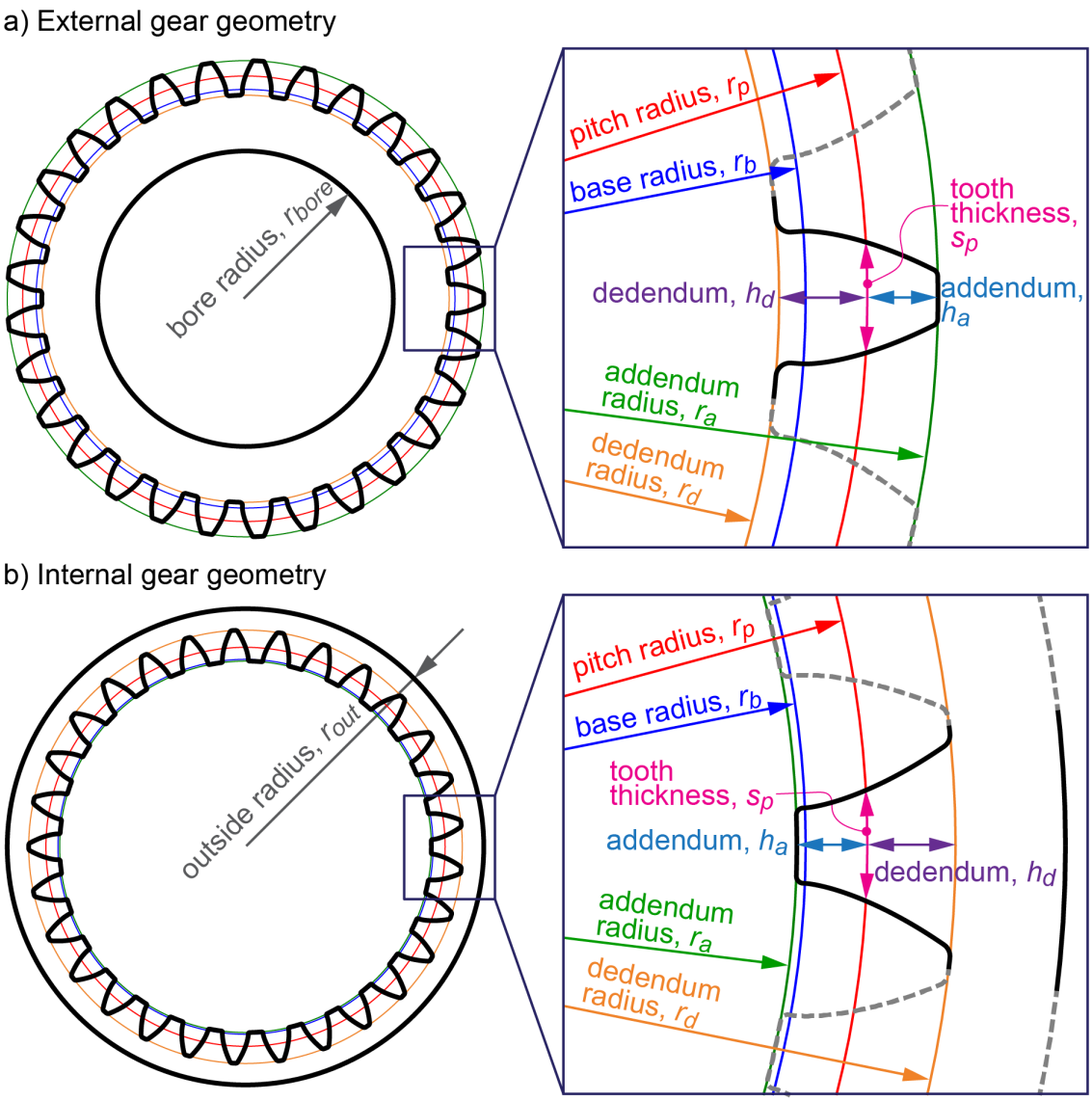

Figure 3.1: Overview of basic gear tooth geometry definitions.

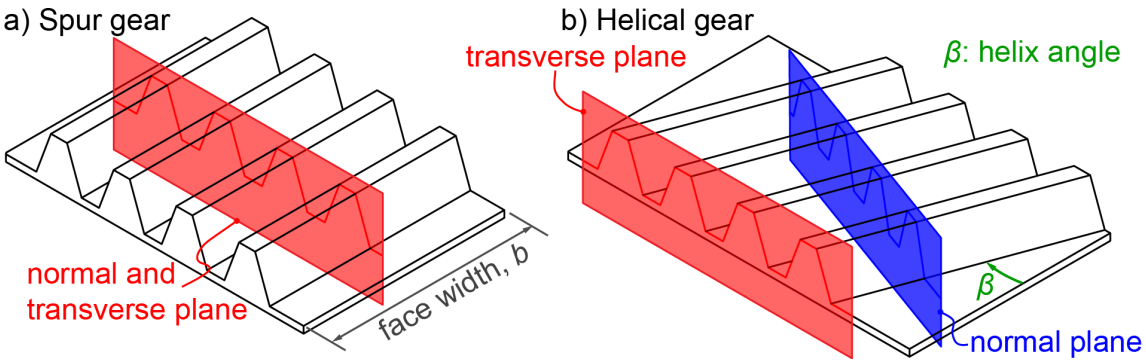

Figure 3.2: Normal and transverse planes of gear-equivalent spur and helical racks.

The normal module of a gear is a measure of the size of the gear and its teeth, in millimetres. The transverse module (m_t) of a gear can be calculated as follows:

$$m_t = \frac{m_n}{\cos\beta} \quad [109] \tag{3.2}$$

The pressure angle of a gear is the angle tangent to the tooth flank profile at the pitch radius (r_p). It affects the power transmission between two gears, and is generally limited to standard values. The transverse pressure angle (γ_t) can be determined as shown below:

$$\gamma_t = \tan^{-1}\left(\frac{\tan\gamma_n}{\cos\beta}\right) \quad [109] \tag{3.3}$$

The pitch radius (or diameter) is the nominal measurement of size used when designing a system of gears, as the pitch circles of paired gears are almost always aligned. The radius of the pitch circle is found using the specified module and number of teeth:

$$r_p = \frac{N m_t}{2} \quad [109] \tag{3.4}$$

The base circle on a gear is the position at which the flank profile curve (almost always the involute of the base circle) of a tooth begins. Its radius (r_b) is defined as a function of the pitch radius and the transverse pressure angle:

$$r_b = r_p \cos\gamma_t \quad [109] \tag{3.5}$$

The tip and root of each tooth are defined at the addendum circle and dedendum circle of the gear, respectively. The radius of each circle is determined by a corresponding radial offset from the pitch radius – either the addendum (h_a) or dedendum (h_d). For standard gear profiles, the values are $h_a = m_n$ and $h_d = 1.25m_n$ [110], but these can be modified depending on the use of the gear (for example, skiving cutters will often have adjusted values). The addendum radius (r_a) and dedendum radius(r_d) are calculated as follows:

$$r_a = r_p + \epsilon h_a \tag{3.6}$$

$$r_d = r_p - \epsilon h_d \tag{3.7}$$

The tooth flank profiles join the addendum and dedendum circles at the tooth tip and root, respectively. At these junctions, there are generally fillets with specified radii (r_{tip} and r_{root}).

Tooth thickness (s_r) for a standard involute gear is measured as an arc with a specified radius (r) between the two profile curves that make up one of the gear teeth:

$$s_r = r\left[\frac{s_p}{r_p} + 2\epsilon\left(\text{inv}\gamma_t - \text{inv}\left(\cos^{-1}\frac{r_b}{r}\right)\right)\right], \quad \text{where } r > r_b \quad [109] \tag{3.8}$$

The involute function (invγ) is the basis for the profile curve of an involute gear tooth, and is specified based on the pressure angle:

$$\text{inv}\gamma = \tan\gamma - \gamma \quad [109] \tag{3.9}$$

The profile of the teeth for a gear can be shifted from the nominal dimensions by specifying a profile shift coefficient (x). The profile shift will alter the tooth thickness and, subsequently, the pitch radius and working pressure angle, as illustrated in Figure 3.3.

The profile shift changes the nominal tooth thickness at the pitch circle (s_p) with a simple multiplication of the profile shift coefficient:

$$s_p = \frac{\pi m_t}{2} + \epsilon 2x m_t \tan\gamma_t \quad [109] \tag{3.10}$$

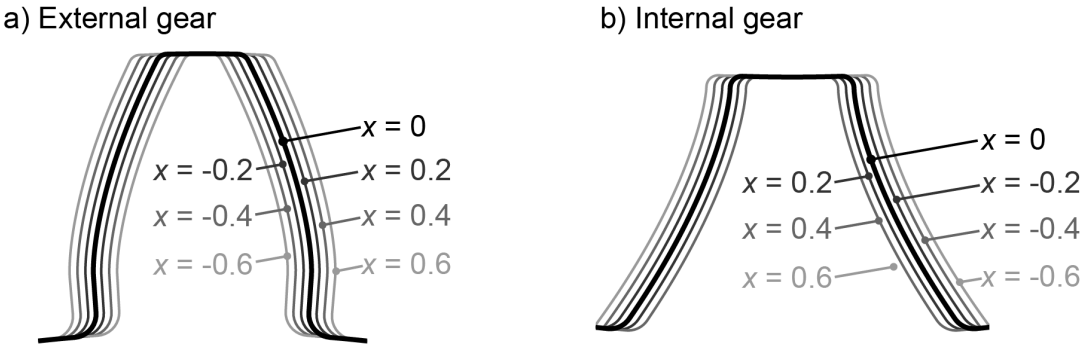

Figure 3.3: Effects of a profile shift on gear tooth geometry.

Since the process of power skiving includes both a cutter and workpiece that are defined using typical gear geometry, their geometric definitions must be delineated through notation. In this thesis, gear geometry definitions with the subscript c refer to the cutter, and those with the subscript g refer to the workpiece. As an example, the addendum radius of the cutter is notated as (r_{ac}) and the addendum radius for the workpiece would be (r_{ag}).

3.3 Cutter and Workpiece Geometry

3.3.1 Cutting Tool Geometry

Conventional power skiving tools generally have the same nominal geometry as a gear shaping tool [6], in that the cutting tool is essentially an external gear with modifications that make it suitable for machining. The module of the cutting tool must be that of the desired gear, and the number of teeth on the cutter is generally chosen to not be a multiple of the number of gear teeth. Skiving cutters may be spur or helical, as shown in Figure 3.4, which affects the geometry of the rake (front) face of the tool. Spur cutters have a conical rake face, whereas helical cutters have a planar rake face for each cutting tooth.

In general, the cutting teeth have an involute profile with additional modifications

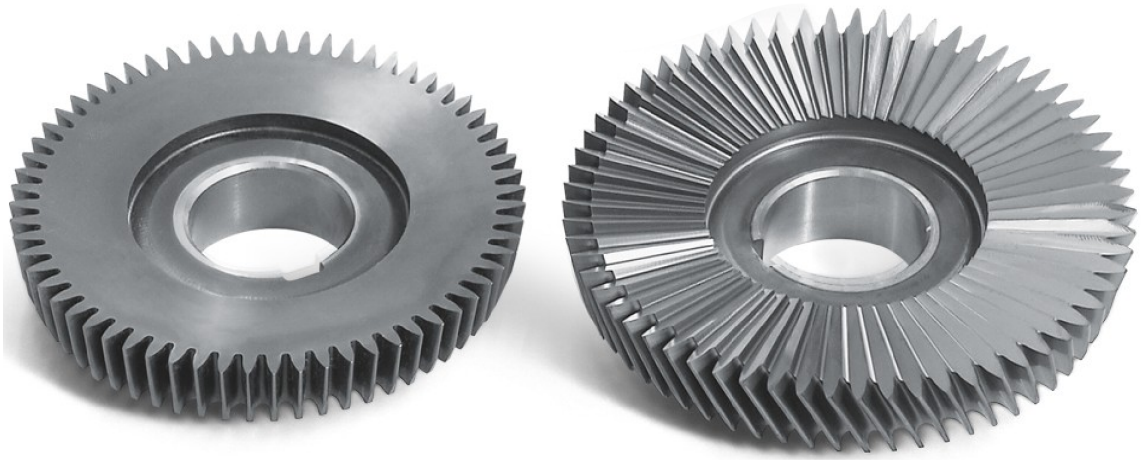

Figure 3.4: Examples of spur (left) and helical (right) power skiving cutters (from [111]).

made to enable correct cutting without interference. A clearance angle on the outside diameter of the tool – otherwise referred to as the top relief angle – can be present (α_t), creating a conical tool shape. Without the outer clearance angle, the tool will be cylindrical, and clearance must be created with a tilt angle when setting up the cut. The addition of a tilt angle will be defined in Section 3.4. The sides of each tooth will also have clearance angles (α_s) to avoid the flanks of the cutting teeth rubbing against the flanks of the workpiece teeth. For both the spur and helical cutter cases, a rake angle (α_r) will be present on the rake face geometry, which alters the local cutting conditions as the cutting teeth engage with the workpiece. The planar rake geometry of a helical cutter will have an additional angle equal to the helical angle of the tool. Figure 3.5 shows these angles as applied to a power skiving tool.

As was mentioned in Chapter 2, much research has been performed regarding the reduction of error by cutter geometry modification in power skiving, as the use of nominal gear geometry introduces inherent geometric errors into the skiving process [90]. Therefore, modelling a skiving tool accurately may involve further alterations to the tooth geometry, such as adjusting the pressure angle or adding a profile shift.

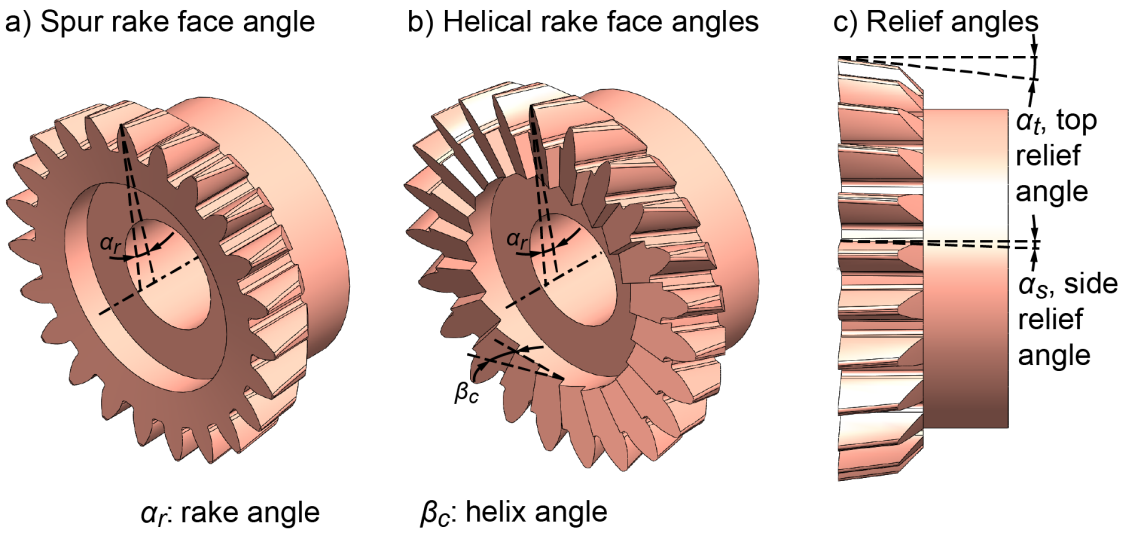

Figure 3.5: Design angles on power skiving tools.

3.3.2 Workpiece Geometry

In practical applications, gears can be machined as features on parts with more complex geometry, such as on the end of a shaft or with additional mounting features. For the virtual model, however, only the working area of the gear needs consideration. For external gears, this is represented as a cylinder with an outer radius equal to the addendum radius of the final gear and with a height equal to the width of the gear face. A cylindrical bore in the centre (with radius r_{bore}) of the gear may be modelled as well, as long as its radius is less than that of the gear's dedendum. For internal gears, the workpiece is constructed as a cylinder with a large internal bore – in other words, as a ring – where the internal radius is equal to the addendum radius of the gear and the outer radius of the ring (r_{out}) is larger than the dedendum radius of the gear. Figure 3.6 provides an overview of the dimensions of workpiece representations in the model.

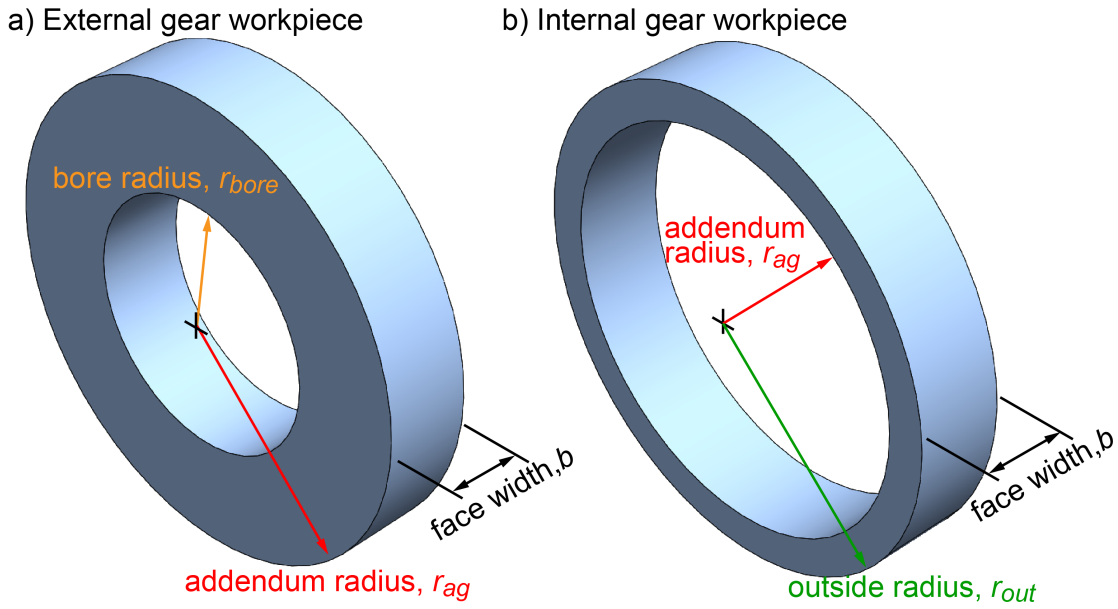

Figure 3.6: Definitions of workpiece representation geometry.

3.4 Kinematic Model

In order to model the cutting forces of power skiving, its kinematics must first be correctly established. Power skiving is a multiple-pass process, wherein a portion of the final gear tooth geometry is cut during each pass. Figure 3.7 demonstrates the basic kinematic concepts for power skiving internal and external gears.

In the power skiving setup, three coordinate systems are established – the machine coordinate system (MCS), the workpiece coordinate system (WCS), and the tool coordinate system (TCS). The machine coordinate system is the stationary global coordinate system that can be used to establish the positions and kinematics of the workpiece and cutter. The workpiece coordinate system – whose point of origin is established to be coincident with that of the MCS – rotates with the gear and is used for calculating cutter-workpiece engagement in the solid modelling engine. The tool coordinate system rotates and translates with the skiving cutter and is used for defining the cutting tool geometry, establishing force predictions using a mechanistic model, and measuring cutting forces during trials.

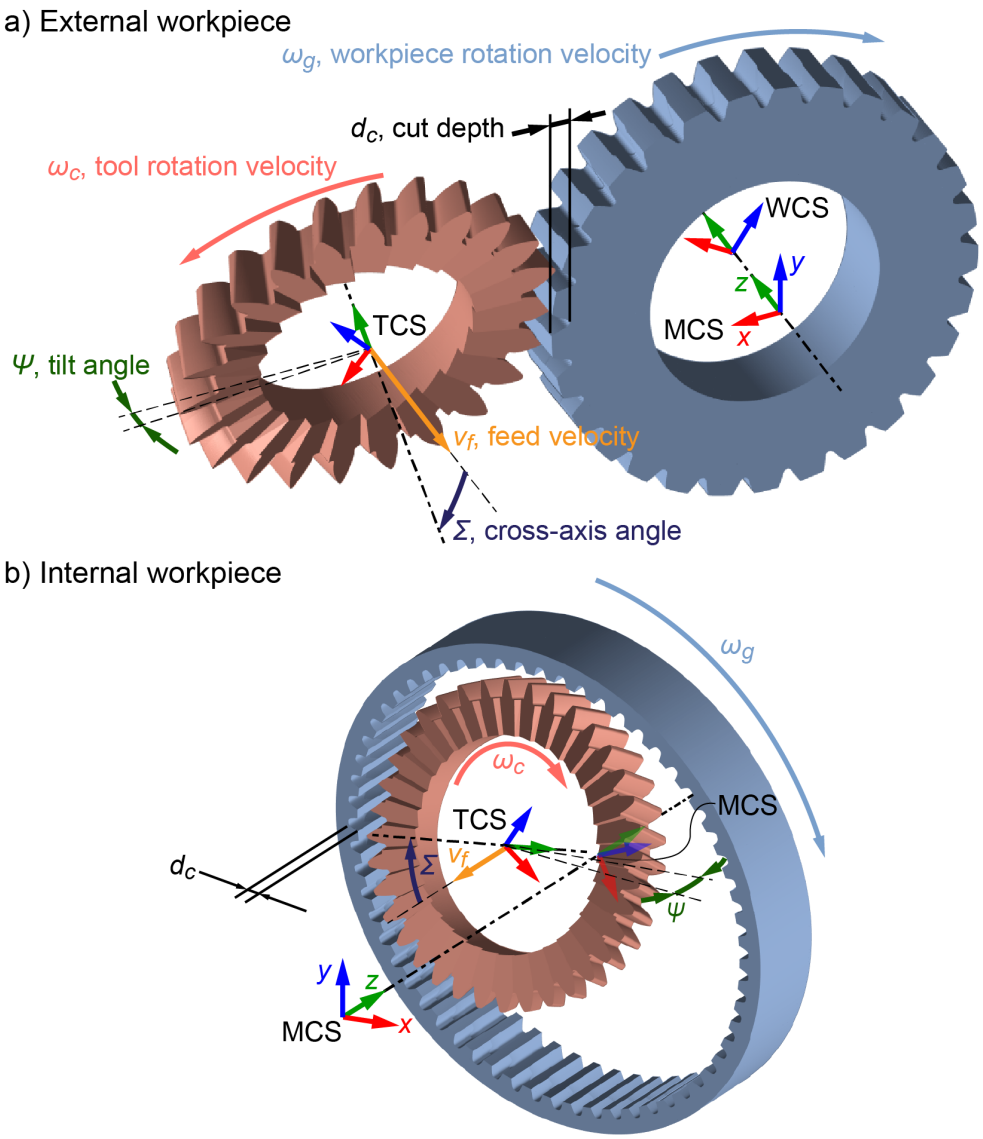

Figure 3.7: Overview of the kinematics for external and internal skiving.

3.4.1 Power Skiving Process Parameters

The power skiving cases presented in Figure 3.7 show the main process parameters that must be defined to describe the power skiving setup. For every cutting pass, the cutting tool is set in a position to cut a certain radial depth into the workpiece (d_c). More specifically, the set depth can include a radial cutting depth, assumed to be along the x axis of the MCS (d_{cx}) and a tangential or lateral offset, assumed to be along the y axis of the MCS. This lateral offset can be used to change the cutting conditions for a given pass [6]; however, the effects arising from this are not studied for the purposes of this model, and the cutting depth is always assumed to be purely in the radial direction (ie., d_{cx}).

The reference position for the tool is defined to be the "scraping distance" (r_{scrape}), which is the radial position along the x-axis of the MCS where the addendum diameters of the cutter and workpiece contact tangentially, such that no cutting is performed. The scraping distance is defined as:

$$r_{\text{scrape}} = r_{ag} + \epsilon_g r_{ac} \tag{3.11}$$

The total cutting depth for each subsequent pass will increase until the final depth of cut is reached (d_{ct}), which will position the tool at the final radial location (r_{end}). This is defined as shown below:

$$r_{\text{end}} = r_{pg} + \epsilon_g r_{pc} = r_{\text{scrape}} - \epsilon_g d_{ct} \tag{3.12}$$

For each pass, the tool begins axially at a clearance distance from the top of the workpiece (z_{top}). As the tool and workpiece rotate, the tool moves axially along the width of the workpiece at a constant feed velocity (v_f) in the z axis of the WCS (and the MCS) until it reaches a clearance distance from the bottom of the workpiece (z_{bottom}). The total stroke length (d_{zt}) is the distance that the tool travels axially along the workpiece for each pass, and is defined as:

$$d_{zt} = |z_{\text{top}}| + b_g + |z_{\text{bottom}}| \tag{3.13}$$

The tool is oriented at a cross-axis angle (Σ) about the x axis of the MCS. The cross-axis angle is also referred to as the shaft angle and is constant for a given tool-workpiece pair, as the angle is required for the two to correctly mesh. The absolute magnitude of the resulting cross axis should generally be greater than 10° to ensure sufficient cutting speed [6]. The angle is a function of the cutter and workpiece helix angles:

$$\Sigma = -\left(\beta_g + \epsilon_g \beta_c\right) \tag{3.14}$$

When planning a skiving process, the nominal rotational speed of the cutting tool is selected based on the desired cutting speed. It is the combination of this tool rotation and the previously defined cross-axis angle that creates the cutting motion. The magnitude of the nominal cutter rotation speed (ω_c) is selected based on the material being cut, the dimensions of the cutter and gear, and, if known, the modal parameters of the tool spindle and workpiece. The direction of the rotation, in the TCS, is based on the orientation of the tool due to the cross-axis angle, and the full expression for the cutting speed is derived as follows:

$$\omega_c = -\frac{\Sigma}{|\Sigma|}\,|\omega_c| \tag{3.15}$$

When cutting a helical gear, the cutter must follow the helical path of the tooth channel of the workpiece, as shown in Figure 3.8. This requires the rotation speed of the tool to be adjusted based on the axial feed velocity and the helix angle of the gear. The resulting total tool rotation speed is thus a function of the chosen nominal cutter speed and the rotation correction (ω_{cf}), calculated as follows:

$$\omega_{cf} = \epsilon_g \frac{v_f \tan \beta_g}{r_{pc}} \tag{3.16}$$

The total angular velocity of the cutting tool can then be expressed as a vector in the TCS by combining the rotation velocities from Equations (3.15) and (3.16):

$$\boldsymbol{\omega}_c = \begin{bmatrix} 0 \\ 0 \\ \omega_c + \omega_{cf} \end{bmatrix} \tag{3.17}$$

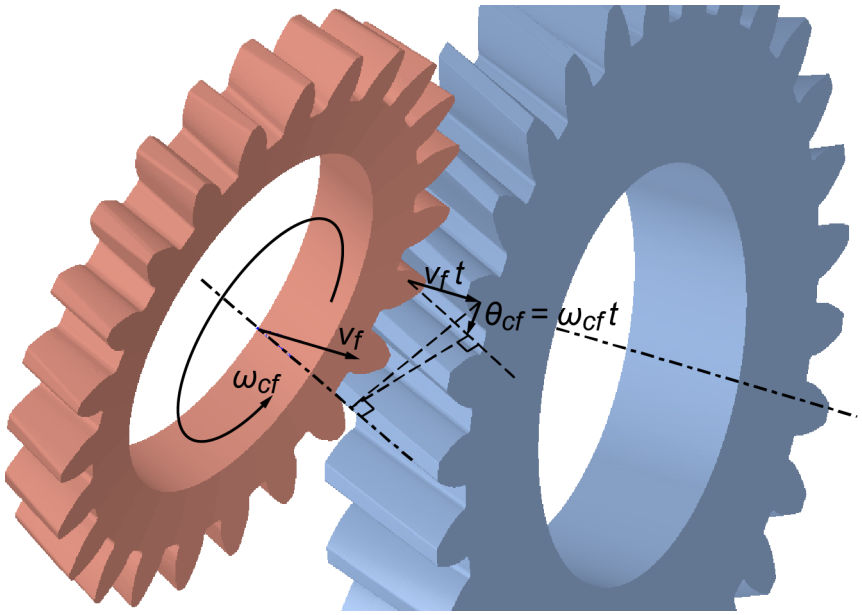

Figure 3.8: Adjustment of rotation speed to cut helix angle.

The angular velocity of the workpiece, in the WCS, is simply a function of the gear ratio and the nominal cutter speed, as shown below:

$$\boldsymbol{\omega}_g = \begin{bmatrix} 0 \\ 0 \\ \omega_g \end{bmatrix} = \begin{bmatrix} 0 \\ 0 \\ -\frac{N_c}{N_g}\epsilon_g \omega_c \end{bmatrix} \tag{3.18}$$

The orientation of the tool can additionally be adjusted with a tilt angle about the y axis of the MCS. The tilt angle can be used to create a profile modification to the resulting gear by changing the orientation of the cutting edge. The addition of a tilt can also be used to adjust both the clearance and rake angles of the cutting tool, which alters the nature of the cutting mechanics and can affect the cutting forces resulting from the process. Additionally, if the tool is cylindrical with no outer clearance angle, the tool must be tilted to provide the clearance. The direction of the tilt will depend on whether the gear is internal or external, and is defined as follows:

$$\Psi = \epsilon_g \left|\Psi\right| \tag{3.19}$$

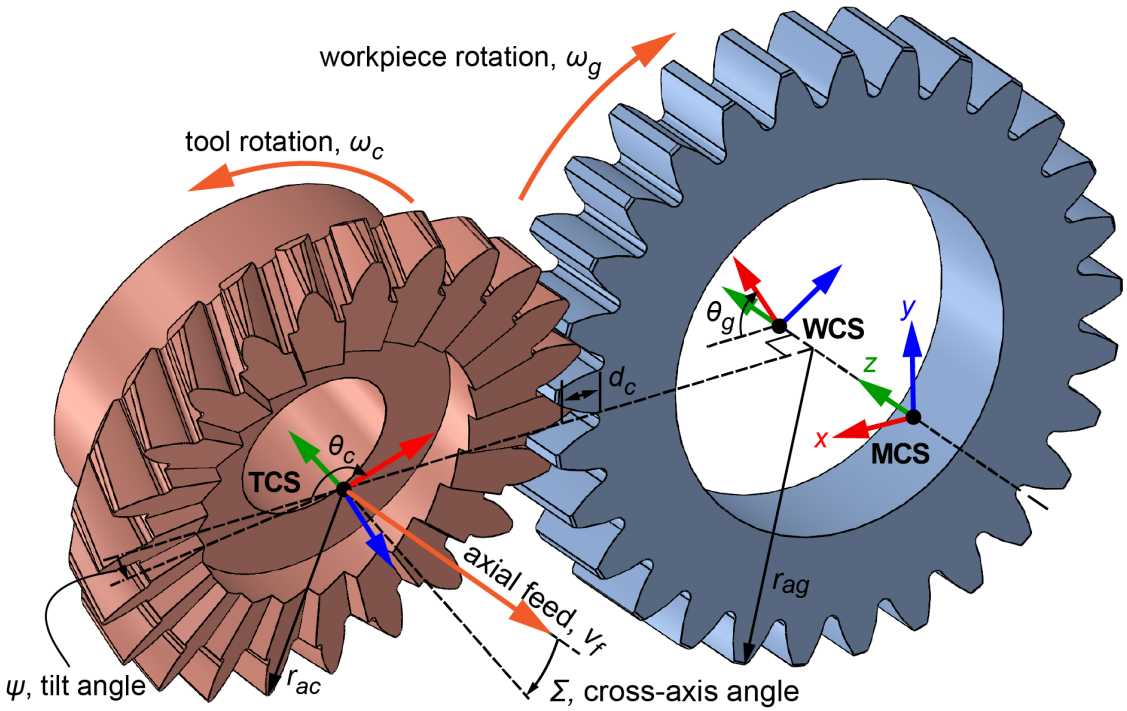

Figure 3.9: Coordinate systems and their relationships in power skiving.

3.4.2 Coordinate System Transformations

The ability to resolve geometric and kinematic features in any of the defined coordinate systems is important for determining cutting force predictions and other resulting process parameters. Figure 3.9 shows the positions and orientations of the cutter and the workpiece at a given time step, which demonstrates how the coordinate system transformations are derived.

The coordinate system transformations are accomplished using homogeneous transformation matrices. With the homogeneaus transformation matrix between two given coordinate systems known, it is possible to take any point expressed in one coordinate system and find its coordinates in a desired coordinate system. For example, the following equation calculates the coordinates of a point in the WCS (a

3-by-1 vector $\mathbf{p}^{\mathrm{WCS}}$) using its established position in the TCS ($\mathbf{p}^{\mathrm{TCS}}$):

$$\begin{bmatrix} \mathbf{p}^{\mathrm{WCS}} \\ 1 \end{bmatrix} = \mathbf{M}_{\mathrm{TCS}}^{\mathrm{WCS}} \begin{bmatrix} \mathbf{p}^{\mathrm{TCS}} \\ 1 \end{bmatrix} \tag{3.20}$$

First, the transformations from the WCS and TCS to the MCS are established. To transform between the rotational coordinates of the WCS to the stationary MCS, a matrix representing the workpiece rotation is established. Since the rotation of the workpiece changes throughout the power skiving process, its angle (θ_g) is expressed as a function of time which depends on the rotation speed previously established:

$$\theta_g(t) = \omega_g t \tag{3.21}$$

The rotation matrix for the WCS is thus defined as follows:

$$\mathbf{R}_{z,\theta_g} = \begin{bmatrix} \cos\theta_g(t) & -\sin\theta_g(t) & 0 & 0 \\ \sin\theta_g(t) & \cos\theta_g(t) & 0 & 0 \\ 0 & 0 & 1 & 0 \\ 0 & 0 & 0 & 1 \end{bmatrix} \tag{3.22}$$

As previously established, the point of origin is the same for both the WCS and the MCS. Therefore, the total transformation matrix to move from the WCS to the MCS is the rotation matrix defined in Equation (3.22):

$$\mathbf{M}_{\mathrm{WCS}}^{\mathrm{MCS}} = \mathbf{R}_{z,\theta_g} \tag{3.23}$$

Transforming between the TCS and the MCS is more complex due to the multiple rotations used to describe the tool's orientation, and several transformation matrices must be combined. A vector describing the distance from the origin point of the TCS (the tool centre) to that of the MCS (coincident with the workpiece centre) can be established as follows:

$$\mathbf{d}_{cg,\mathrm{MCS}}(t) = \begin{bmatrix} d_{cgx}(t) \\ d_{cgy}(t) \\ d_{cgz}(t) \end{bmatrix} = \begin{bmatrix} r_{\mathrm{scrape}} - d_{cx}(t) \\ d_{cy}(t) \\ z_{\mathrm{top}} - v_f t \end{bmatrix} \tag{3.24}$$

The distance vector is then used to create a translation matrix to move between the two centre points:

$$\mathbf{T}_{g\to c}^{\mathrm{MCS}} = \begin{bmatrix} 1 & 0 & 0 & d_{cgx}(t) \\ 0 & 1 & 0 & d_{cgy}(t) \\ 0 & 0 & 1 & d_{cgz}(t) \\ 0 & 0 & 0 & 1 \end{bmatrix} \tag{3.25}$$

A rotation matrix for the cross-axis angle rotation portion of the tool orientation is also defined:

$$\mathbf{R}_{x,\Sigma} = \begin{bmatrix} 1 & 0 & 0 & 0 \\ 0 & \cos\Sigma & -\sin\Sigma & 0 \\ 0 & \sin\Sigma & \cos\Sigma & 0 \\ 0 & 0 & 0 & 1 \end{bmatrix} \tag{3.26}$$

In order to retain the correct kinematic relationship between the cutter and workpiece, the tilt must be applied at the intersection of the cutter's addendum (at radius r_{ac}) with a line joining the centre axes of the cutter and workpiece. To do this, two translation matrices are introduced; $\mathbf{T}_{c\to r_{ac}}$ to move to the pivot point, and $\mathbf{T}_{r_{ac}\to c}$ to return to the centre of the cutter. The result, combined with the rotation matrix about the y axis of the MCS, is as follows:

$$\begin{aligned} \mathbf{T}_{r_{ac}\to c}\mathbf{R}_{y,\Psi}\mathbf{T}_{c\to r_{ac}} &= \begin{bmatrix} 1 & 0 & 0 & -\epsilon_g r_{ac} \\ 0 & 1 & 0 & 0 \\ 0 & 0 & 1 & 0 \\ 0 & 0 & 0 & 1 \end{bmatrix} \begin{bmatrix} \cos\Psi & 0 & \sin\Psi & 0 \\ 0 & 1 & 0 & 0 \\ -\sin\Psi & 0 & \cos\Psi & 0 \\ 0 & 0 & 0 & 1 \end{bmatrix} \begin{bmatrix} 1 & 0 & 0 & \epsilon_g r_{ac} \\ 0 & 1 & 0 & 0 \\ 0 & 0 & 1 & 0 \\ 0 & 0 & 0 & 1 \end{bmatrix} \\ &= \begin{bmatrix} \cos\Psi & 0 & \sin\Psi & \epsilon_g r_{ac}\cos\Psi - \epsilon_g r_{ac} \\ 0 & 1 & 0 & 0 \\ -\sin\Psi & 0 & \cos\Psi & -\epsilon_g r_{ac}\sin\Psi \\ 0 & 0 & 0 & 1 \end{bmatrix} \end{aligned} \tag{3.27}$$

Finally, a matrix describing the rotation of the tool about the z axis is designated as $\mathbf{R}_{z,\theta_c}$. The angle of rotation of the tool is a function of the angular velocity of the

tool, and changes with time ($\theta_c(t) = \omega_c t + \omega_{cf} t$), and is expressed in the following matrix:

$$\mathbf{R}_{z,\theta_c} = \begin{bmatrix} \cos\theta_c(t) & -\sin\theta_c(t) & 0 & 0 \\ \sin\theta_c(t) & \cos\theta_c(t) & 0 & 0 \\ 0 & 0 & 1 & 0 \\ 0 & 0 & 0 & 1 \end{bmatrix} \tag{3.28}$$

Therefore, the final transformation matrix from the TCS to the MCS can be expressed as a combination of the individual transformations defined in Equations 3.25 to 3.28:

$$\mathbf{M}_{\text{TCS}}^{\text{MCS}} = \mathbf{T}_{g\to c}\mathbf{R}_{x,\Sigma}\mathbf{T}_{r_{ac}\to c}\mathbf{R}_{y,\Psi}\mathbf{T}_{c\to r_{ac}}\mathbf{R}_{z,\theta_c} \tag{3.29}$$

For any given representation of a coordinate system change using a homogeneous transformation matrix, the opposing coordinate system change is expressed using the inverse of the matrix:

$$\mathbf{M}_{\text{MCS}}^{\text{WCS}} = \left[\mathbf{M}_{\text{WCS}}^{\text{MCS}}\right]^{-1} \tag{3.30}$$

Therefore, the total resulting transformation from the TCS to the MCS can be derived by combining the inverse of the matrix in Equation (3.29) with the matrix derived in Equation (3.29), resulting in the following expression:

$$\mathbf{M}_{\text{TCS}}^{\text{WCS}} = \mathbf{M}_{\text{MCS}}^{\text{WCS}}\mathbf{M}_{\text{TCS}}^{\text{MCS}} = \mathbf{R}_{z,-\theta_g}\mathbf{T}_{g\to c}\mathbf{R}_{x,\Sigma}\mathbf{T}_{c\to r_{ac}}\mathbf{R}_{y,\Psi}\mathbf{T}_{r_{ac}\to c}\mathbf{R}_{z,\theta_c} \tag{3.31}$$

3.4.3 Relative Cutting Velocity

In power skiving, a majority of the cutting action is performed by the rotation of the cutting tool. In fact, the contribution of the axial feed rate to the cutting speed is often negligible, and the rate effectively controls the chip thickness rather than the cutting velocity. The cross-axis angle results in the cutting edge being fed axially along the tooth gap of the workpiece. Figure 3.10 shows how the teeth of the cutter proceed through the cutting region due to the tool's rotation.

An estimation of the cutting speed is often used when planning power skiving processes. This nominal cutting speed assumes that the cutting edge moves solely in

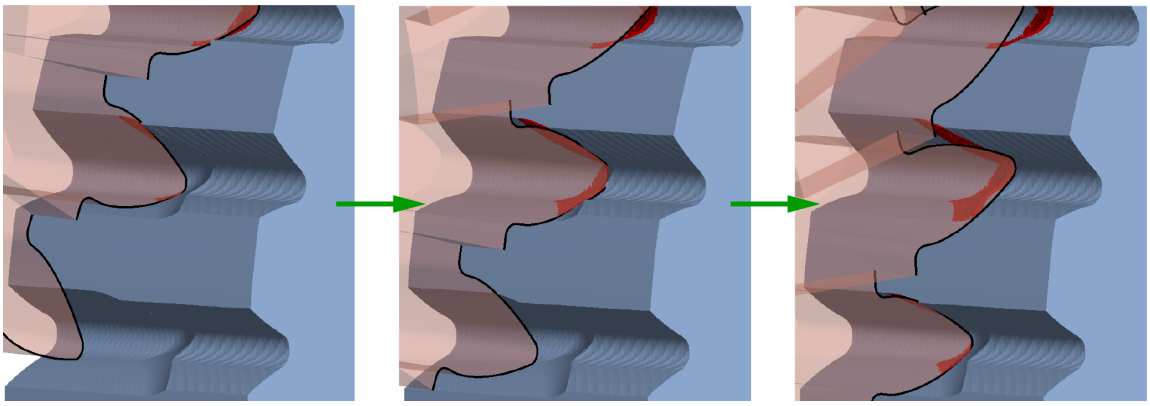

Figure 3.10: Cutting action from the rotation of the power skiving cutter.

the workpiece's z-axis direction, and takes into account the pitch radius and cross-axis angle of the tool. This nominal cutting speed is generally expressed in metres per minute, and is calculated as follows:

$$v_c \approx \omega_c r_{pc} \sin \Sigma \tag{3.32}$$

The actual cutting velocity and magnitude varies both along the cutting edge and with time due to the continuously varying oblique contact conditions resulting from the cutter geometry and rotation. The relative velocity between the cutter and the workpiece directly affects the resultant cutting forces, so a more exact calculation of the velocity is used. In the WCS, the relative motion of the tool resembles rolling motion along a circular path, with the tool rotation axis at the tool centre, and the axis of the path being the centre axis of the workpiece. The velocity resulting from this motion can be seen in Figure 3.11.

A vector expression for the relative velocity ($\mathbf{v}_c$) between the tool and the workpiece for a given point with a position with respect to the tool centre ($p_{i/c}$) and with respect to the workpiece centre ($p_{i/g}$) can be calculated using the rotational velocities of the cutter and workpiece ($\boldsymbol{\omega}_c$ and $\boldsymbol{\omega}_g$, respectively). The velocity equation also includes the axial feed ($\mathbf{v}_f$), though its contribution is often negligible ($< 1\%$ of the total velocity). The expression can be defined in the TCS or the WCS, as follows:

$$\mathbf{v}_c = \boldsymbol{\omega}_c \times \mathbf{p}_{i/c} - \boldsymbol{\omega}_g \times \mathbf{p}_{i/g} + \mathbf{v}_f \tag{3.33}$$

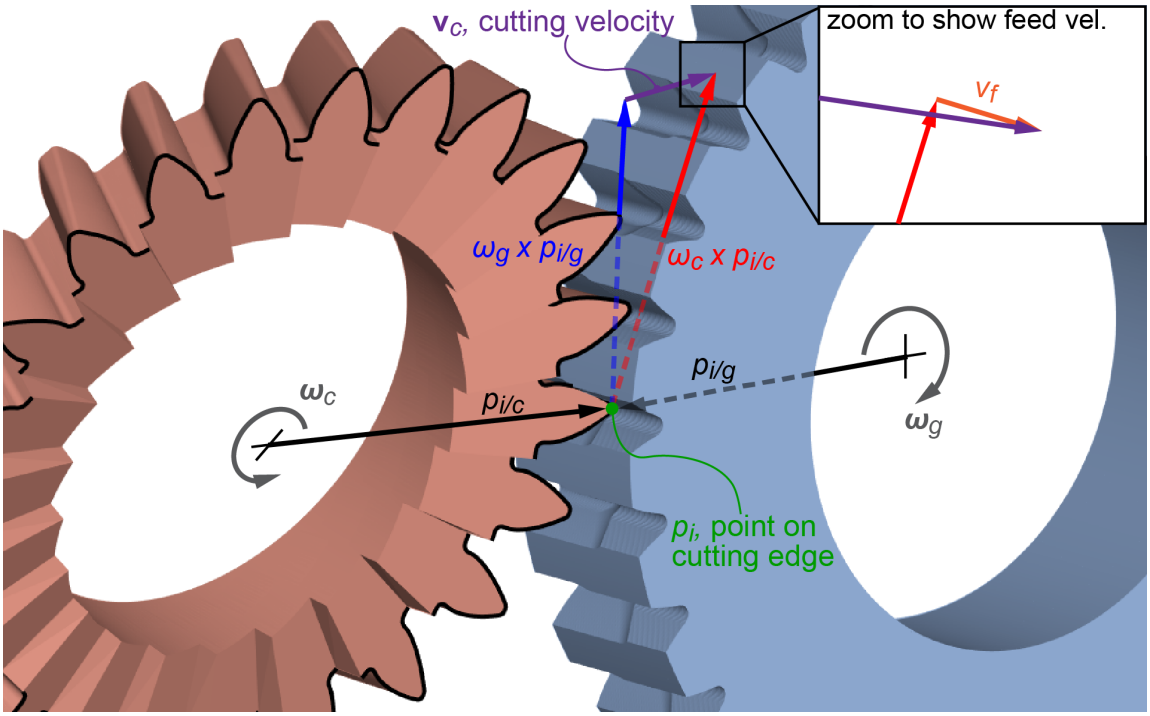

Figure 3.11: Calculation of relative velocity of a point on the cutter tool.

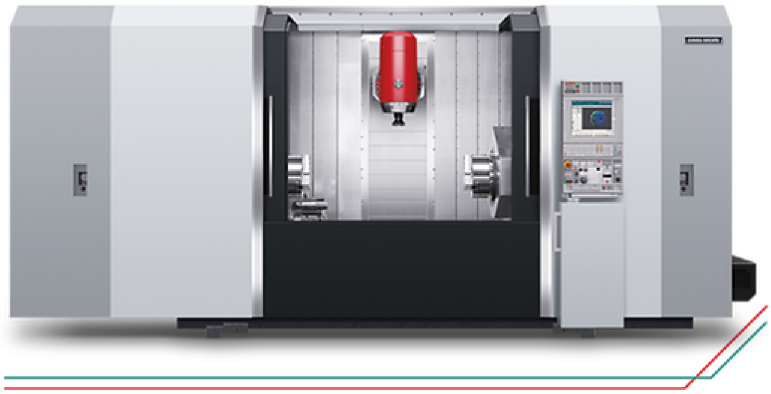

Figure 3.12: DMG MORI NT5400 DCG mill-turn machine (from [112]).

3.5 Validation of Kinematic Model

In order to ensure that the model accurately reflects actual power skiving processes, the kinematics must be validated. Computer numerical control (CNC) signal data was collected during experimental power skiving trials performed on a DMG NT5400 DCG mill-turn machine (see Figure 3.12). The the parameters used in these trials can be found in Appendix A.

Figure 3.13 compares the virtual and measured MCS axis positions of the skiving tool for Trial 25, a 16-pass process. In the model, the tool's retraction along the x axis (for collision avoidance) and its axial return in the z direction are not modelled, thus time delays needed to be added to the simulated position signal between passes in order to align with the measured CNC data. Furthermore, the orientation of the machine axes differed from that of the simulation. The CNC signal directions were oriented accordingly to correspond with the axes established in the virtual model; specifically, the z axis was reversed and the x and y axes were swapped.

The simulated and measured axis positions show excellent agreement. Due to the high mechanical stiffness of the machine, there was minimal signal variation in the CNC data due to displacement caused by the cutting forces. As a result, the difference between simulated and CNC tool positions was below 0.03mm.

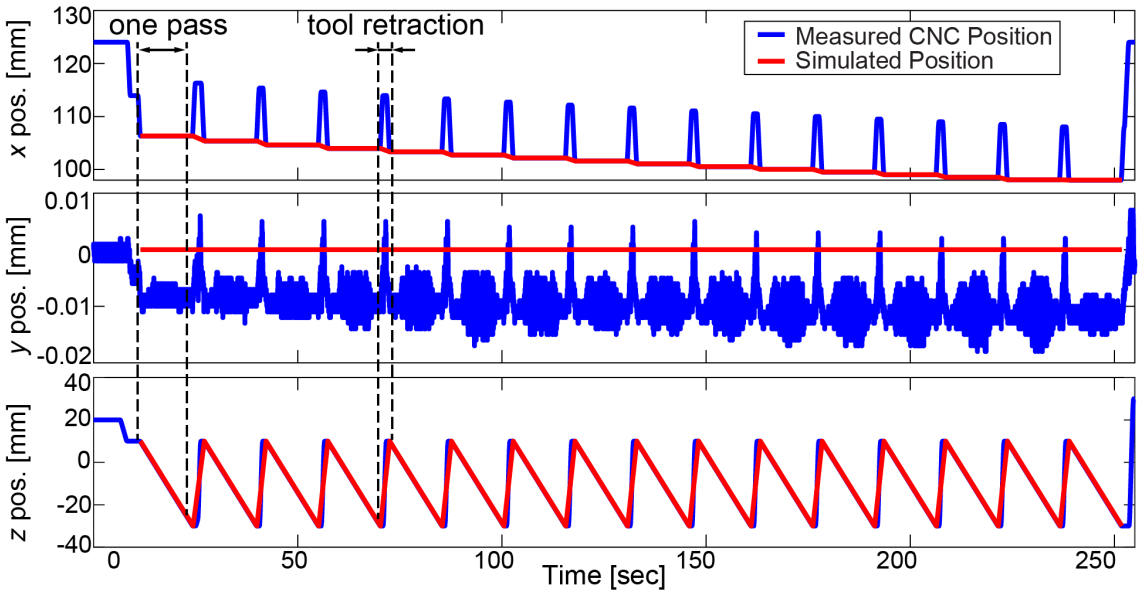

Figure 3.13: Simulated and measured axis commands (Trial 25).

3.6 Conclusions

In this chapter, the geometry and kinematics of the power skiving process were defined. The geometry of the cutting tool and the workpiece were established, the major motions of the cutting process were defined, and the transformations between the three main coordinate systems were determined. A simple equation for describing the relative cutting velocity between the tool and workpiece was also derived. The kinematic model was further verified using the collected CNC signals from a power skiving process performed on a mill-turn machine tool, and was shown to be accurate.

Chapter 4

Cutting Force Prediction

4.1 Introduction

Cutting force predictions for the power skiving process are generated in the form of a time-domain simulation using the kinematics defined in the previous chapter. To calculate these force predictions, tool movements at discrete time steps are used to find uncut chip geometry and, subsequently, the local cutting conditions across the cutting edge of the defined tool. A cutting force model with specified coefficients is then used to create local cutting force predictions which are then summed to create a total force prediction.

This chapter presents the prediction of cutting forces in power skiving using the virtual model. Section 4.2 describes the general cutting force models, including corresponding cutting force coefficient models. The dexel-based cutter-workpiece engagement (CWE) engine used for the model, ModuleWorks, is introduced in Section 4.3. Section 4.4 shows the method used to model a three-dimensional skiving tool for implementation in the CWE engine. In Section 4.5, the dexel data generated by the CWE extraction is used to determine a two-dimensional cross-section of the uncut chip geometry for use in the cutting force model. The methodology for the calculation of local cutting forces is presented in Section 4.6. Finally, trials for

experimental validation are presented in Section 4.7, and the accuracy of the cutting force predictions from the model is examined.

This chapter presents a method of approximating the outer geometry of a shape from the dexel geometry via the generation of contours. This work was originally developed by Mr. Andrew Katz of the University of Waterloo, and implemented for the determination of uncut chip geometry in power skiving by the author.

4.2 Cutting Force Model

4.2.1 Orthogonal Cutting Model

The orthogonal cutting model [113] is a basic but fundamental cutting force model from which others are derived. Figure 4.1 shows the setup of orthogonal cutting consisting of a tool whose cutting edge is oriented perpendicularly to the cutting velocity v_c positioned at a depth of cut (h) into a workpiece of width (b) – otherwise known as the uncut chip thickness and width, respectively. The total cutting force is represented in two orthogonal components; the tangential force (F_t), which is oriented opposite of the cutting velocity, and the feed force (F_f), which is oriented normal to the cutting velocity and tool edge. The forces are represented as linear equations:

$$\left.\begin{aligned} F_t &= F_{tc} + F_{te} = K_{tc}bh + K_{te}b \\ F_f &= F_{fc} + F_{fe} = K_{fc}bh + K_{fe}b \end{aligned}\right\} \tag{4.1}$$

F_{tc} and F_{fc} are forces resulting from the shearing of the chip material from the workpiece, while $F_{te}$and F_{fe} represent additional forces such as the tool rubbing against the workpiece, the build up of material on the cutting edge, and other additional effects. These forces are generally calculated as functions of the uncut chip geometry (the width b and thickness h) and experimentally-determined cutting coefficients (K_{tc}, K_{fc}, K_{te}, and K_{fe}). These coefficients are specific to the cutting setup, and are influenced by factors such as the workpiece material, cutting edge preparation, lubrication, tool surface or coating, cutting speed, and others. The cutting

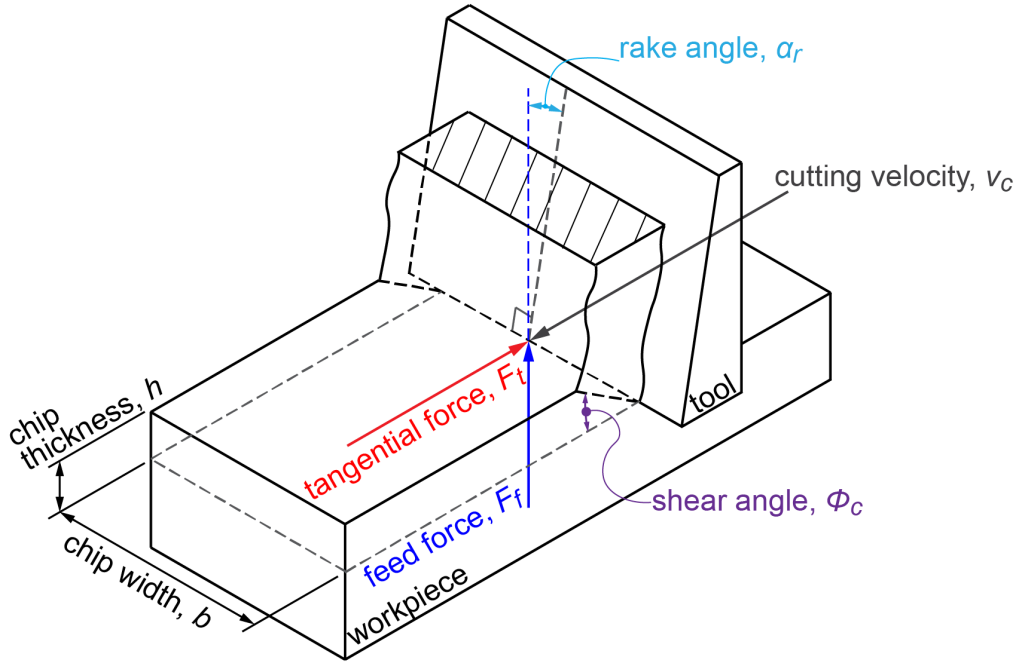

Figure 4.1: Orthogonal cutting model.

forces are also influenced by the rake angle of the tool (α_r) and the angle of shearing action of the chip (ϕ_c).

4.2.2 Oblique Cutting Model

For process modelling, the orthogonal cutting model is generally extended to include a non-orthogonal, or inclined, cutting edge. The result is the oblique cutting model [113], wherein the tool edge is held at an inclination angle (i) with respect to the cutting velocity. A result of the oblique cutting edge is that the chip flows at an angle (η) along the rake face of the tool. As shown in Figure 4.2, the introduction of the inclination angle results in an additional radial force (F_r), which is calculated in a similar manner to the tangential and feed forces:

$$F_r = F_{rc} + F_{re} = K_{rc}bh + K_{re}b \tag{4.2}$$

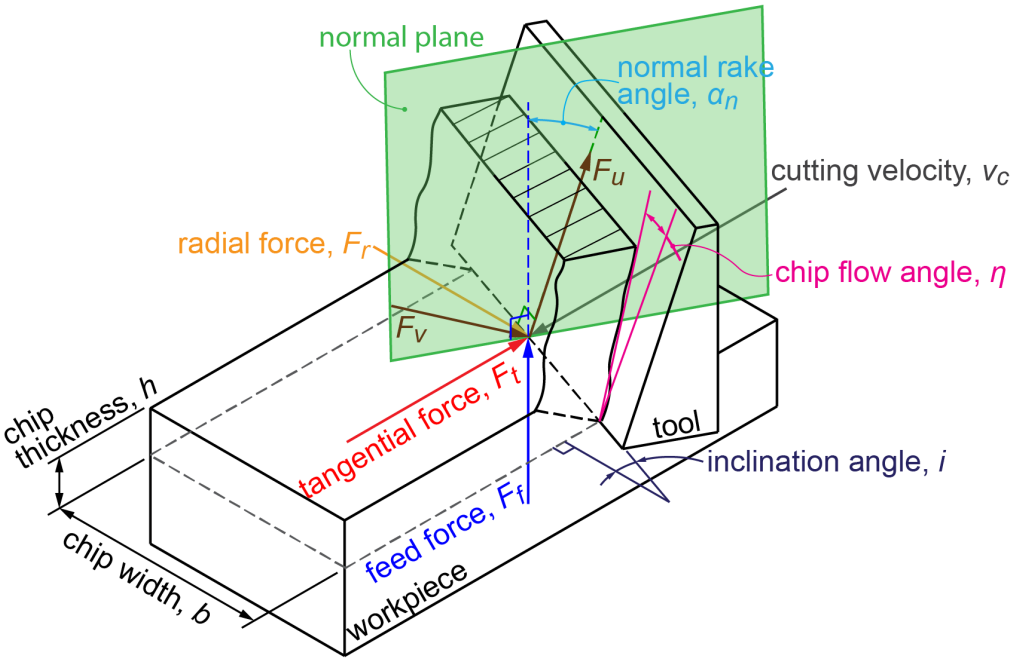

Figure 4.2: Oblique cutting model.

Where the cutting coefficients (K_{rc} and K_{re}), as for the orthogonal coefficients, can be determined experimentally with cutting trials. There are a number of methods for finding the coefficients from cutting trial data, but the two considered in this publication are the orthogonal-to-oblique method and the Kienzle method.

4.2.3 Orthogonal-to-Oblique Cutting Force Coefficients

In the orthogonal-to-oblique method of determining cutting coefficients, a geometric relationship between the oblique and orthogonal cutting models is established [113]. This allows results from orthogonal cutting trials to be used to determine oblique cutting coefficients. This is done by assuming that a plane normal to the cutting edge (see Figure 4.2) is analogous to the orthogonal cutting case. The key cutting properties that are determined from the orthogonal trials are the shear angle (ϕ_c), average friction angle (β_a), and shear stress (τ_s).

The shear angle (ϕ_c) of the orthogonal cut is calculated using a ratio between the uncut chip thickness (h) and the measured resultant chip thickness (h_c), as well as the rake angle (α_r):

$$\phi_c = \tan^{-1} \frac{r_c \cos \alpha_r}{1 - r_c \sin \alpha_r}, \text{ where } r_c = \frac{h}{h_c} \tag{4.3}$$

The average friction angle (β_a) is an estimation of the effect of friction across the tool's rake face. The angle is a function of the cutting forces with the edge effects removed (ie., F_{tc} and F_{fc}), which can be estimated by performing multiple cutting trials [10]. The friction angle is determined as follows:

$$\beta_a = \alpha_r + \tan^{-1} \frac{F_{fc}}{F_{tc}} \tag{4.4}$$

The shearing stress (τ_s) can be calculated as a typical stress relationship of shear force (F_s) over the chip cross section area (A) and related to the cutting forces as demonstrated by Merchant [9], as seen below:

$$\tau_s = \frac{F_s}{A} = bh \frac{F_{tc} \cos \phi_c - F_{fc} \sin \phi_c}{\sin \phi_c} \tag{4.5}$$

From [113], the use of a classical oblique cutting model [114] and geometric relationships results in the following cutting coefficient equations in the normal plane of the oblique cutting model:

$$\left.\begin{aligned} K_{tc} &= \frac{\tau_s}{\sin \phi_n} \frac{\cos(\beta_n - \alpha_n) + \tan i \tan \eta \sin \beta_n}{\sqrt{\cos^2(\phi_n + \beta_n - \alpha_n) + \tan^2 \eta \sin^2 \beta_n}} \\ K_{fc} &= \frac{\tau_s}{\sin \phi_n \cos i} \frac{\sin(\beta_n - \alpha_n)}{\sqrt{\cos^2(\phi_n + \beta_n - \alpha_n) + \tan^2 \eta \sin^2 \beta_n}} \\ K_{rc} &= \frac{\tau_s}{\sin \phi_n} \frac{\cos(\beta_n - \alpha_n) \tan i - \tan \eta \sin \beta_n}{\sqrt{\cos^2(\phi_n + \beta_n - \alpha_n) + \tan^2 \eta \sin^2 \beta_n}} \end{aligned}\right\} \tag{4.6}$$

To use the parameters derived from the orthogonal cutting tests, it is assumed that the inclination angle (i) and the chip flow angle (η) are equal, as per the chip flow rule proposed by Stabler [115], the normal rake angle is equal to that of the

orthogonal rake angle (ie., $\alpha_n = \alpha_r$), and that the normal shear angle is equal to the orthogonal shear angle (ie., $\phi_n = \phi_c$). For the average friction angle, a simple transformation is used, as follows:

$$\beta_n = \tan^{-1}\left(\tan\beta_a \cos\eta\right) \tag{4.7}$$

The edge coefficients (K_{te}, K_{fe}, and K_{re}) are assumed to be equal to those measured from the orthogonal cutting trials for finding the coefficients in Equation (4.6). Since there is no radial component to orthogonal cutting, K_{re} is generally assumed to be zero.

4.2.4 Kienzle Cutting Force Coefficients

The Kienzle model for cutting force coefficients [116] uses a nonlinear, or exponential, term in order to vary the cutting force coefficients with the uncut chip thickness (h). The model is based on the friction and normal forces acting on the rake face of the tool (F_u and F_v, respectively). The friction force acts along the chip velocity vector, which is aligned with the chip flow angle (η), and the normal force acts normal to the rake face of the tool. The forces are calculated as follows:

$$\left.\begin{aligned} F_u &= K_u b h^{1-u} = \left(K_u h^{-u}\right) A \\ F_v &= K_v b h^{1-v} = \left(K_v h^{-v}\right) A \end{aligned}\right\} \tag{4.8}$$

Experimental trials are used to determine the values for the cutting coefficients (K_u, u, K_v, and v). As with the orthogonal-to-oblique method, geometric transformations can relate the Kienzle cutting coefficients with oblique cutting force coefficients, as shown [21]:

$$\left.\begin{aligned} K_{tc} &= K_u h^{-u}\left(\sin i \sin\eta + \cos i \sin\alpha_n \cos\eta\right) + K_v h^{-v} \cos i \cos\alpha_n \\ K_{fc} &= K_u h^{-u}\left(\cos\alpha_n \cos\eta\right) - K_v h^{-v} \sin\alpha_n \\ K_{rc} &= K_u h^{-u}\left(-\cos i \sin\eta + \sin i \sin\alpha_n \cos\eta\right) + K_v h^{-v} \sin i \cos\alpha_n \end{aligned}\right\} \tag{4.9}$$

For the Kienzle model of cutting coefficients, the edge effects are generally assumed to be captured by the cutting coefficients. The edge coefficients (K_{te}, K_{fe}, and K_{re}) are therefore assumed to be zero.

4.3 Cutter-Workpiece Engagement

As seen in the previous section, the calculation of cutting forces using any of the outlined force models requires the determination of the thickness and widths of the undeformed (or uncut) chip geometry. To do so analytically for power skiving would necessitate the determination of the intersection of the involute surfaces of the cutter and workpiece, which changes throughout the duration of the process due to the complex kinematics. Therefore, a solid modelling approach is used to predict the uncut chip geometry for the power skiving model. As mentioned in Chapter 2, there are a number of approaches to solid modelling finding uncut chip geometry in a process model. Exact geometric approaches, including constructive solid geometry and boundary representation, offer precise definitions of the workpiece and chip geometry, but are computationally expensive as they represent solids using numerous boolean operations and equations, respectively. Discrete solid modelling engines conversely represent the solid geometry as a series of data that describes a portion of the total shape or volume, examples of which include solid meshing, voxels, and dexels. Discrete solid representation generally results in better calculation speed and numerical stability, though the geometric accuracy is reduced. For the power skiving model, a multi-dexel modelling approach was chosen for the aforementioned performance advantages. The ModuleWorks [117] software engine, a well-optimized multi-dexel solid modeller, is used for calculating material removal and uncut chip thickness.

In the basic dexel representation model proposed by Van Hook [118], space is represented by an array of parallel rays. The points of intersection of these rays with a solid volume are used to create line segments, hereafter referred to as "nails", which collectively describe the shape of the volume. Since sections of the volume running parallel to the dexel direction can cause poor surface representation, the addition of multiple orthogonal dexel directions is used to more accurately describe the volume [119]. Figure 4.3 shows the necessity of multiple orthogonal dexel directions to accurately describe a shape in two dimensions. For the purposes of the three-dimensional power skiving model, three orthogonal dexel directions are required –

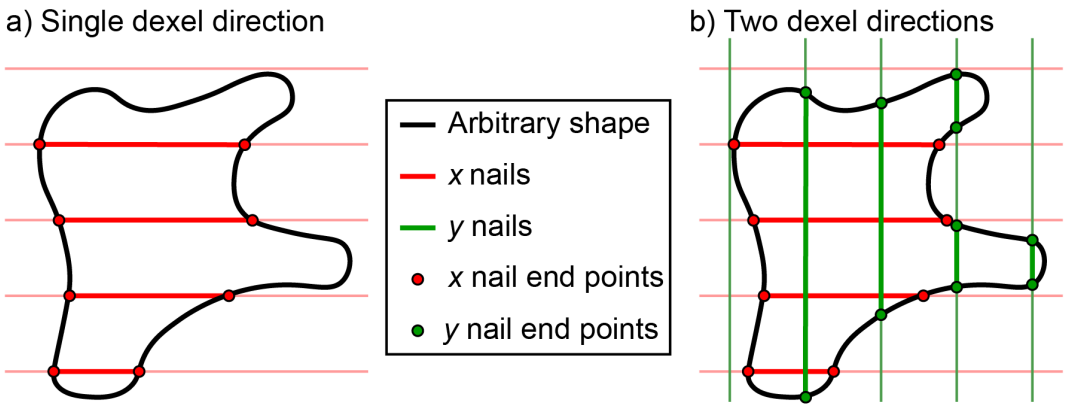

Figure 4.3: Dexel representation of a shape in one and two directions.

known as tri-dexel representation.

The tool, workpiece, and the developed kinematics can be integrated into the ModuleWorks engine, as shown in Figure 4.4. For calculation purposes, the workpiece remains stationary. As a result, all kinematics for the tool must be described in the WCS using the transformation described in Equation (3.20).

From the kinematics, the tool position at each time step in a time-domain simulation is known and can be used to determine the swept volume of the tool as it moves. Normally, this could be found using linear interpolation between the two positions; however, since the movement of the tool in power skiving is mostly rotational, this approach would result in an inaccurate movement. A circular interpolation about the workpiece centre axis is used instead, which keeps the centre of mass of the tool along a circular path about the workpiece in a more accurate representation of the power skiving motion in the WCS. Figure 4.5 shows a simplified comparison of the differing results of the linear and circular interpolation techniques, though the discrepancy between the two methods is much less at the smaller time steps of a power skiving simulation.

The result of the intersection between the tool's swept volume and the workpiece is the 3D uncut chip geometry obtained in dexel format from the ModuleWorks engine, as shown in Figure 4.6. To be compatible with a cutting force model, a 2D

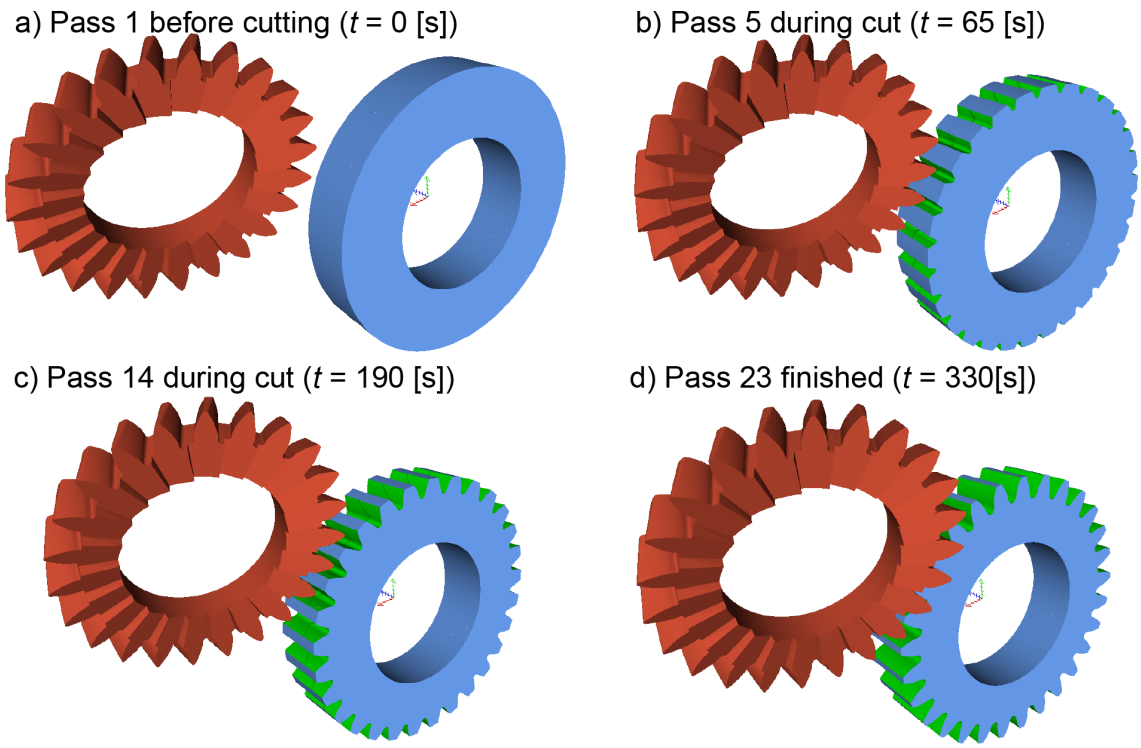

Figure 4.4: Representation of tool and workpiece in the ModuleWorks engine.

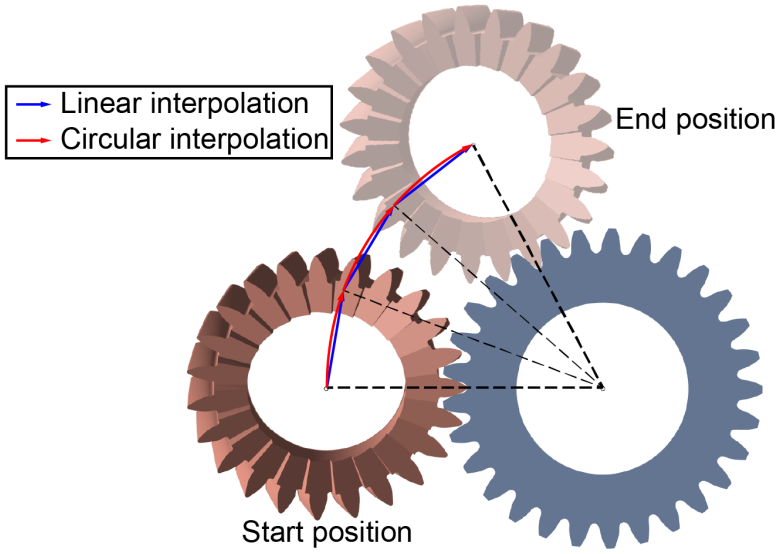

Figure 4.5: Results of linear and spherical linear tool position interpolation.

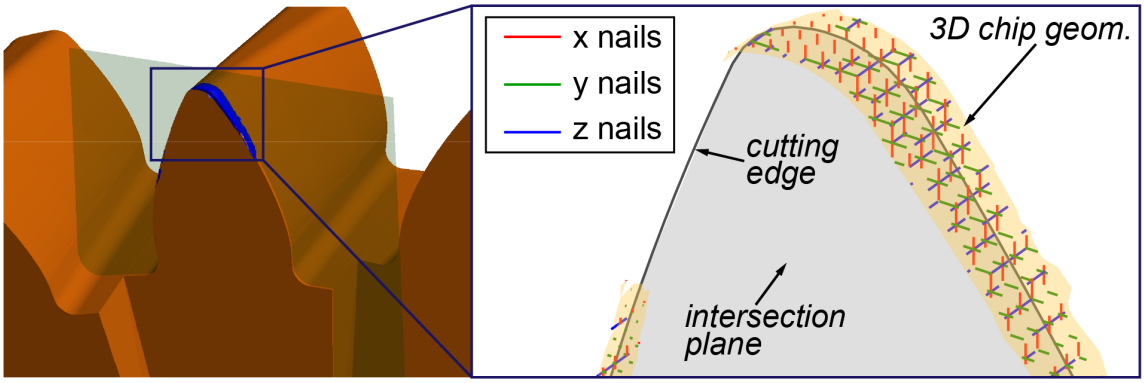

Figure 4.6: Extraction of dexel representation of uncut chip geometry.

cross section of the 3D geometry must be determined.

4.4 Cutting Tool Representation

To accurately calculate the CWE in the ModuleWorks engine, an accurate model of the power skiving tool is created. The tool geometry is based on the standard gear geometry definitions, though adjustments can be made to the nominal geometry in order to accurately reflect any modifications made to the tool by the manufacturer.

4.4.1 Tool Rake Geometry

The rake geometry of the tool depends whether the tool is a spur or helical cutter, as demonstrated in Figure 4.7. For a spur cutter, the rake geometry is a cone, and for a helical cutter, the rake geometry is an array of planes corresponding to each of the individually ground tooth faces.

The conical rake geometry for a spur cutter is described in the TCS by the cone's apex point p_{cone}, its axis $\mathbf{n}_{\text{cone}}$, and the rake angle α_r. This geometry is the same for

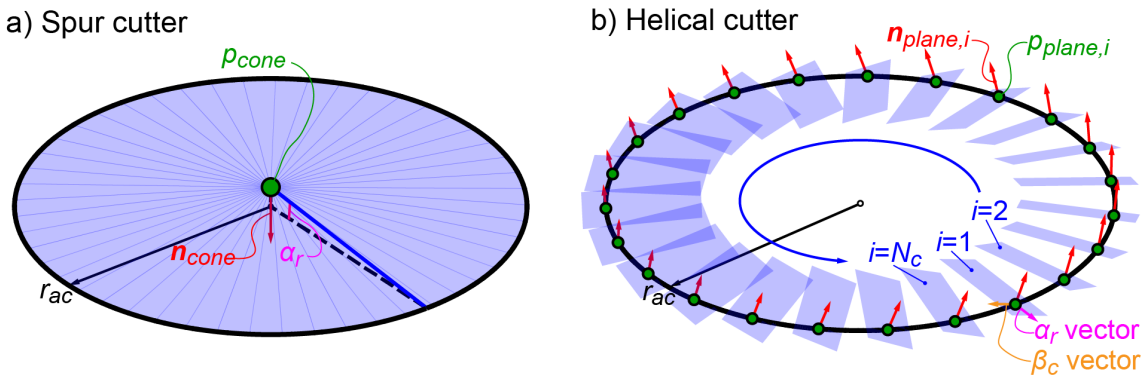

Figure 4.7: Rake geometry of the cutting tool.

all the teeth on the cutter. The apex point is located along the tool's centre axis:

$$p_{\text{cone}} = \begin{bmatrix} 0 \\ 0 \\ r_{ac} \tan \alpha_r \end{bmatrix} \tag{4.10}$$

The axis of the cone is the unit vector connecting the apex and the origin point of the TCS, as shown below:

$$\mathbf{n}_{\text{cone}} = \begin{bmatrix} 0 \\ 0 \\ -1 \end{bmatrix} \tag{4.11}$$

For the planar rake geometry of a single helical cutter tooth, the plane is described by a point p_r and a normal vector $\mathbf{n}_{\text{plane}}$. The point p_{plane} is defined in the TCS at the cutter tip in the centre of the cutting tooth:

$$p_{\text{plane}} = \begin{bmatrix} r_{ac} \\ 0 \\ 0 \end{bmatrix} \tag{4.12}$$

The plane normal is defined as the cross product between vectors representing the tool's helix angle and the rake face inclination at the point on the cutter tip, as

follows:

$$\mathbf{n}_{\text{plane}} = \begin{bmatrix} 0 \\ -\cos\beta_c \\ \sin\beta_c \end{bmatrix} \times \begin{bmatrix} \cos\alpha_r \\ 0 \\ -\sin\alpha_r \end{bmatrix} = \begin{bmatrix} \cos\beta_c \sin\alpha_r \\ \cos\alpha_r \sin\beta_c \\ \cos\alpha_r \cos\beta_c \end{bmatrix} \tag{4.13}$$

Since a plane is defined for each tooth on the cutter, the point and normal for the single tooth case is transformed based on each tooth's angular position:

$$\left.\begin{aligned} p_{\text{plane},i} &= \begin{bmatrix} \cos\frac{(i-1)2\pi}{N_c} & -\sin\frac{(i-1)2\pi}{N_c} & 0 \\ \sin\frac{(i-1)2\pi}{N_c} & \cos\frac{(i-1)2\pi}{N_c} & 0 \\ 0 & 0 & 1 \end{bmatrix} p_{\text{plane}} \\ \mathbf{n}_{\text{plane},i} &= \begin{bmatrix} \cos\frac{(i-1)2\pi}{N_c} & -\sin\frac{(i-1)2\pi}{N_c} & 0 \\ \sin\frac{(i-1)2\pi}{N_c} & \cos\frac{(i-1)2\pi}{N_c} & 0 \\ 0 & 0 & 1 \end{bmatrix} \mathbf{n}_{\text{plane}} \end{aligned}\right\} \text{ where } i = 1, 2, \ldots, N_c \tag{4.14}$$

4.4.2 Discretized Cutting Edge

The most important feature to define on the power skiving tool is the cutting edge, as its geometry drives the cutter-workpiece engagement from which chip geometry is extracted. For the virtual power skiving model, the cutting edge is represented by discrete points referred to as the "nodes" of the cutting tool. As will be shown later in this chapter, the nodes will be used to estimate local cutting conditions and forces. For both the spur and helical cutter cases, the discretized cutting edge is first defined on the transverse plane of the tool. The transverse plane is simply the xy plane in the TCS, with the normal of the plane oriented in the z-axis direction:

$$p_{\text{transverse}} = \begin{bmatrix} 0 \\ 0 \\ 0 \end{bmatrix}, \quad \mathbf{n}_{\text{transverse}} = \begin{bmatrix} 0 \\ 0 \\ 1 \end{bmatrix} \tag{4.15}$$

On the transverse plane, the discretized cutting edge is represented by a series of points (p_{ti}). Each of these points has a radial distance from the centre of the transverse plane (r_{ti}) and an angular position about the z axis of the plane (θ_{ti}), as

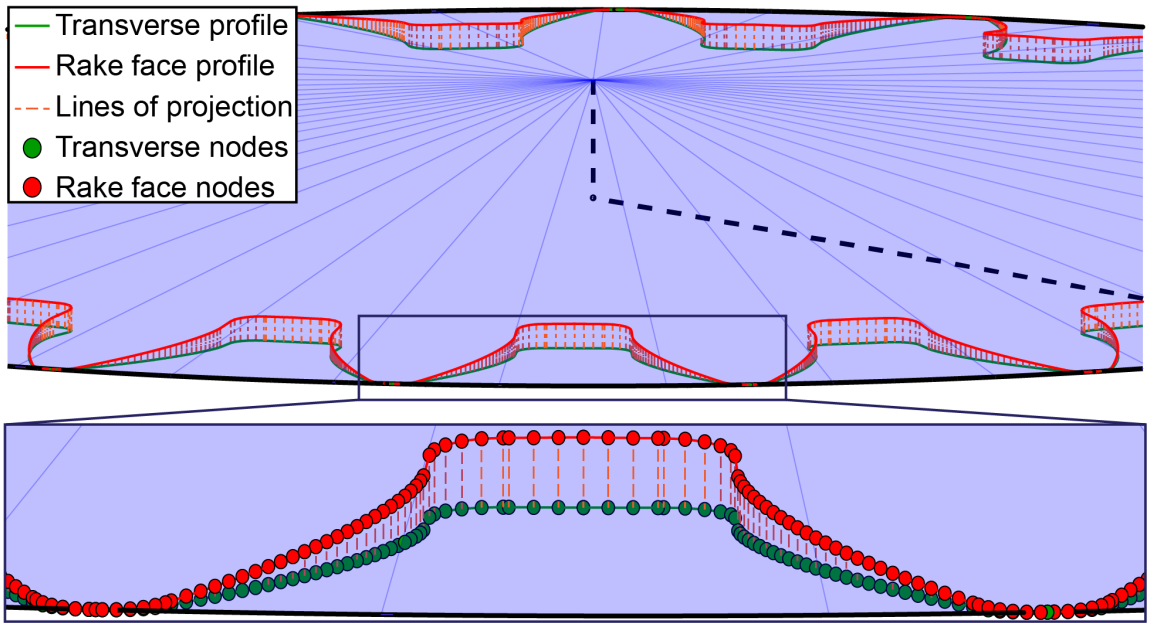

Figure 4.8: Generation of the cutting edge of a spur power skiving tool.

calculated below:

$$r_{ti} = \sqrt{p_{ti,x}^2 + p_{ti,y}^2}, \quad \theta_{ti} = \operatorname{atan2}\left(p_{ti,y}, p_{ti,x}\right) \tag{4.16}$$

The discretized points on the transverse plane of the cutter are used to find corresponding points on the rake face geometry. For the case of a spur cutter, the projection of the transverse points onto the cone is accomplished by using the radial distance of the point to find the z-axis position of the corresponding point on the rake face, as follows:

$$p_{ri} = \begin{bmatrix} p_{ti,x} \\ p_{ti,y} \\ (r_{ac} - r_{ti}) \tan \alpha_r \end{bmatrix} \tag{4.17}$$

The projection of the transverse cutting edge points onto a conical rake face can be seen in Figure 4.8. The profile created by this projection is used as the cutting edge of the tool, with nodes at each specified discretized cutting edge position p_{ri}.

The determination of the cutting edge points for a helical tool is more complex than for a spur tool. Rather than a linear projection of the transverse points onto the rake geometry, a helical projection must be used to accurately reflect the path of the tooth profile as it rotates about the tool's z axis. To accomplish this, a local helix angle is defined at the point on the transverse edge:

$$\beta_p = \tan^{-1}\left(\frac{r\tan\beta_c}{r_{pc}}\right) \tag{4.18}$$

The local helix angle is then used to create the equation for a helix originating from a given point on the transverse plane, as follows:

$$p_{\text{helix}}(z) = \begin{bmatrix} r_{ti}\cos\left(\theta_{ti} + \frac{z-p_{ti,z}}{r_{ti}}\tan\beta_p\right) \\ r_{ti}\sin\left(\theta_{ti} + \frac{z-p_{ti,z}}{r_{ti}}\tan\beta_p\right) \\ z \end{bmatrix} \tag{4.19}$$

The intersection between the defined helix and the rake plane for a given tooth must then be found. The corresponding point on the rake face (p_{ri}) can be found by solving for the following helix-plane intersection equation:

$$\mathbf{n}_{\text{plane},x}\left(p_{\text{helix},x} - p_{\text{plane},x}\right) + \mathbf{n}_{\text{plane},y}\left(p_{\text{helix},y} - p_{\text{plane},y}\right) + \mathbf{n}_{\text{plane},z}\left(p_{\text{helix},z} - p_{\text{plane},z}\right) = 0 \tag{4.20}$$

There is no closed-form solution to Equation (4.20), therefore the intersection points on the rake face representing the cutting edge (p_{ri}) must be found numerically. For the model, Newton's method [120] is used for numerical iteration to find the intersection points. The number of iterations is limited to five, as that provides sufficient convergence in common cases for cutter geometry. Figure 4.9 shows the helical intersections which define the discretized cutting edge for a helical power skiving tool.

4.4.3 In-Engine Tool Representation

For the complete three-dimensional representation in the ModuleWorks engine, the top and side flanks of the tool must be modelled in addition to the cutting edge.

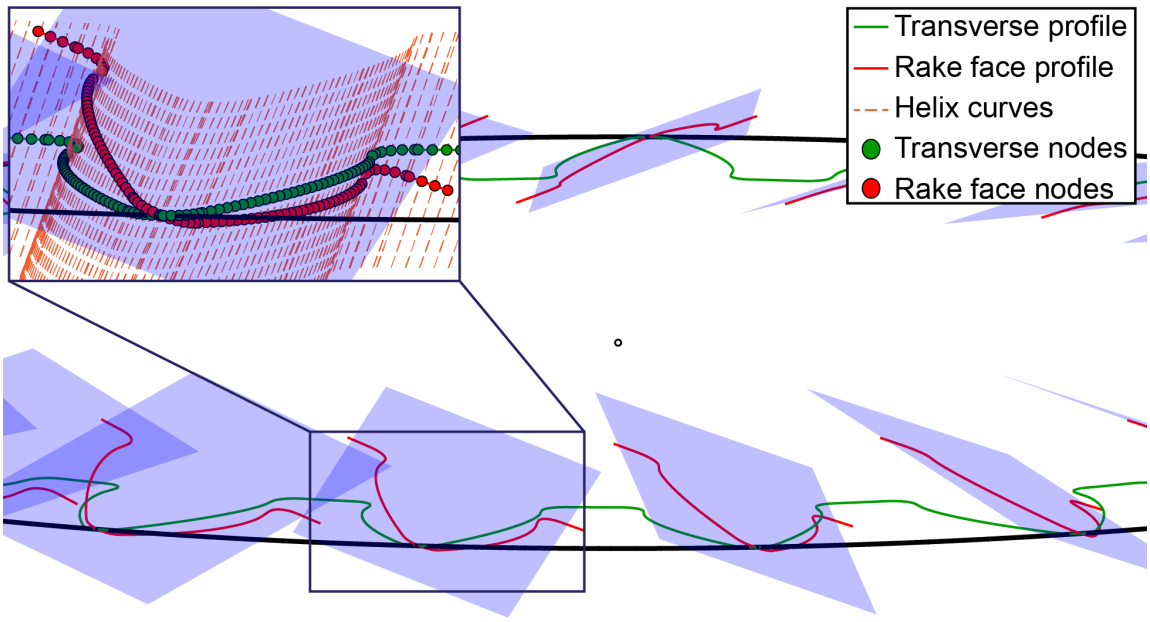

Figure 4.9: Generation of the cutting edge of a helical power skiving tool.

This allows for any collision of the workpiece with the tool flank to be detected, which would indicate kinematic issues with the power skiving process being modelled.

To model the flanks, tooth profiles are generated at a number of heights along the tool's z axis until the desired width of the tool (b_c). To integrate the clearance angles, two adjustments are made to the tooth profile. First, the addendum radius is modified based on the specified outer clearance angle:

$$r_{ac}(z) = r_{ac}(0) - z \tan \alpha_t, \quad z = 0...b_c \tag{4.21}$$

To capture the effect of the side clearance angles, a profile shift is added to subsequent tooth profiles along the gear axis. The calculation of the profile shift for a given height to achieve the specified clearance angle is as follows:

$$x(z) = \begin{cases} x(0) + \frac{z \tan \alpha_s}{2 m_n z \tan \gamma_t}, & \gamma_t > 0 \\ 0, & \gamma_t \leq 0 \end{cases} \tag{4.22}$$

With the known addendum radius and profile shift, discrete points of the tooth

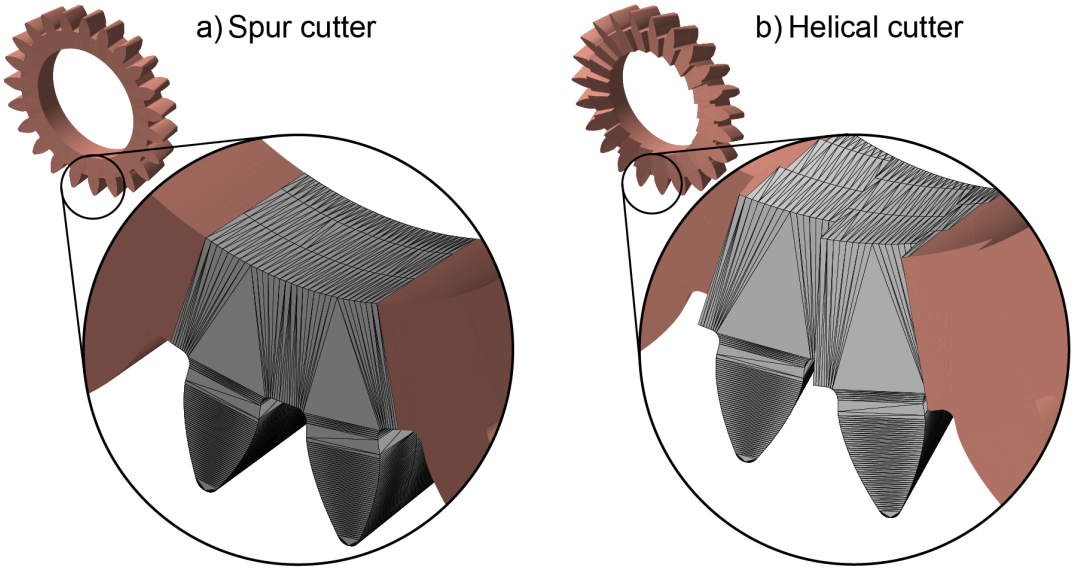

Figure 4.10: Triangular representation of cutting tool.

profiles at the specified heights are generated using the methods specified in Section 4.4.2. Once the points at each z-axis position have been established, triangular connections are created to join all the defined points. The final triangulation of the cutter geometry is then able to be used in the ModuleWorks engine as part of a power skiving simulation. Figure 4.10 shows the triangular representation used to define the power skiving cutter in the engine.

4.5 Uncut Chip Geometry

4.5.1 Dexel Nail Intersection

To determine the cross-section of the uncut chip geometry, a point cloud is first populated from the cutter-workpiece engagement data. The point cloud is generated on the rake face of the tool at an interpolated pose halfway between the start and end poses of the given time step. The first set of points added to the point cloud is at the intersection of the dexel nails and the rake face geometry, as shown in Figure 4.11.

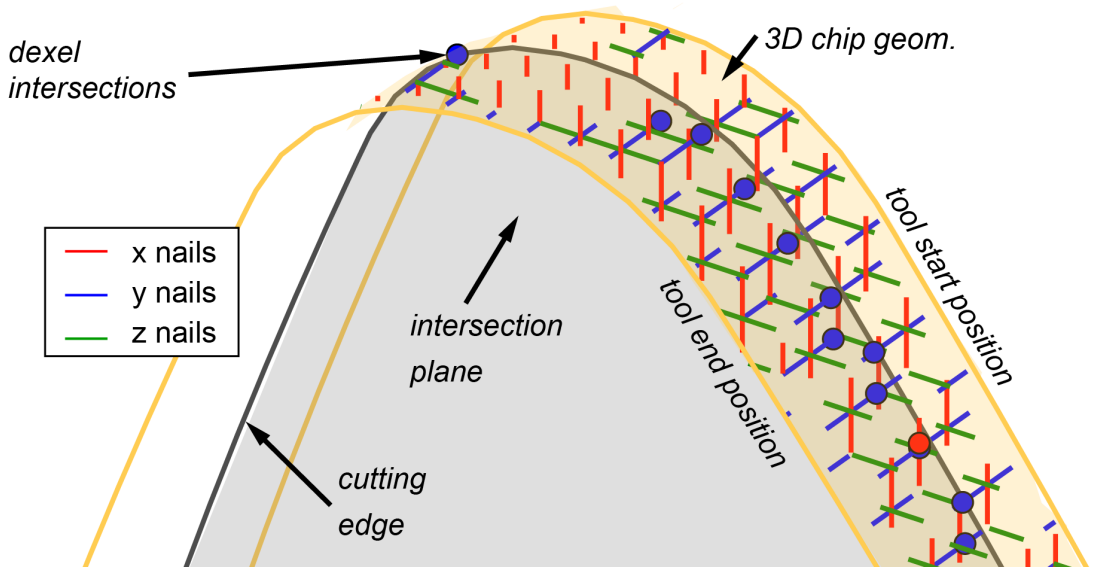

Figure 4.11: Dexel nail intersection with tool rake geometry.

In the case of a spur cutting tool, the intersection point of the nails and the conical rake face must be determined. Each nail has two end points (p_0 and p_1), and the cone for the rake face is defined using an apex point (p_{cone}), a centre axis ($\mathbf{n}_{\text{cone}}$), and a rake angle (α_r). A geometric constant (m) is established as a ratio between the squares of the cone's base radius and height:

$$m = \frac{r_{ac}^2}{(r_{ac} \tan \alpha_r)^2} = \frac{1}{(\tan \alpha_r)^2} \tag{4.23}$$

Vectors are also established between the first end point (p_0) and the cone apex (p_{cone}) as well as between the two nail end points, as follows:

$$\mathbf{w} = p_0 - p_{\text{cone}} \tag{4.24}$$

$$\mathbf{v} = p_1 - p_0 \tag{4.25}$$

The point of intersection can be expressed using a variable ($0 \leq t \leq 1$) in the following manner:

$$p_{xsec} = p_0 + t\mathbf{v} \tag{4.26}$$

To solve for the variable (t), the intersection of the line and cone can be determined as a quadratic equation [121]:

$$at^2 + bt + c = 0, \text{ where } \begin{cases} a = \mathbf{v} \cdot \mathbf{v} - (1+m)\left(\mathbf{v} \cdot \mathbf{n}_{\text{cone}}\right)^2 \\ b = 2\left[\mathbf{v} \cdot \mathbf{w} - (1+m)\left(\mathbf{v} \cdot \mathbf{n}_{\text{cone}}\right)\left(\mathbf{w}\mathbf{n}_{\text{cone}}\right)\right] \\ c = \mathbf{w} \cdot \mathbf{w} - (1+m)\left(\mathbf{w} \cdot \mathbf{n}_{\text{cone}}\right)^2 \end{cases} \tag{4.27}$$

Only the case where there are two real solutions to the quadratic case are considered (ie., $b^2 - 4ac > 0$). For either solution, if $0 \leq t \leq 1$ then that solution is substituted into Equation 4.26 to find the intersection point.

For the planar rake faces for a helical cutter, the point of intersection is first determined by first calculating the distance of each of the end points of the nail as projected onto the normal of the rake plane, as follows:

$$d_0 = (p_0 - p_r) \cdot \mathbf{n}_{\text{cone}} \tag{4.28}$$

$$d_1 = (p_1 - p_r) \cdot \mathbf{n}_{\text{cone}} \tag{4.29}$$

If the end points are determined to be on opposite sides of the plane, then the point of intersection can be found using the following equation:

$$p_{xsec} = p_0 + |d_0| \frac{(p_1 - p_0)}{|d_0| + |d_1|}, \text{ where } d_0 \cdot d_1 \leq 0 \tag{4.30}$$

4.5.2 Contours of Dexel End Points

Only considering the intersection of the dexel nails can result in an inadequate estimation of the 2D cross section depending on the orientation of the intersecting geometry and the dexel resolution, as Figure 4.12 demonstrates. To improve the 2D chip representation, the outer surface of the chip is approximated by creating sets of contours using the end points of the dexel nails. The algorithm used is a simplified version of a method presented by Zhang and Leu [122] which reconstructs 3D surface data from a tri-dexel volume representation.

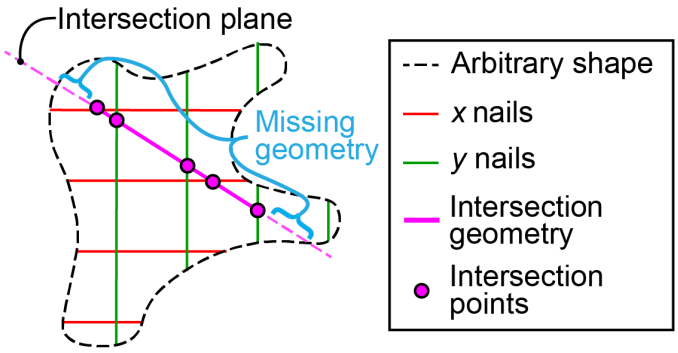

Figure 4.12: Poor estimation of cross-section geometry using only nail intersections.

Figure 4.13 demonstrates how the outer contours are constructed for a set of x- and y-oriented nails. First, a set of coplanar nails is chosen. For example, nails oriented in the x and y directions at the same z height (ie., on an xy plane) are grouped together for analysis. The nails are then sorted in ascending dexel index order. Starting from the smallest dexel index, line segment connections are created between the end points of the current and the neighbouring nail or nails. If an orthogonal nail (for example, a y-oriented nail when analyzing the x nails) intersects the neighbouring nail, a connection is first made to the closest end point of that orthogonal nail, then to the end point of the neighbouring nail. This continues until connections have been made for all subsequent nails, and the connections are labelled based on the nail orientation (ie., xx connections for x-oriented nails). Connections are similarly generated for the orthogonal nails, and then the two sets of connections are combined to form the outer contour for the plane. The set of connections on an xy plane is referred to as an xy contour.

The algorithm is then applied for every xy, xz, and yz plane with dexel nails present, generating a complete set of contours which describe the outer geometry of the 3D chip. The intersection between the outer contours and the intersecting geometry can then be used to improve the cross-section estimation of the chip, as seen in Figure 4.14. Discrepancies between the actual shape and that of the outer contours may still be present, as the accuracy of the outer contours as an estimation of the shape is limited by the dexel resolution used during the simulation.

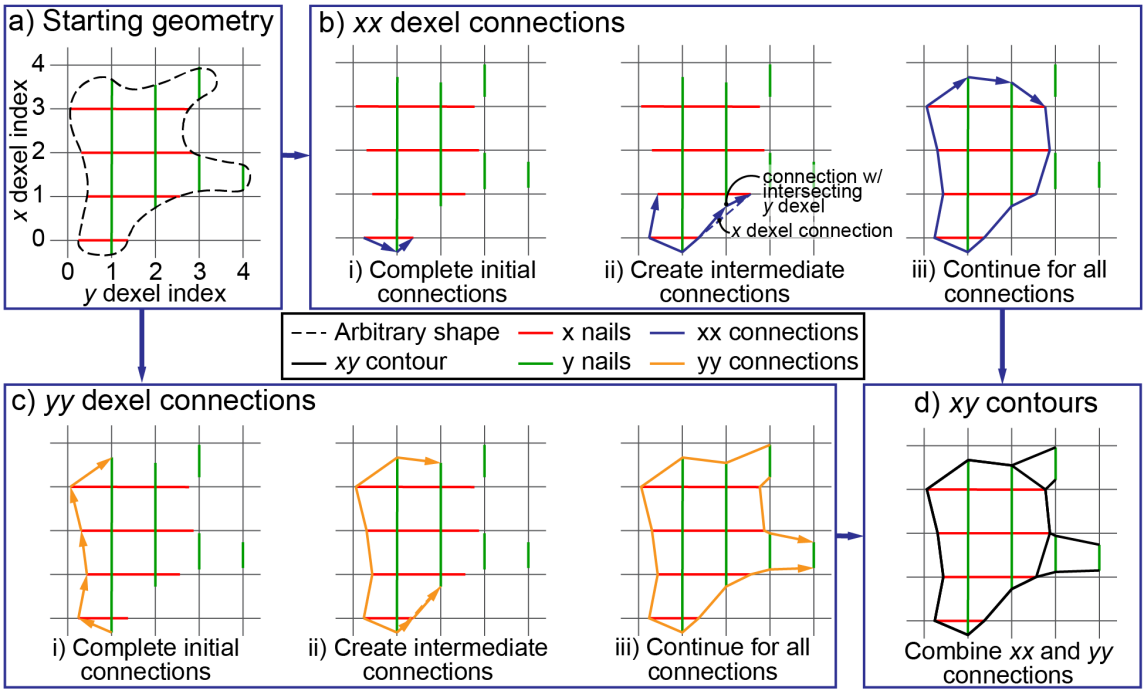

Figure 4.13: Procedure to generate outer contours in xy plane.

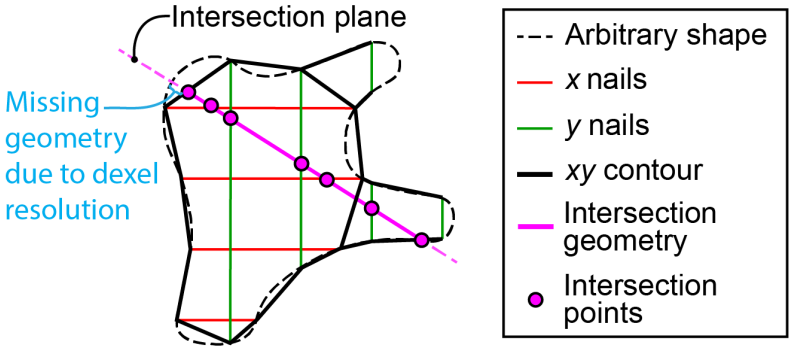

Figure 4.14: Improved cross-section geometry estimation with outer contour.

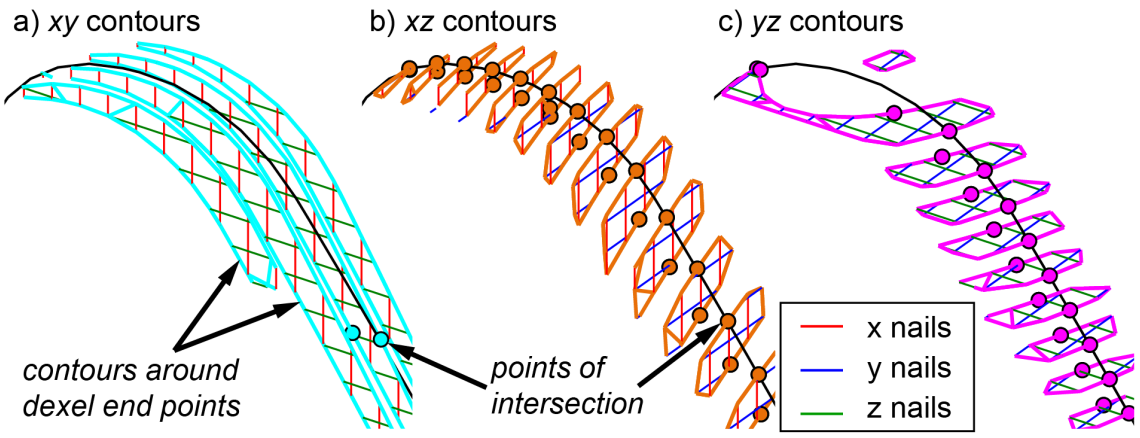

Figure 4.15: Creation and intersection of uncut chip contours from dexel end points.

As shown in Figure 4.15, intersections between the contours' line segments and the tool rake geometry are found for xy, xz, and yz outer contours. The calculation method for finding these intersections is the same as for finding the original nail intersections. These points are added to the set 2D chip geometry points generated from the dexel nail intersection and nodes of the cutting edge.

4.5.3 Engaged Cutting Edge Nodes

As explained in Section 4.4, the cutting edge of the power skiving tool is discretized into nodes. The nodes of the cutting edge form the basis of the cutting force calculations, and are thus included in the representation of the 2D chip cross section. However, only the nodes that are considered "engaged" with the cut are required. Therefore, only nodes within a distance threshold of another point in the point cloud (the threshold being set to the dexel spacing d_{dexel}) are kept. Since the cutter points are in the TCS, they must be transformed into the WCS using the coordinate system transformations outlined in Section 3.4.

4.5.4 Triangulation of Point Cloud

Geometric relationships between the points in the point cloud are established using the α-shape (hereafter called the alpha-shape) method for determining the shape of points in a planar set [123]. The alpha-shape method involves first determination of the Delaunay triangulation (DT) of the point set, which is the joining of all the points in the set though non-overlapping triangles whose circumscribed circles do not contain the points of any other triangle. A circumscribed circle in one that passes through each of the three points defining a triangle, and its location coordinates (x_c, y_c) and radius (r_c) are calculated as:

$$\begin{aligned} x_c &= \frac{\left(x_0^2+y_0^2\right)(y_2-y_1)+\left(x_1^2+y_1^2\right)(y_0-y_2)+\left(x_2^2+y_2^2\right)(y_1-y_0)}{2\left(x_0\left(y_2-y_1\right)+x_1\left(y_0-y_2\right)+x_2\left(y_1-y_0\right)\right)} \\ y_c &= \frac{\left(x_0^2+y_0^2\right)(x_1-x_2)+\left(x_1^2+y_1^2\right)(x_2-x_0)+\left(x_2^2+y_2^2\right)(x_0-x_1)}{2\left(x_0\left(y_2-y_1\right)+x_1\left(y_0-y_2\right)+x_2\left(y_1-y_0\right)\right)} \\ r_c &= \sqrt{\left(x_c-x_0\right)^2+\left(y_c-y_0\right)^2} \end{aligned} \quad \text{[124]} \quad (4.31)$$

To accomplish the Delaunay triangulation, a version of the Bowyer-Watson algorithm [125] is used. First, a triangle sufficiently large to encompass all the points in the set is established. The points are then inserted into the triangulation one at a time. Any triangle whose circumscribed circle contains the new point is removed, and new triangles are established using the vertices of the removed triangles and the new point. Once all points in the set have been inserted, the vertices of the large triangle that originally encompassed all the points are removed along with any triangles associated to them.

The second step of the alpha-shape method is to set a size threshold on the triangles, as the original Delaunay triangulation will be by definition a convex hull that does not necessarily reflect the shape of the chip. In the typical definition of the alpha shape, a threshold is set to limit the maximum size of the circumcircle of the triangles. In this model, a modified version of this method is employed with a different threshold. A threshold for the longest edge of each triangle is used in order to simplify the computation. By removing triangles whose edges are larger than the

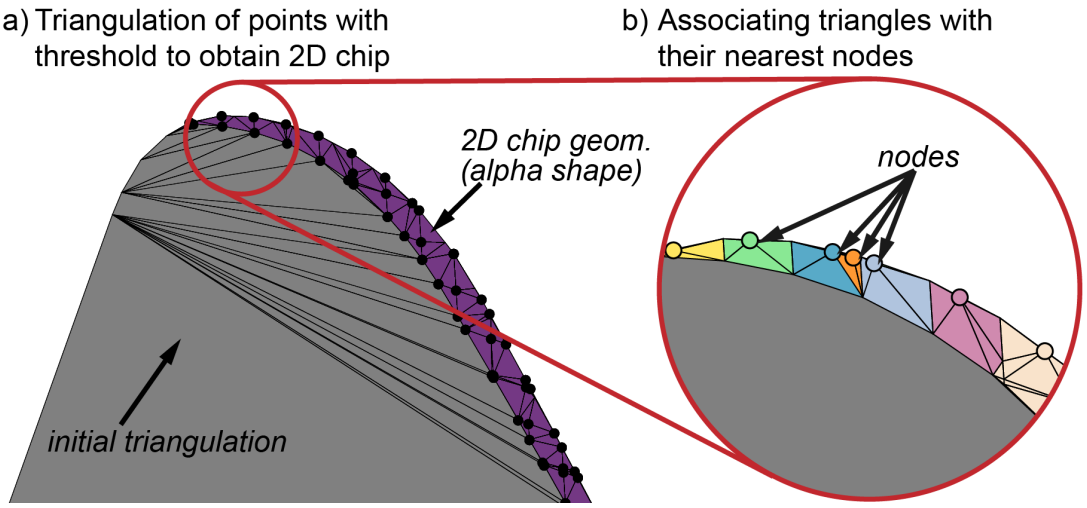

Figure 4.16: Triangulation of chip geometry points and association with nearest nodes.

set threshold (established as $\sqrt{3}d_{\text{dexel}}$), the triangulation represents the uncut chip cross section, as seen in Figure 4.16a.

The overall cutting force prediction for each time step is based on a summation of the cutting forces calculated from each of the engaged nodes of the discretized cutting edge. Thus, each triangle in the final triangulation of the uncut chip cross section is associated with the node that is closest in distance to the triangle's centre point. Figure 4.16b demonstrates that this results in numerous chip sections which can easily integrated with the oblique cutting model for cutting force prediction.

The effective area of the chip associated with each node is calculated by summing the area of each associated triangle. As demonstrated in Equations (4.1) and (4.2), the geometry of the chip being cut is directly used to predict cutting forces. The area for each triangle defined by points p_0, p_1, and p_2 is found using Heron's formula

for the area of a triangle [126]:

$$A = \sqrt{s\left(s - l_{01}\right)\left(s - l_{02}\right)\left(s - l_{12}\right)},$$
$$\text{where} \begin{cases} l_{01} &= \sqrt{\left(x_1 - x_0\right)^2 + \left(y_1 - y_0\right)^2 + \left(z_1 - z_0\right)^2} \\ l_{02} &= \sqrt{\left(x_2 - x_0\right)^2 + \left(y_2 - y_0\right)^2 + \left(z_2 - z_0\right)^2} \\ l_{12} &= \sqrt{\left(x_2 - x_1\right)^2 + \left(y_2 - y_1\right)^2 + \left(z_2 - z_1\right)^2} \\ s &= \frac{l_{01}+l_{02}+l_{12}}{2} \end{cases} \tag{4.32}$$

4.5.5 Uncut Chip Geometry Comparison

To determine a comparative accuracy of the uncut chip geometry extracted from the model, a basic visual comparison was performed between sample chips collected from the power skiving trials (see Section 4.7) and the corresponding uncut chip geometry created in a simulation of the trial. A portable microscope camera and stand were used to examine the collected chips; however, the microscope and stand required are an imprecise assembly, and therefore only approximate values for dimensional measurements could be used after calibrating the image.

Chips were collected from Pass 4 and Pass 9 of Trial 20, the parameters for which can be found in Table A.4. Uncut chip geometry from the same passes in a simulation of Trial 20 were also obtained, and the collected and simulated chips are compared in Figure 4.17. Despite the deformation in the collected chips, the shapes of the simulated and machined chips are quite similar. The measured dimensions are reasonably similar, though the nature of the material deformation during the creation of the chips reduces the significance of any direct comparison.

4.6 Calculation of Cutting Forces

4.6.1 Local Cutting Force Conditions

The cutting force on the power skiving tool are determined at each node on the cutting edge using forces calculated with the oblique cutting model (Equations (4.1)

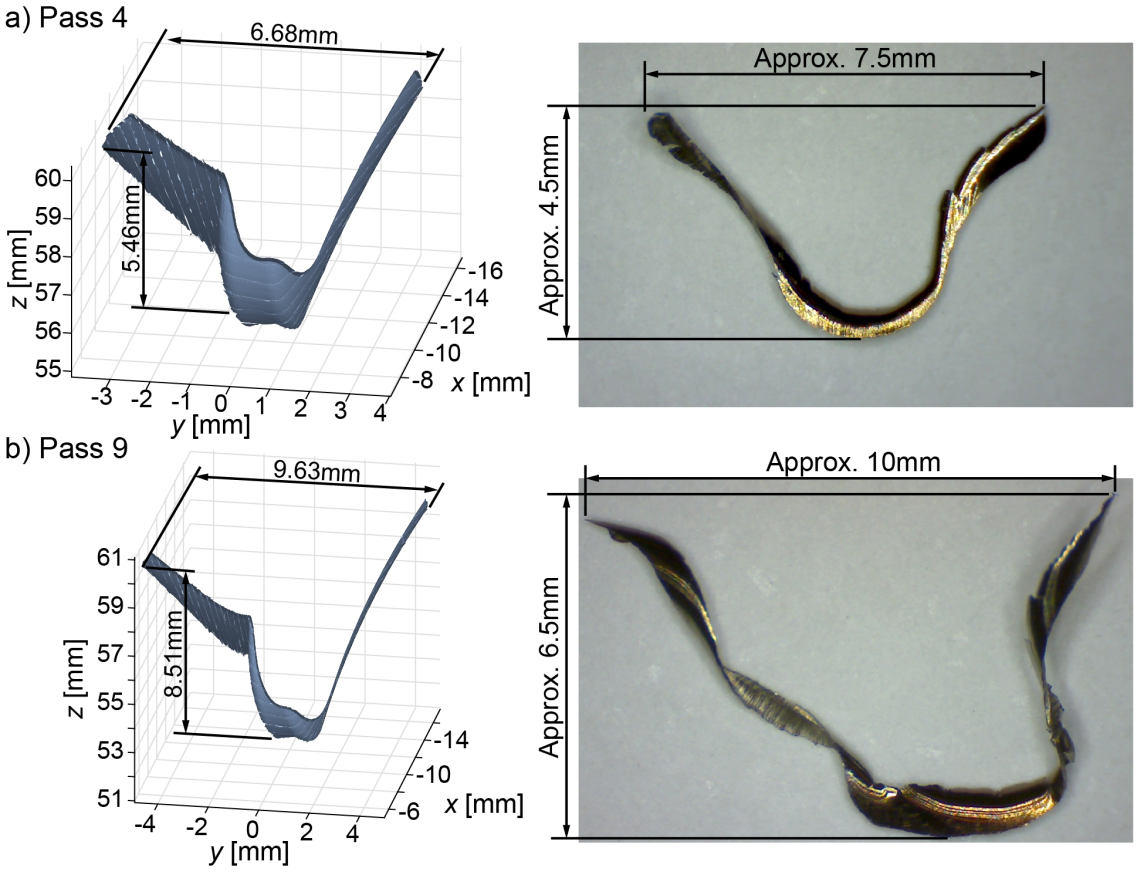

Figure 4.17: Comparison of collected and simulated chip geometry for Trial 20.

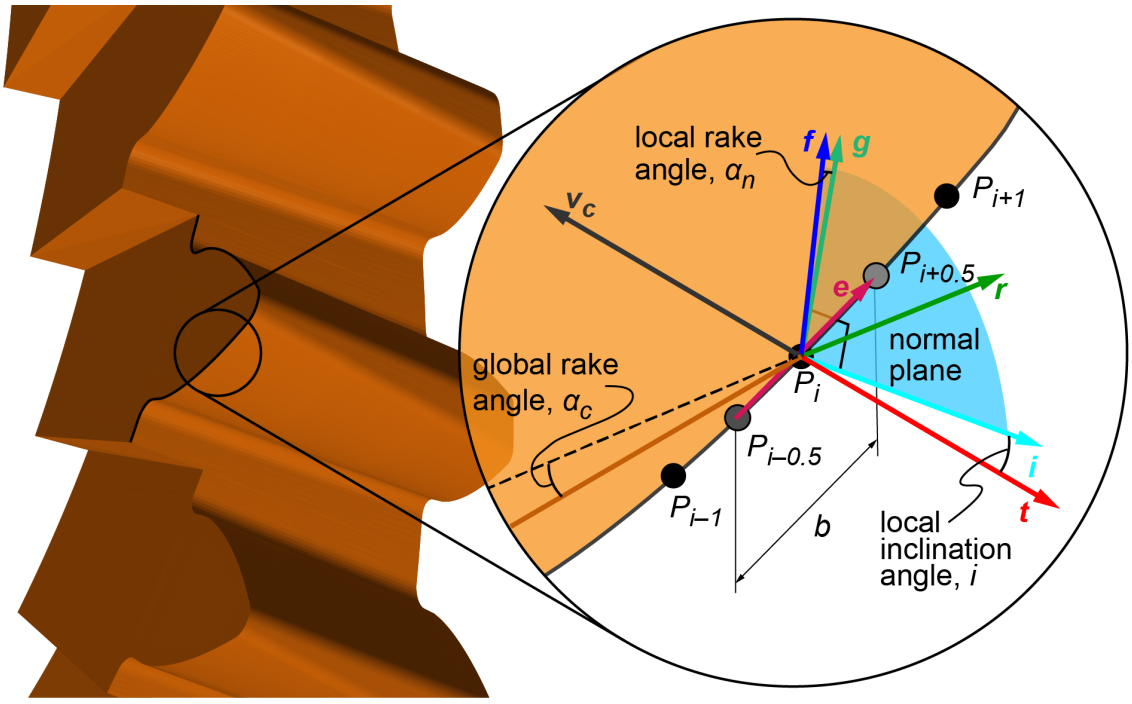

Figure 4.18: Oblique cutting model applied to tool cutting edge.

and (4.2)). In contrast with the CWE calculations, cutting forces are determined in the TCS. The orientations of these forces differ based on the relative velocity and local geometry of the cutting tool. These orientations are represented as vectors for the tangent (t), feed (f), and radial (r) directions. Additionally, the local rake (α_n) and inclination (i) angles can be determined, both of which have an effect on the resulting cutting force conditions and coefficients. Figure 4.18 shows the key vectors for the oblique model as applied to a node on the power skiving cutting edge.

The tangent direction vector ($\mathbf{t}$) is defined in the opposite direction of the relative velocity of the cutting edge ($\mathbf{v}_c$):

$$\hat{\mathbf{t}} = -\hat{\mathbf{v}}_c \tag{4.33}$$

An edge vector ($\mathbf{e}$) is established to represent the local cutting edge of the tool. A given node has a position p_i and its neighbouring nodes are positioned at p_{i-1} and p_{i+1}. The midpoint between p_i and p_{i-1} as well as the midpoint between p_i and p_{i+1}

($p_{i-0.5}$ and $p_{i+0.5}$, respectively) are determined and used to establish the edge vector:

$$\mathbf{e} = p_{i+0.5} - p_{i-0.5} = \frac{p_{i+1} + p_i}{2} - \frac{p_i + p_{i-1}}{2} \tag{4.34}$$

The feed vector direction ($\mathbf{f}$) is then calculated as the cross-multiplication of the edge vector and tangent vector:

$$\hat{\mathbf{f}} = \hat{\mathbf{e}} \times \hat{\mathbf{t}} \tag{4.35}$$

Similarly, the local inclination vector of the tool ($\mathbf{i}$) is the result of the cross-multiplication of the feed and edge vectors:

$$\hat{\mathbf{i}} = \hat{\mathbf{f}} \times \hat{\mathbf{e}} \tag{4.36}$$

The local rake angle (i) for the node, defined between the tangent and inclination vectors, can also be determined:

$$i = \cos^{-1}\left(\hat{\mathbf{i}} \cdot \hat{\mathbf{t}}\right) \tag{4.37}$$

Finally, the radial vector ($\mathbf{r}$) can be established as orthogonal to the tangent and feed vectors. The radial vector and inclination vector must be at an acute angle with one another, therefore the radial vector is reversed if necessary:

$$\hat{\mathbf{r}} = \hat{\mathbf{t}} \times \hat{\mathbf{f}}, \qquad \hat{\mathbf{r}} = \begin{cases} \hat{\mathbf{r}}, & \hat{\mathbf{r}} \cdot \hat{\mathbf{i}} > 0 \\ -\hat{\mathbf{r}}, & \hat{\mathbf{r}} \cdot \hat{\mathbf{i}} < 0 \end{cases} \tag{4.38}$$

The width of the chip (b) is estimated by projecting the length of the edge vector onto the radial vector using the inclination angle:

$$b = \|\mathbf{e}\| \cos i \tag{4.39}$$

The thickness of the chip (h) is then estimated using the chip area determined from the triangulation of the cross section and the width of the chip:

$$h = \frac{A}{b} \tag{4.40}$$

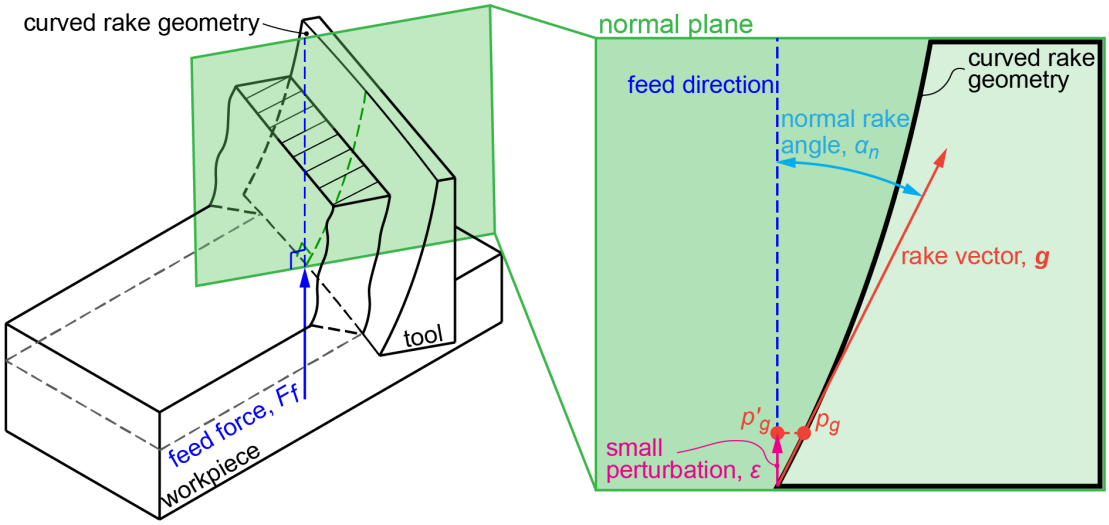

Figure 4.19: Approximation of local rake vector angle on a conical tool face.

Lastly, the local rake angle (α_n) for the node is calculated. Since the angle is a function of the rake face geometry, a vector representing the orientation of the rake surface on the normal plane ($\mathbf{g}$) is established. For a spur cutter with a conical rake face, the rake vector must be established based on an approximation of the rake face geometry for a small distance from the node, as in Figure 4.19.

To estimate the local rake geometry, an approximate point on the rake face (p_g) is created. First, a point (p'_g) along the feed vector a small distance (ε) from the node point (p_i) is established:

$$p'_g = p_i + \varepsilon \hat{\mathbf{f}} \tag{4.41}$$

The z-axis coordinate for the point can then be adjusted to be on the cone surface by using the radial distance of the point from the apex as well as the z-axis coordinate of the cone's apex:

$$p'_{gz} = p_{rz} - \sqrt{{p'_{gx}}^2 + {p'_{gy}}^2} \tan \alpha_r \tag{4.42}$$

The point on the feed vector is then used to obtain the point on the rake face by projecting it onto the normal plane:

$$p_g = p'_g + \left(\left(p'_g - p_i \right) \cdot \hat{\mathbf{e}} \right) \hat{\mathbf{e}} \tag{4.43}$$

The rake vector can then be established between the projected point and the local node point:

$$\hat{\mathbf{g}} = \frac{p_g - p_i}{\|p_g - p_i\|} \tag{4.44}$$

For a helical cutter, the rake face is planar, and the derivation of the rake vector is more straightforward:

$$\hat{\mathbf{g}} = \hat{\mathbf{n}}_r \times \hat{\mathbf{e}} \tag{4.45}$$

The local rake angle can then be calculated based on the angle between the rake vector and the feed vector. Similarly to the radial vector, the rake angle must be flipped if the rake and inclination angles do not form an acute angle:

$$\alpha_n = \cos^{-1}\left(\hat{\mathbf{g}} \cdot \hat{\mathbf{f}}\right), \qquad \alpha_n = \begin{cases} \alpha_n, & \hat{\mathbf{g}} \cdot \hat{\mathbf{i}} \geq 0 \\ -\alpha_n, & \hat{\mathbf{g}} \cdot \hat{\mathbf{i}} < 0 \end{cases} \tag{4.46}$$

Owing to the unique nature of the kinematics and geometry of the power skiving process, both the local rake angles and inclination angles vary both across the cutting edge and as the cut proceeds through the workpiece. As a result, the orientation of the cutting force directions will vary along the cutting edge, as seen in Figure 4.20. Figure 4.21 shows an example of the extent to which the two angles can vary during a single pass of a cutting tooth. The rake angle, in particular, can be seen to vary from a large negative ($\alpha_n < -30°$) to a highly positive ($\alpha_n > 30°$) value. This variance must be considered during force calculations, as cutting coefficients can be significantly affected by the local rake angle.

4.6.2 Force Prediction in the Virtual Model

For integration into the cutting force model, the kinematics of the power skiving process, the extraction of uncut chip geometry, and the calculation of the local cutting conditions are combined into a time-domain simulation. The process is defined in incremental time steps, where the start and end tool positions are defined by the kinematic model. The ModuleWorks engine then calculates the CWE, from which

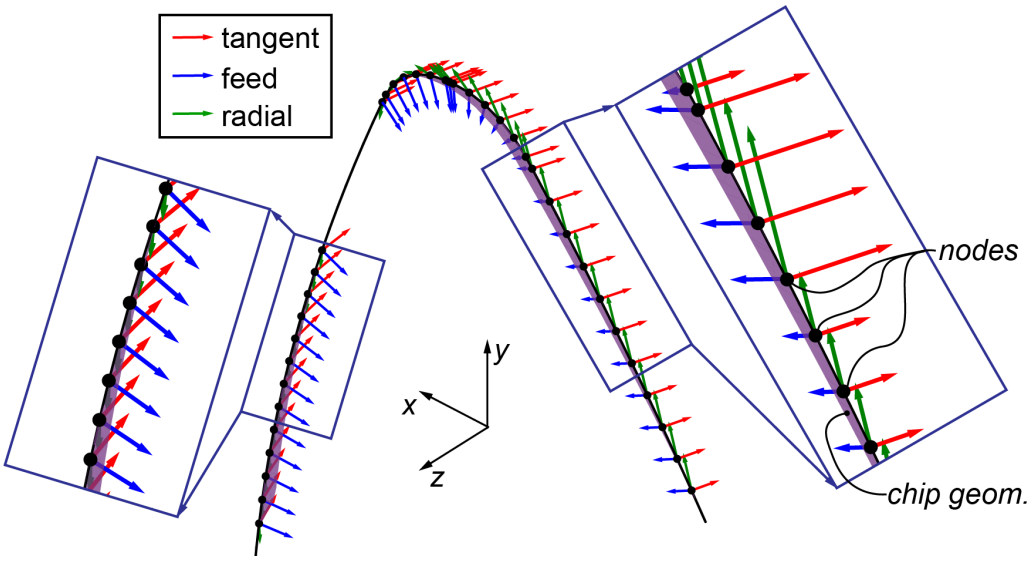

Figure 4.20: Cutting force component directions along cutting edge.

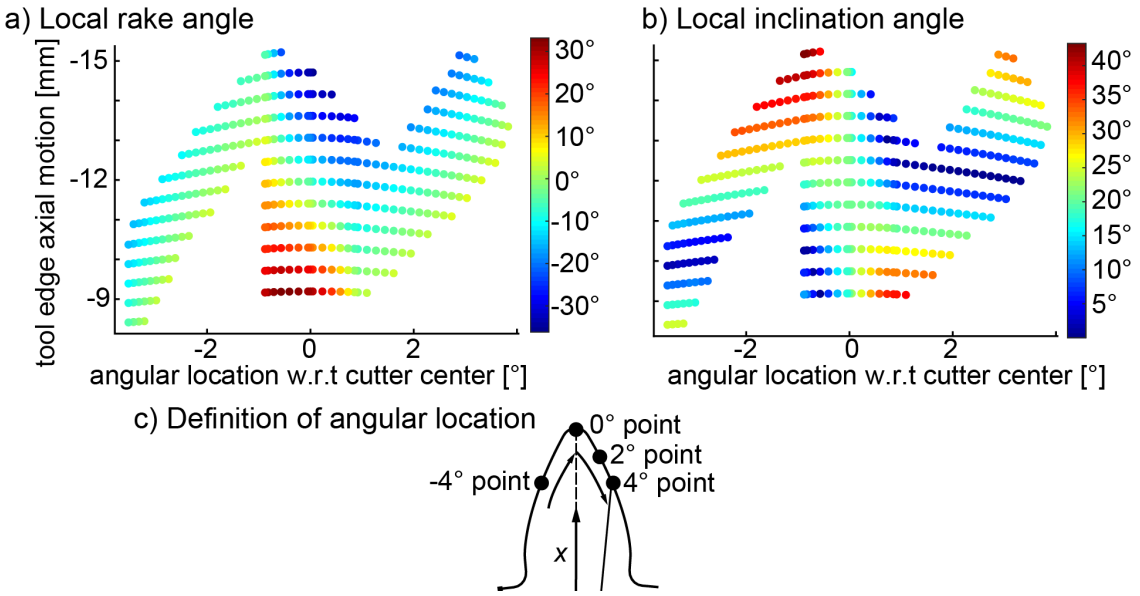

Figure 4.21: Local rake and inclination angles during one tooth pass.

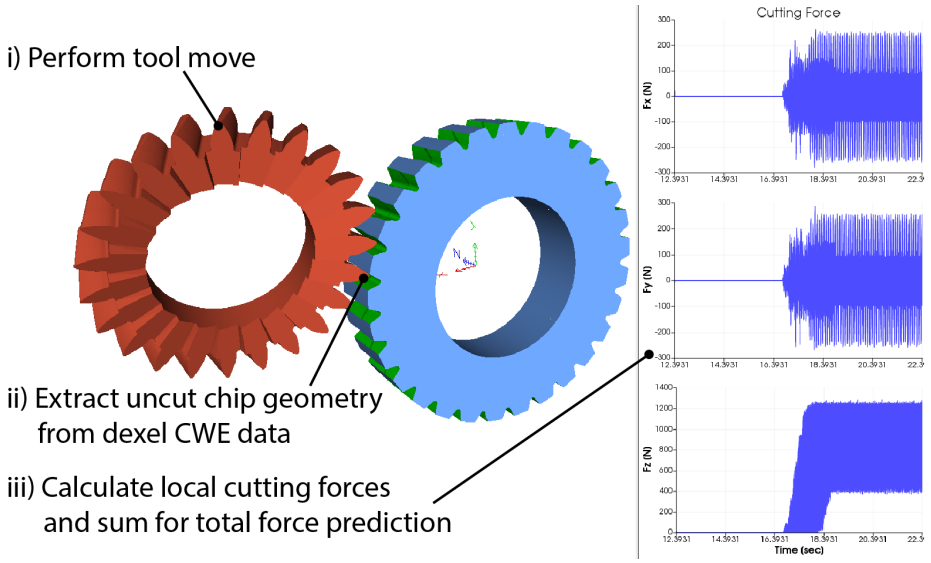

Figure 4.22: Cutting force predictions generated during simulation.

the chip geometry is extracted. Using the local cutting force conditions as calculated above in conjunction with the cutting force coefficients as described in Section 4.2, local predictions of cutting force are made for each node along the discretized cutting edge. The local cutting forces are then summed in order to generate a single cutting force prediction for the time step. This process is repeated for all time steps until the final specified gear is achieved. The time-domain simulation is integrated into a single program using ModuleWorks as its visualization engine, as shown in Figure 4.22.

4.7 Experimental Validation

As mentioned in Chapter 3, validation trials were performed at the University of Sheffield's Advanced Manufacturing Research Centre, on a DMG MORI NT5400 DCG mill-turn machine. In total, 25 trials were performed while taking cutting force measurements in order to validate the performance of the power skiving model.

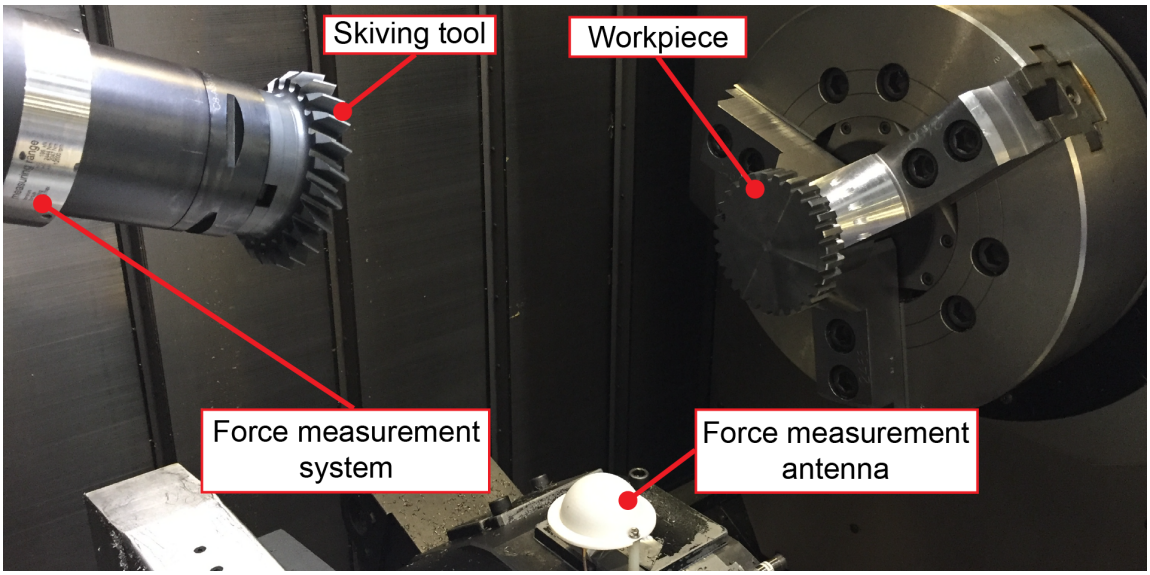

Figure 4.23: Experimental setup for power skiving cutting force measurement.

4.7.1 Experimental Trial Setup

The setup for the validation trials can be seen in Figure 4.23. The cutting tool was mounted to a pro-micron SPIKE, which is a wireless unit that captures bending moment data using strain gauges. The SPIKE system acts as an extension of the tool holding interface of the main spindle of the mill-turn machine. The workpiece was mounted in a secondary spindle capable of rotating synchronously with the main tool spindle. To receive the data, an antenna was mounted in close proximity to the working area of the process; however, a small number data points was lost during the trials.

The workpiece used for the trials is a 3.9mm module, 29-tooth external spur gear. Since the gear was not intended to be an operational part, the workpiece has minimal features, as can be seen in Figure 4.24. The 22.75mm-wide working area originally had a diameter of 121.15mm, and for the trials was machined to its final diameter of 120.9mm on the mill-turn machine in order to have the area concentric with the rotating axis. The 90mm-diameter feature is used for clamping the workpiece onto the secondary spindle. The material of the workpieces is EN24T steel (equivalent to

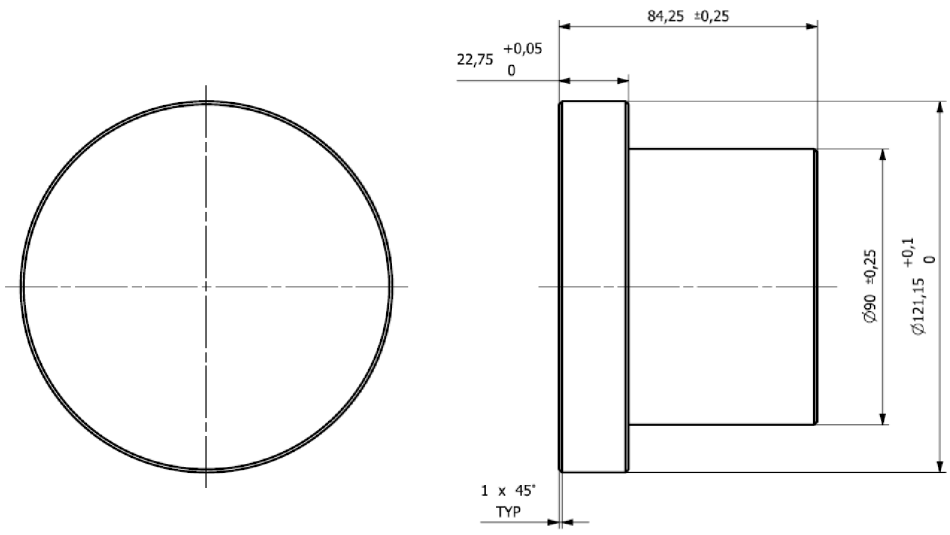

Figure 4.24: Workpiece geometry for power skiving trials.

AISI4340). The geometry of the gear being cut into the workpiece is summarized in Table A.1, part of Appendix A.

Two cutting tools were used during the trials, one fabricated by Dathan Tool and Gauge and the other by Sandvik Coromont. Both were designed specifically for the workpiece being fabricated; however, there are differences in tool design between the two manufacturers. Table A.2 in Appendix A outlines the geometry of each of the cutting tools used. While both have the same helix angle ($\beta_c = 20°$), compared to the Dathan tool, the Sandvik tool has fewer teeth (21 as compared to 23) and a larger rake angle (10° as opposed to 5°). As was observed during the trials, the differences had a noticeable effect on the cutting forces. Furthermore, the Sandvik tool has geometry that varies from the theoretical nominal geometry of a cutter with its attributes (smaller r_{ac}, narrower teeth), and thus there was uncertainty when modelling the tool in the power skiving simulations.

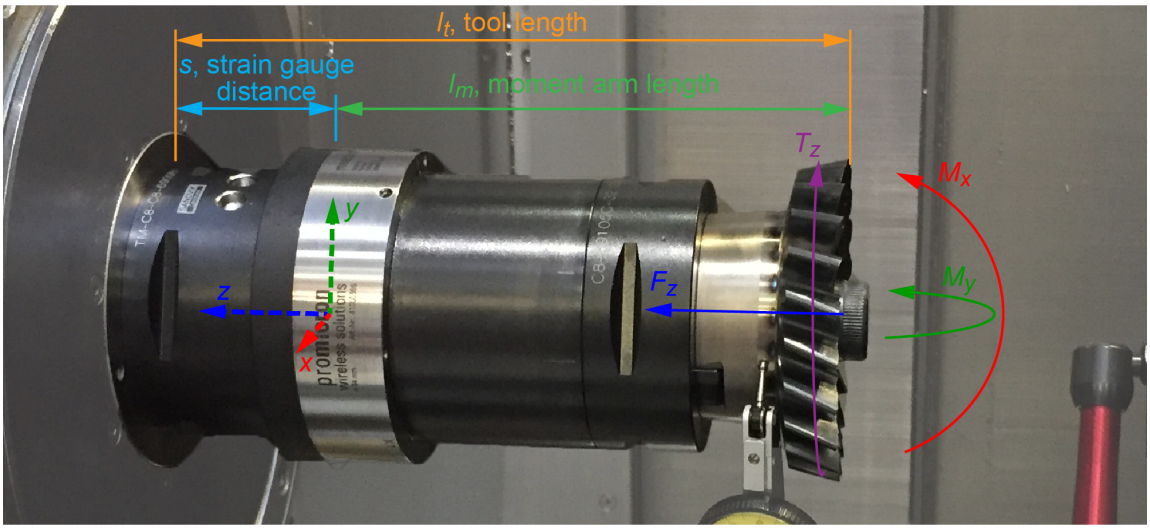

Figure 4.25: Overview of the SPIKE system and its dimensions.

4.7.2 Data Processing of Force Measurements

The raw data captured by the SPIKE system is a combination of bending moments and force readings measured using strain gauges placed at a specified location on the tool holder. The four readings given by the SPIKE system are x-axis moment (M_x), y-axis moment (M_y), z-axis torque (T_z), and z-axis force (F_z). Figure 4.25 shows the major geometry of the SPIKE and the readings it provides. All the axes can be seen to have an amount of noise resulting from the instrumentation. It can be observed that the F_z data is particularly noisy, due to the fact that the axial force is reconstructed from strain gauge readings, and due to the bending of the tool holder causing additional axial forces to be read.

An example of the data collected can be seen in Figure 4.26. The data was captured at the largest possible frequency achievable by the system ($f_s = 2.5$kHz), meaning that the number of data points (n_p) for each pass of a cutting tooth would be as follows:

$$n_p = \frac{f_s}{\omega_c N_c} \tag{4.47}$$

The measurement system directly provides F_z force readings; however, the bend-

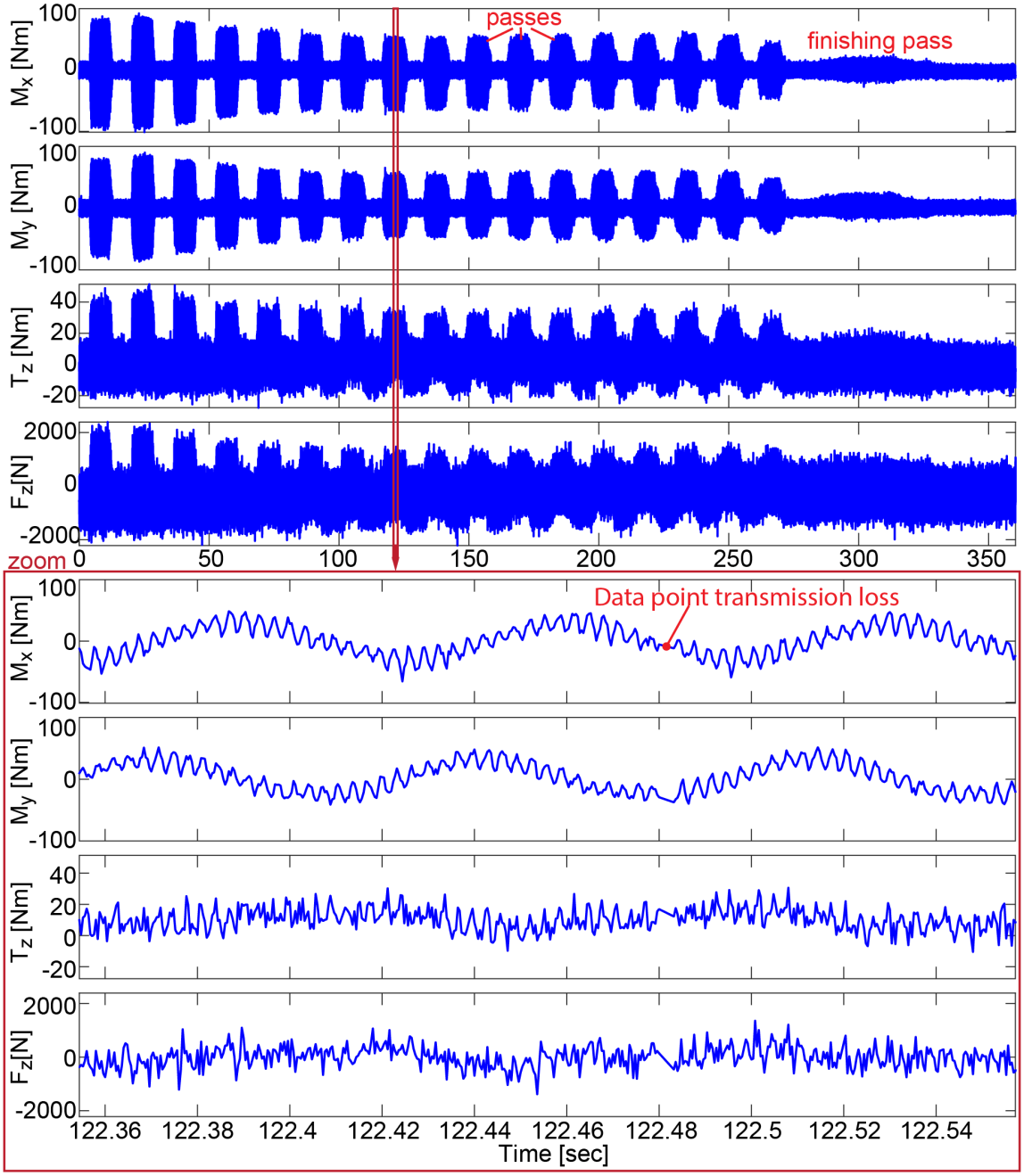

Figure 4.26: SPIKE system bending moment, torque, and force readings (Trial 8).

ing moments must be converted to represent forces. First, the moment arm must be calculated. Before the tool-and-SPIKE assembly was placed on the main spindle, the tool length (l_t) and radius were measured in a presetting tool. The distance of the strain gauges from the base of the measurement system is provided by pro-micron ($s = 50\text{mm}$), and thus the moment arm length (l_m) can be determined as follows:

$$l_m = l_t - s \tag{4.48}$$

With the moment arm length known, the conversion of the moment readings to force readings in the x and y directions (F_x and F_y, respectively) can be calculated:

$$\begin{aligned} F_x &= -M_y l_m \\ F_y &= M_x l_m \end{aligned} \tag{4.49}$$

Due to the amount of noise present in the F_z data, a moving average of the measured forces was used instead. To sufficiently smooth the data for later comparison with the process simulation, a moving average window of ten times the tooth passing period (t_p). The tooth passing period is the time between subsequent engagements each cutter tooth, and is defined as follows:

$$t_p = \frac{60}{2\pi\omega_c N_c} \tag{4.50}$$

Figure 4.27 shows the resulting cutting force measurements after conversion. It can be seen that the F_x and F_y data have noise which can be filtered out, and that the F_z data has the tendency to drift from its baseline value, for which a compensation can be performed.

To compensate for the drift in the z-axis force data, a simple linear compensation is used. Two points are taken at times between passes (t_0 and t_1) where the tool is not engaged with the workpiece and forces should be zero. A number of additional data points around the two selected points are used to calculate average force values ($\bar{F}_0$ and $\bar{F}_1$), which along with the selected times create a line describing the drift:

$$F_d(t) = m_d t + F_{d0} = \frac{\bar{F}_1 - \bar{F}_0}{t_1 - t_0} t + \left(\bar{F}_0 - \frac{\bar{F}_1 - \bar{F}_0}{t_1 - t_0} t_0 \right) \tag{4.51}$$

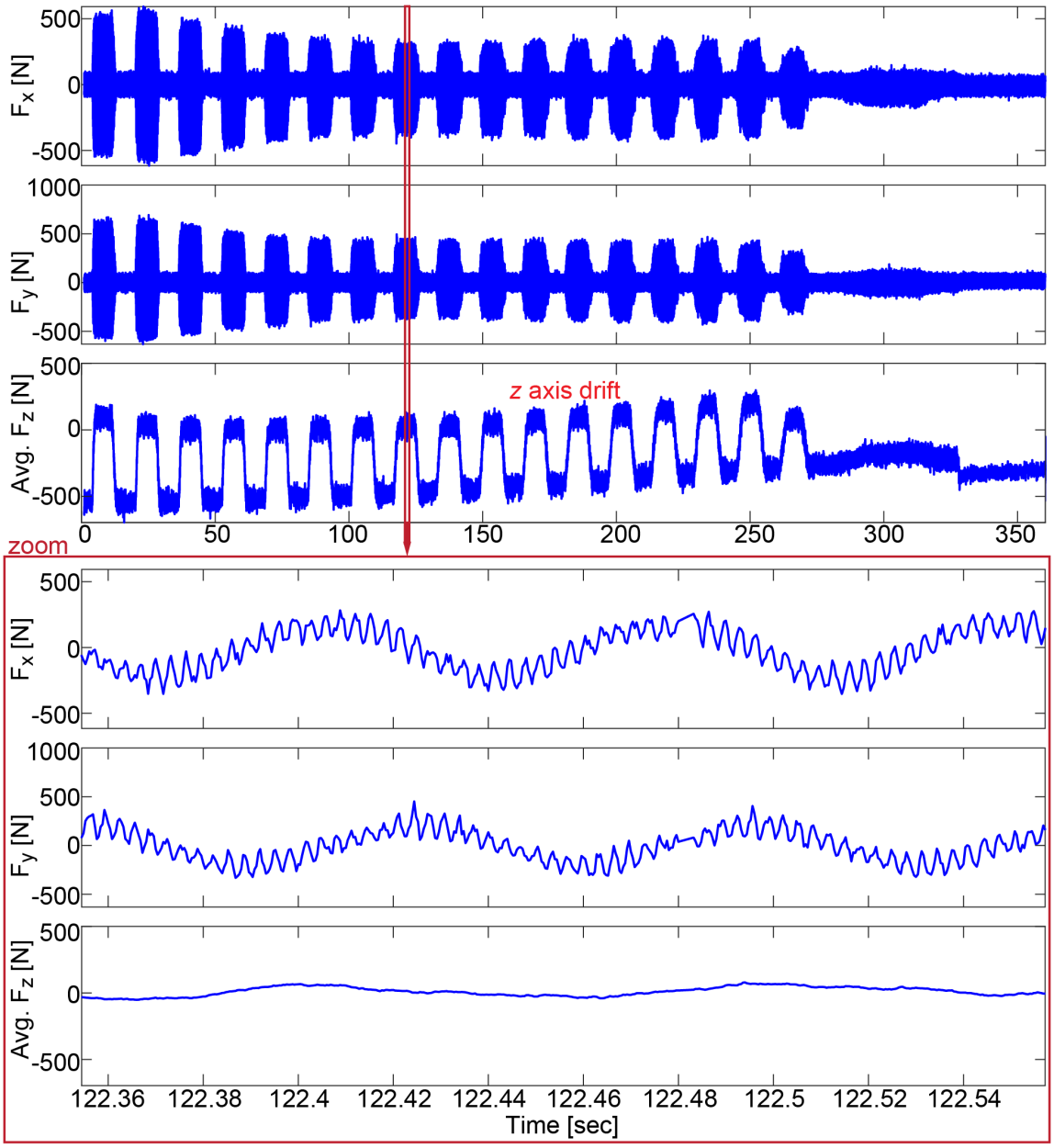

Figure 4.27: Initial calculated force measurements from the SPIKE system (Trial 8).

Using the linear drift from Equation (4.51), the drift can then be removed from the data. For this application, drift is only removed from the first selected point onward, which allows more complex cases of drift to use linear compensation in multiple sections. Figure 4.28 shows the removal of drift in the original force data (F_z) to create a new data set (F'_z) using this method:

$$F'_z(t) = F_z(t) - m_d t + F_{d0} \quad \text{where } t = t_0, ...t_n \tag{4.52}$$

In order to reduce the noise in the x and y axis cutting force data, a lowpass filter was applied to the data from the SPIKE system. Acceptable performance of the lowpass filter was achieved by using a Chebyshev design approach with a set pass band frequency (f_p) and stop band frequency (f_s) as follows:

$$f_p = \frac{1}{2\pi\omega_g} + \frac{1}{t_p} + 5 \text{ Hz} \tag{4.53}$$

$$f_s = \frac{1}{2\pi\omega_g} + \frac{1}{t_p} + 10 \text{ Hz} \tag{4.54}$$

4.7.3 Determination of Cutting Coefficients

To create initial cutting force predictions, the orthogonal-to-oblique cutting force coefficients for AISI5130, a material similar to the EN24T/AISI4340 workpiece material, were used. However, since the orthogonal-to-oblique model is derived from cutting experiments using a set rake angle, performance of the cutting force predictions is reduced in the case of large variations in rake and inclination angles, as are present in power skiving. Figure 4.30 shows the tendency of force predictions using orthogonal-to-oblique cutting coefficients to create large peaks not present in the measured data.

With the inadequate performance of the model using orthogonal-to-oblique coefficients, the Kienzle model is used instead. In general, the coefficients from this model are able to provide good cutting force predictions despite the variation in local cutting conditions. Initially, a set of Kienzle coefficients from the coefficient

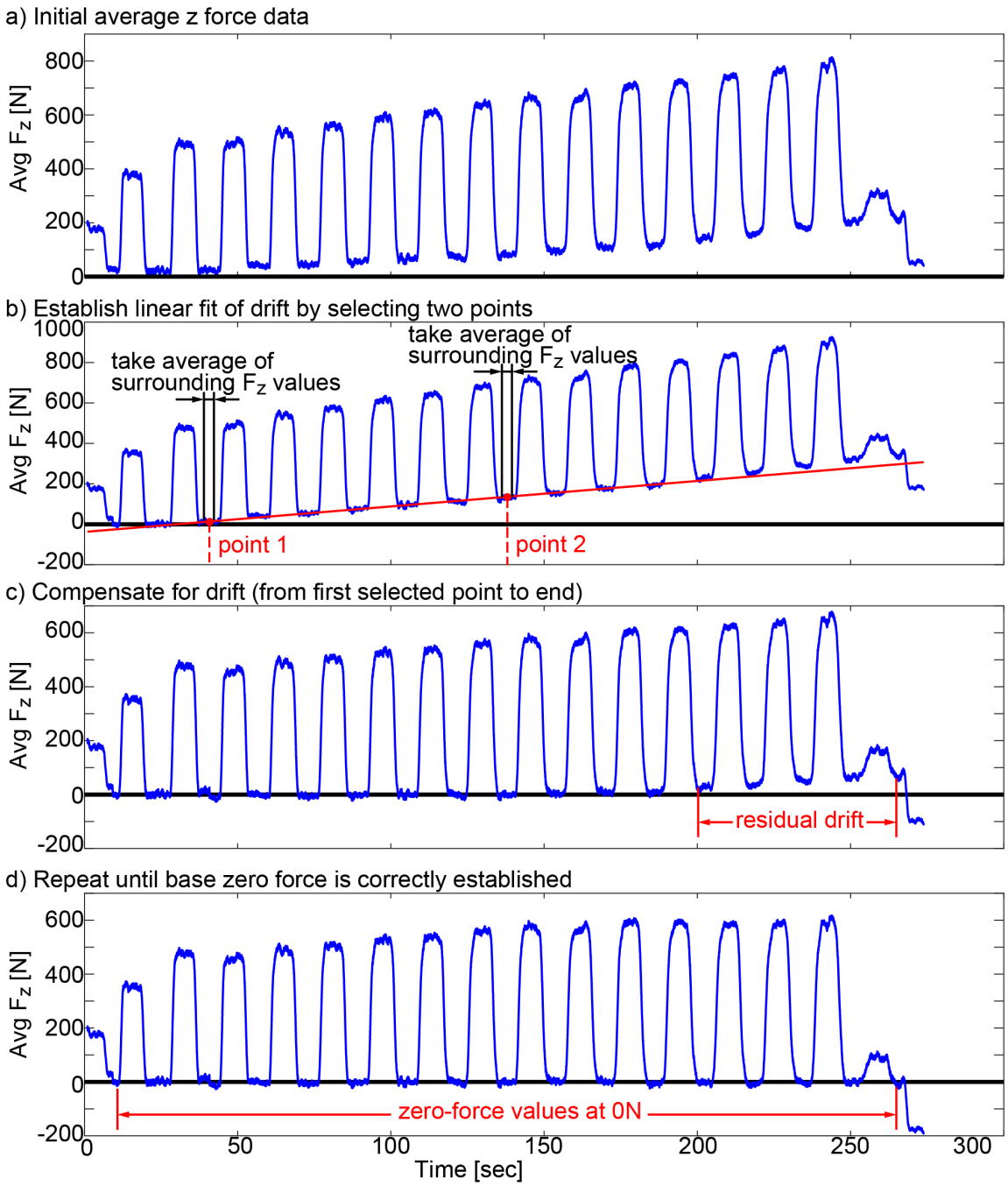

Figure 4.28: Drift compensation for SPIKE z-axis measurements (Trial 20).

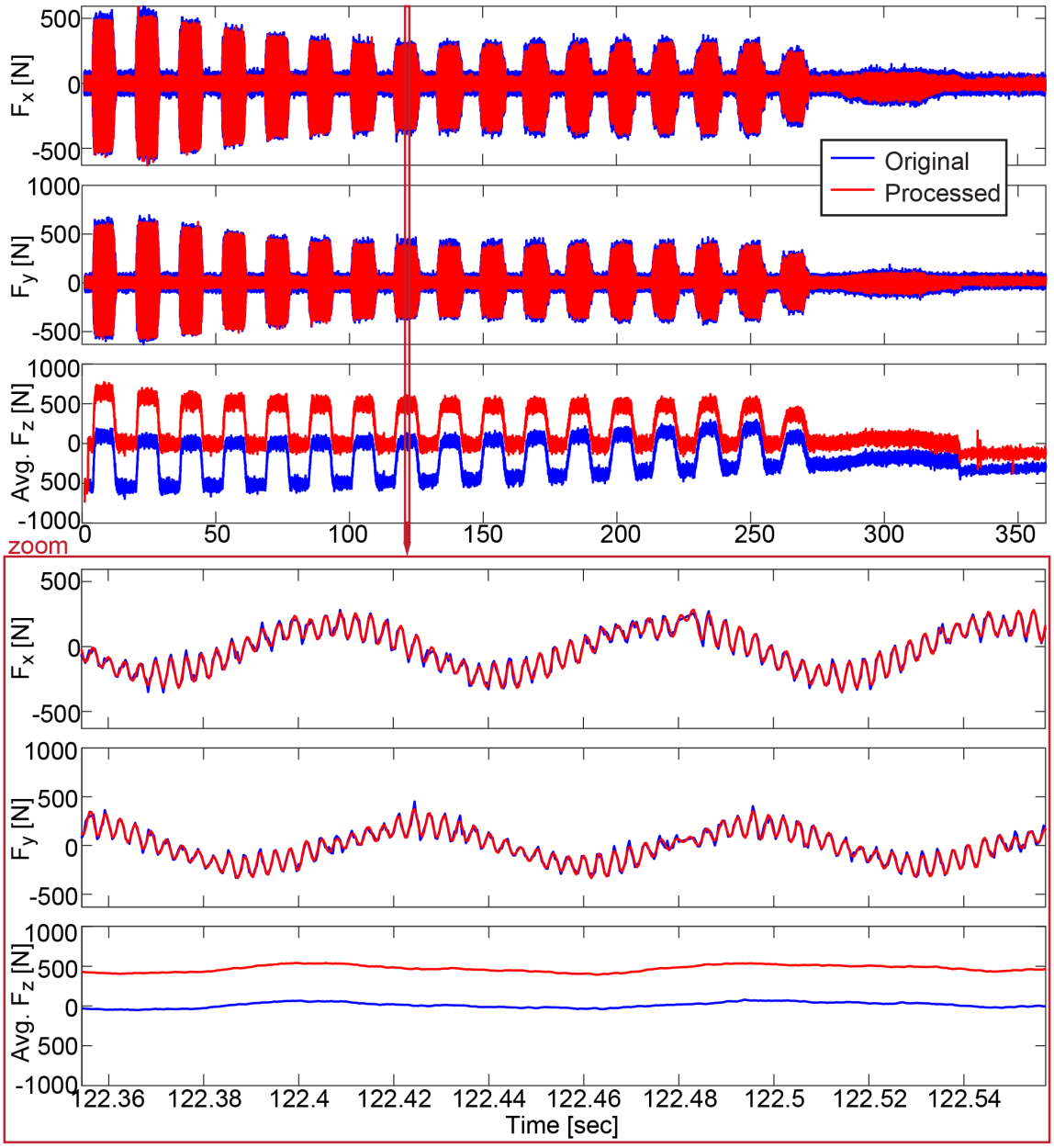

Figure 4.29: Processed force measurements from SPIKE data (Trial 8).

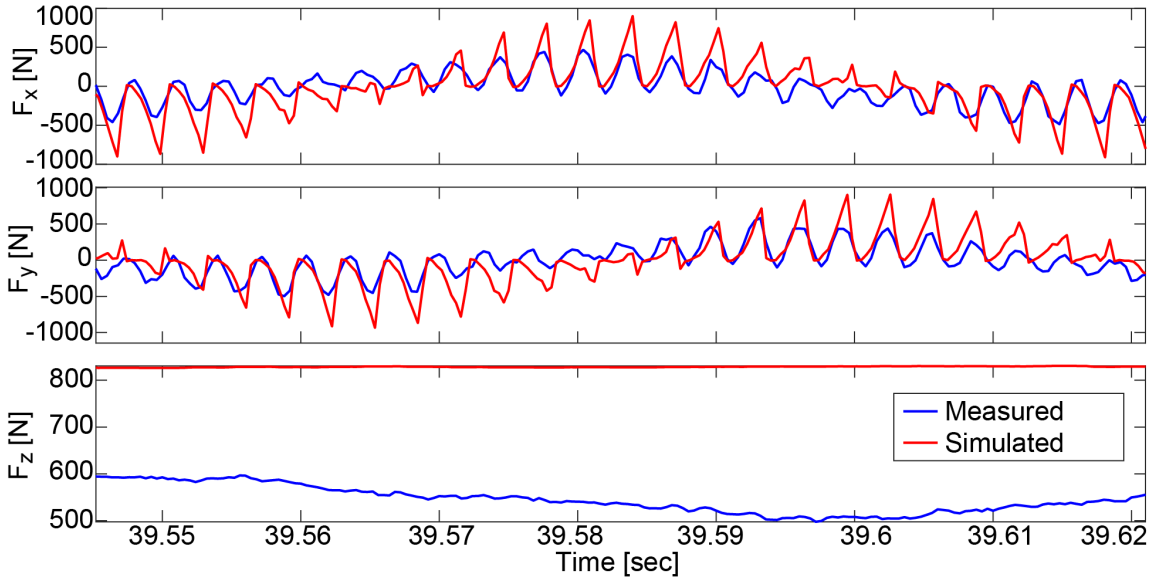

Figure 4.30: Peak force discrepancies using the orthogonal-to-oblique cutting model (Trial 8).

library of CutPro® [127] (a software developed by the Manufacturing Automation Laboratory at the University of British Columbia) was used. The coefficients from the software are a function of the cutting velocity (v_c in $\frac{\text{m}}{\text{min}}$), and can be found in Table 4.1.

While fairly accurate cutting force predictions are achieved using the CutPro® coefficients, a new set of Kienzle coefficients was also developed in order for the values to be tuned to accurately reflect the cutting conditions found in power skiving. To find a new set of coefficients, a set of data from one of the experimental trials (in this case, Trial 6) is chosen as the base measured data set. A simulation is run with the trial parameters to generate the local cutting component directions, including the force component directions ($\mathbf{t}$, $\mathbf{f}$, $\mathbf{r}$), the local rake angle (α_n), the local inclination angle (i), and the local chip width and thickness (b, h).

A four-dimensional search space is established for the Kienzle coefficients. For each coefficient, a starting value ($K_{u,0}$, u_0, $K_{v,0}$, v_0) and an end value ($K_{u,f}$, u_f, $K_{v,f}$, v_f) are selected based on likely values for the parameters. Intermediate values are

established by setting a regular interval for each of the coefficients.

$$\left.\begin{aligned} K_{u,s} &= K_{u,0},\ K_{u,1}, \ldots, K_{u,f} \\ u_s &= u_0,\ u_1, \ldots, u_f \\ K_{v,s} &= K_{v,0},\ K_{v,1}, \ldots, K_{v,f} \\ v_s &= v_0,\ v_1, \ldots, v_f \end{aligned}\right\} \tag{4.55}$$

For every possible combination of the Kienzle coefficients, a normalized RMS error value (e_t) is found by comparing forces calculated from the local simulation parameters to the measured set of data. Using the local cutting conditions exported from the simulation, local cutting force predictions for each engaged node on the cutter (j) are found for each time step (k) by using the geometric conversion from Kienzle to oblique coefficients from Equation (4.9):

$$\begin{bmatrix} F_x \\ F_y \\ F_z \end{bmatrix}_{j,k} = \begin{bmatrix} \hat{\mathbf{t}}bh & \hat{\mathbf{f}}bh & \hat{\mathbf{r}}bh \end{bmatrix}_{j,k} \begin{bmatrix} K_t c \\ K_f c \\ K_r c \end{bmatrix}_{j,k} \tag{4.56}$$

The total cutting force prediction is then found by summing the local cutting forces for all the engaged nodes at the time step:

$$\mathbf{F}_k = \sum_{j=1}^{n_{\text{nodes}}} \mathbf{F}_{j,k} \tag{4.57}$$

The error in each of the axis directions for each time step is found, and the values are normalized using the largest measured forces in each of the respective directions ($F_{x,\max}$, $F_{y,\max}$, $F_{z,\max}$):

$$\left.\begin{aligned} e_x &= \frac{F_{x,\text{meas}} - F_{x,\text{sim}}}{F_{x,\max}} \\ e_y &= \frac{F_{y,\text{meas}} - F_{y,\text{sim}}}{F_{y,\max}} \\ e_z &= \frac{F_{z,\text{meas}} - F_{z,\text{sim}}}{F_{z,\max}} \end{aligned}\right\} \tag{4.58}$$

The total RMS value of the normalized errors across all the time steps is then found:

$$e_t = \sqrt{\frac{1}{3n_{\text{steps}}}\left(\sum_{k=1}^{n_{\text{steps}}} e_{x,k}^2 + e_{y,k}^2 + e_{z,k}^2\right)} \tag{4.59}$$

The coefficients that result in the smallest e_t value are selected as the cutting coefficients. For the measured data from Trial 6, a search window with the following values was established:

$$\left.\begin{array}{cc} K_{u,0} = 400 & K_{u,f} = 1000 \\ u_0 = 0 & u_f = 1 \\ K_{v,0} = 1400 & K_{v,f} = 2000 \\ v_0 = 0 & v_f = 1 \end{array}\right\} \tag{4.60}$$

Additionally, for each step, the average local rake angle was calculated, and the forces were separated into two groups ($\alpha_n \geq 0$ and $\alpha_n < 0$). The results for these two sets of forces were analyzed independently to find a set of coefficients for each. A comparison between coefficients from the CutPro® software and the developed coefficients can be seen in Table 4.1. As can be observed, the coefficients determined from the measured data for Trial 6 are very similar to the coefficients from the software, especially considering the nominal cutting speed of $95\frac{\text{m}}{\text{min}}$.

4.7.4 Accuracy of Cutting Force Prediction

The measured and simulated cutting forces for Trials 7, 8, and 20 are compared here to show the accuracy of the cutting force predictions from the power skiving model. The tool and process parameters for these trials can be found in Appendix A. The data is compared using the RMS error values of the average cutting force of each tooth pass in each of the three axial directions as well as the peak cutting force of each tooth pass in the x and y directions (as the average z force was used for comparison due to the noise in the SPIKE data). A normalized error for each measurement is also calculated by dividing by the largest force in each of the respective axial directions.

Table 4.1: Cutting coefficients used for simulation of experimental trials.

Coefficient	MAL Library	Developed
if $\alpha_n \geq 0$		
K_u	$-0.84431v_c + 636.0384$	550
u	$-0.00012702v_c + 0.58017$	0.5
K_v	$-0.50863v_c + 1600.9745$	1700
v	$-0.00033348v_c + 0.25358$	0.2
if $\alpha_n < 0$		
K_u	$-0.86007v_c + 648.9746$	550
u	$-0.00062942v_c + 0.67863$	0.2
K_v	$-1.1995v_c + 1759.746$	1500
v	$-0.00038151v_c + 0.35419$	0.2

Table 4.2: Summary of prediction accuracy for Trial 7.

	x axis	y axis	z axis
Avg. RMS error [N]	23 (4.2%)	12 (5.1%)	60 (9.9%)
Peak RMS error [N]	56 (10.2%)	51 (11.4$)	–

A comparison of the results for Trial 7 can be found in Figure 4.31, with the corresponding error values in Table 4.2. For this trial, the coefficients developed from Trial 6 are used in the simulation. The resulting cutting force predictions are quite close to the measured results, with the average RMS errors being within 4–6% for the x and y axes and 10% for the z axis. The peak RMS errors are also within 10–12%. The present discrepancy could be due to a number of factors, including tool deflection or vibration, noise from the measurement system, and inherent error in the calculated cutting force coefficients. However, the results for this trial demonstrate that the model can quite accurately predict cutting forces in power skiving.

Similar to Trial 7, the coefficients used in the Trial 8 simulation are the ones developed from the Trial 6 force measurements. In this trial, the depths of cut for

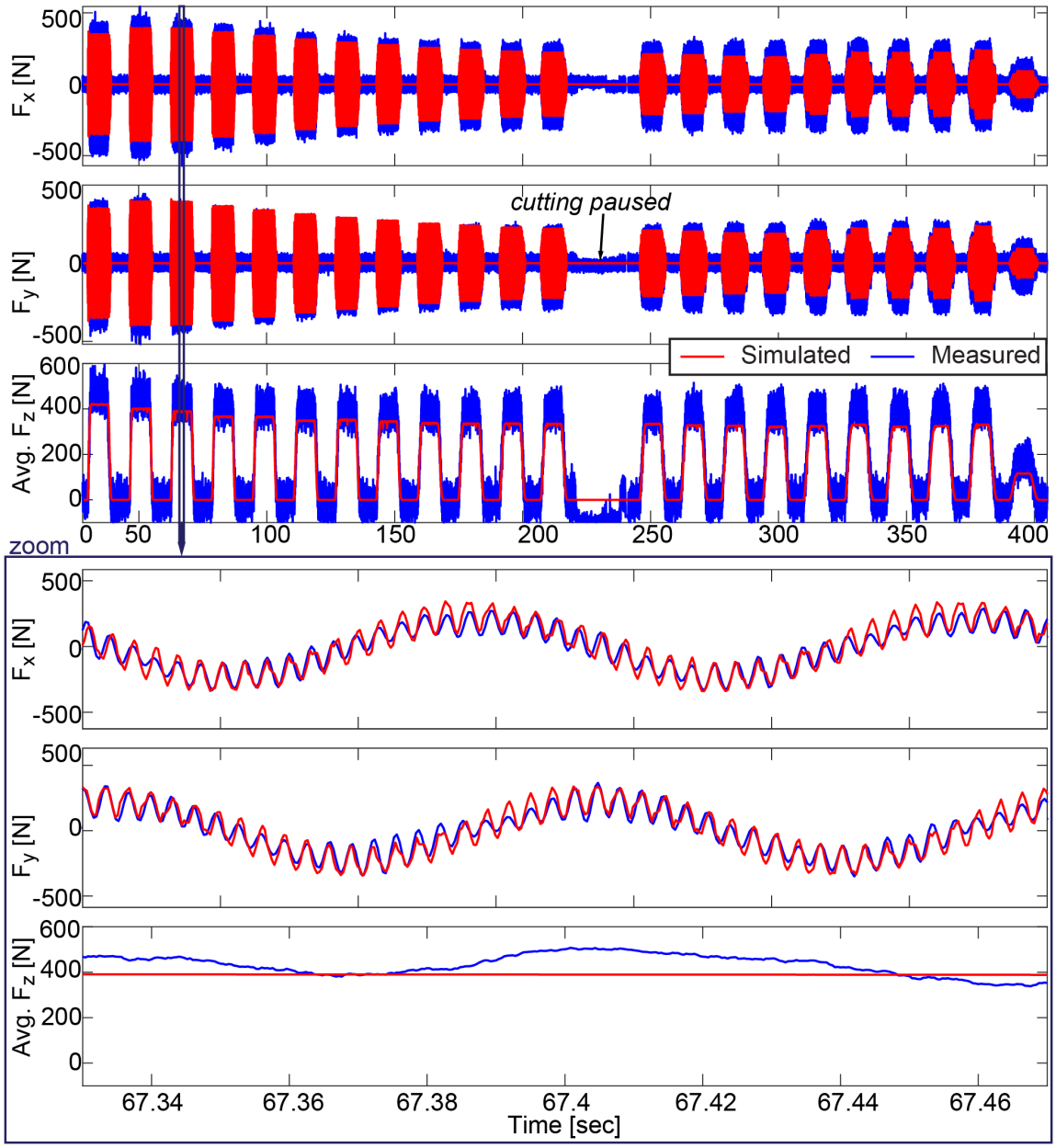

Figure 4.31: Comparison of simulated and measured cutting forces for Trial 7.

Table 4.3: Summary of prediction accuracy for Trial 8.

	x axis	y axis	z axis
Avg. RMS error [N]	40.41 (6.9%)	35.94 (5.7%)	57.45 (7.4%)
Peak RMS error [N]	83.01 (14.2%)	78.65 (12.5$)	–

each pass were larger than those found in Trial 7, resulting in higher cutting forces. The cutting force predictions from the simulation remain reasonably accurate (as can be seen in Table 4.3). However, Figure 4.32 shows that the forces during the final pass – a finishing pass with reduced axial feed rate and small cutting depth – are not captured accurately. This is due to the heightened requirements for dexel and time step resolutions (ie., smaller dexel spacing and smaller time steps) in order to correctly capture the thin chips created from a finishing pass. Furthermore, the cutting force coefficients may not be adequately tuned to capture the forces of a finishing pass. This demonstrates the need for further research into the accurate modelling of processes that include these finishing passes.

The measured and simulated cutting forces for Trial 20 are also compared. Unlike the previous two trials, Trial 20 used the Sandvik cutting tool, as well as a different tool speed (957rpm vs 841rpm for the previous trials). The CutPro® force coefficients were used in this case, as they resulted in reduced error compared to the calculated coefficients. The resulting simulated cutting forces (see Figure 4.33 have large peaks and do not match the measured data very well. Table 4.4 shows that the peak RMS error reached more than 20% of the maximum forces in the x and y axes, which is a notable discrepancy. The differences between the measured and simulated forces are theorized to be mainly due to a lack of available geometry data for the cutting tool (there are unknown profile modifications made to the Sandvik tool which were estimated for the simulation) and the differences in the cutting conditions causing the coefficients to not be as accurate.

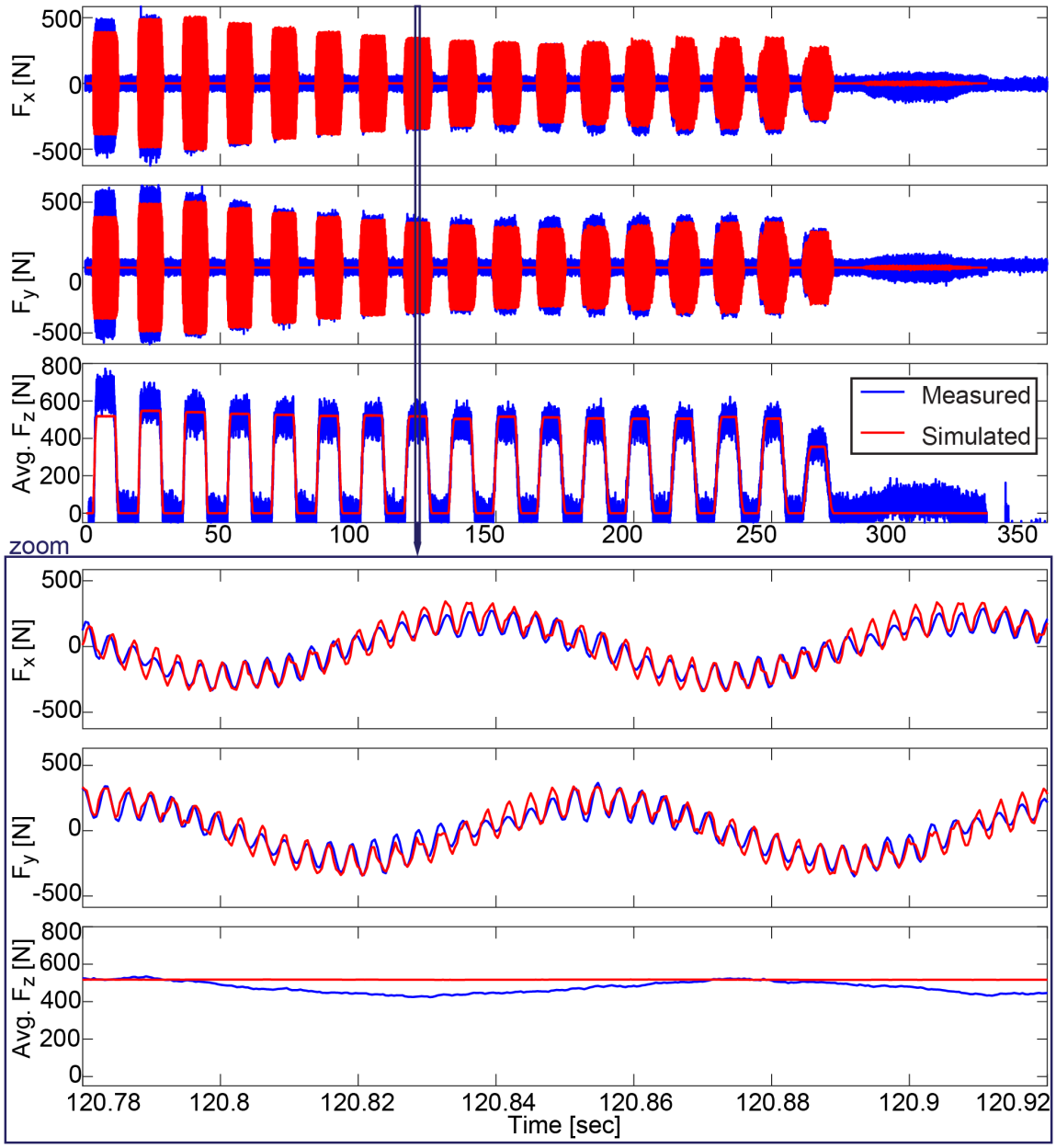

Figure 4.32: Comparison of simulated and measured cutting forces for Trial 8.

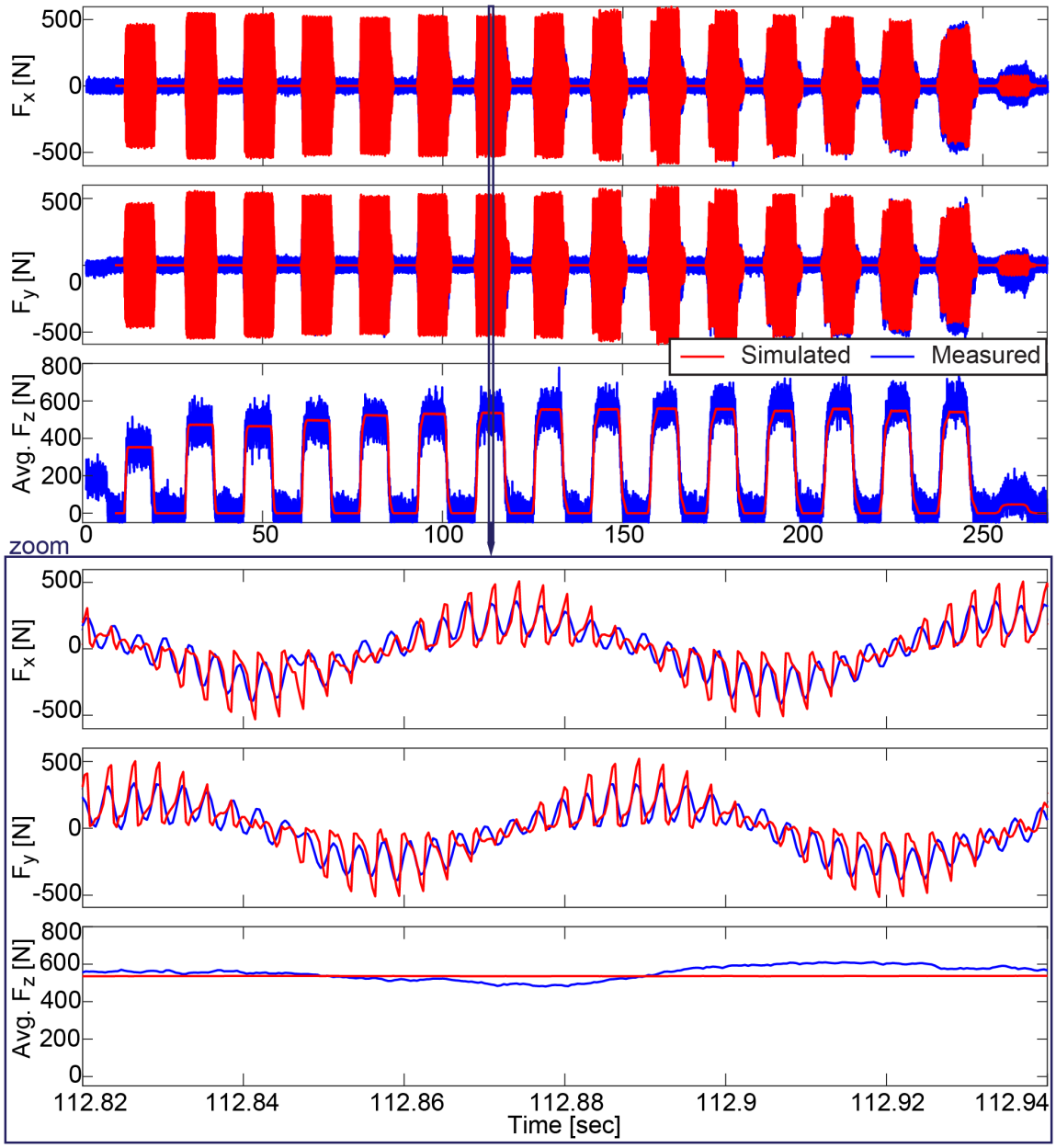

Figure 4.33: Comparison of simulated and measured cutting forces for Trial 20.

Table 4.4: Summary of prediction accuracy for Trial 20.

	x axis	y axis	z axis
Avg. RMS error [N]	43.25 (8.0%)	45.06 (8.6%)	52.83 (6.8%)
Peak RMS error [N]	111.48 (20.6%)	114.95 (21.9$)	–

4.8 Conclusions

In this chapter, the development of cutting force predictions for the virtual model was presented. The uncut chip geometry is successfully extracted at each step of a time domain simulation using a dexel-based CWE calculation engine. A 2D cross section of the chip geometry is found, and the local kinematics and geometry are used to apply a force model to resolve the local cutting forces. The forces are then summed to create a total cutting force prediction. A set of coefficients is generated from experimental trial data, and the comparison of the simulated and measured forces from a number of power skiving trials shows that the cutting forces can be successfully predicted using the virtual power skiving model.

Chapter 5

Process Planning Using Virtual Model

5.1 Introduction

Traditionally, power skiving processes have been planned using iterative methods wherein process parameters are chosen (usually based on previously implemented values), then tested and adjusted repeatedly until a satisfactory process has been achieved. This approach requires a significant investment of time and material, which is undesirable in industrial practice. Therefore, a more focused approach to process planning has been developed using the virtual power skiving model. The basis of this method of process planning is the prediction data obtained through the simulation of a skiving process with a gradual radial feed. The predictions from this process could then be used to predict the cutting conditions for a cutting pass of a given depth. This approach was used to develop the cutting depths of passes for several processes while limiting the average total cutting force experienced by the tool in an effort to reduce tool wear.

This chapter covers the use of the virtual model as a tool to plan power skiving processes. Section 5.2 presents an improvement of the computational efficiency of the model using a partial workpiece in order to increase the practical feasibility of

the model as a process planning tool. Section 5.3 demonstrates a method of process planning for power skiving using simulations with gradual radial feeds to generate data from which cutting-force-limited process parameters can be found.

The author would like to acknowledge that both the main topics of this chapter are implementations of ideas first proposed by Dr. Luke Berglind of the Advanced Manufacturing Research Centre at the University of Sheffield as part of a collaborative research effort on the topic power skiving.

5.2 Simulation Efficiency Improvement

The CWE calculation is the most computationally demanding task when modelling the power skiving process. This causes simulations using the power skiving model to take, in many cases, more than an hour to be performed. For the virtual model to be more effectively used as a process planning tool, a strategy to reduce the simulation time for cutting force prediction was developed. Using a partial workpiece representation to find the cutting forces for a single tooth gap and then superposing that result to simulate the cutting of the other gear teeth, a more computationally efficient model can be used to predict cutting forces in a power skiving process.

5.2.1 Cutting a Partial Workpiece

The partial workpiece in the multi-dexel engine is represented as a section of the original workpiece that is large enough to accommodate the cutting of a single tooth gap, as demonstrated in Figure 5.1a. The size of the section is defined by the angular pitch (the tooth-to-tooth angle) of the gear, calculated as follows:

$$\theta_N = \frac{2\pi}{N} \tag{5.1}$$

When the partial workpiece is used in the simulation, CWE calculations (as well as subsequent cutting force prediction calculations) are only performed while the single tooth gap is being cut. The end result of the simulation is thus only a portion

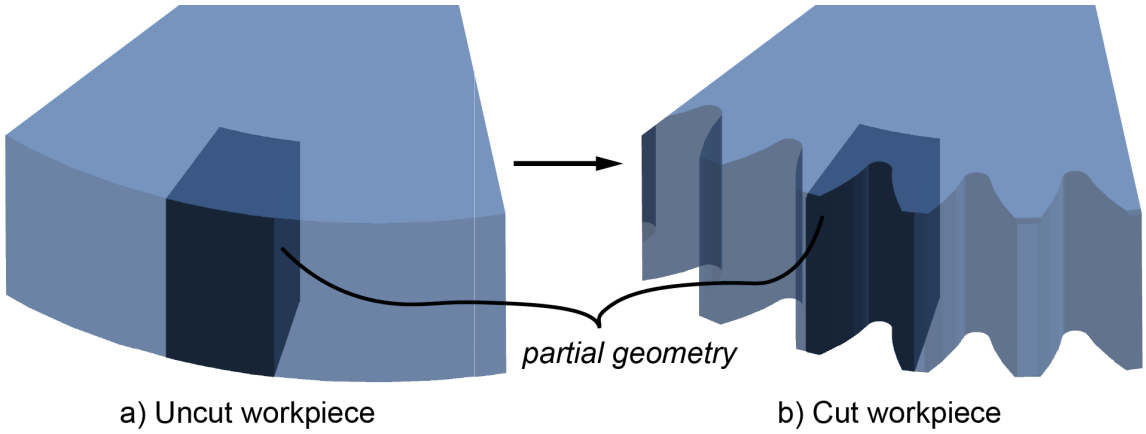

Figure 5.1: Partial workpiece used to decrease CWE computation time.

of the gear in the section of the workpiece, as shown in Figure 5.1b. The resulting cutting forces from the partial simulation must be processed by superposition to create an estimate of the cutting forces for a full workpiece.

5.2.2 Superposition of Partial Workpiece Results

The "single tooth data" resulting from the partial workpiece simulation (see Figure 5.2) forms the basis of the estimation of cutting forces for the same cutting process applied to the full workpiece.

The single tooth data generated by a partial workpiece simulation consists of short periods of cutting force predictions separated by larger periods of no cutting forces. For consistency in tool positions during simulation, the time step for each simulation is defined as a fraction of the tooth passing period. The period between the predicted single tooth passes (the gear rotation period t_g) is therefore based on the tooth pass period (t_p) and the number of teeth in the workpiece:

$$t_g = t_p N_g \tag{5.2}$$

To determine the cutting forces for the workpiece teeth that are not modelled, the cutting force data could simply be duplicated with an added time shift of t_p.

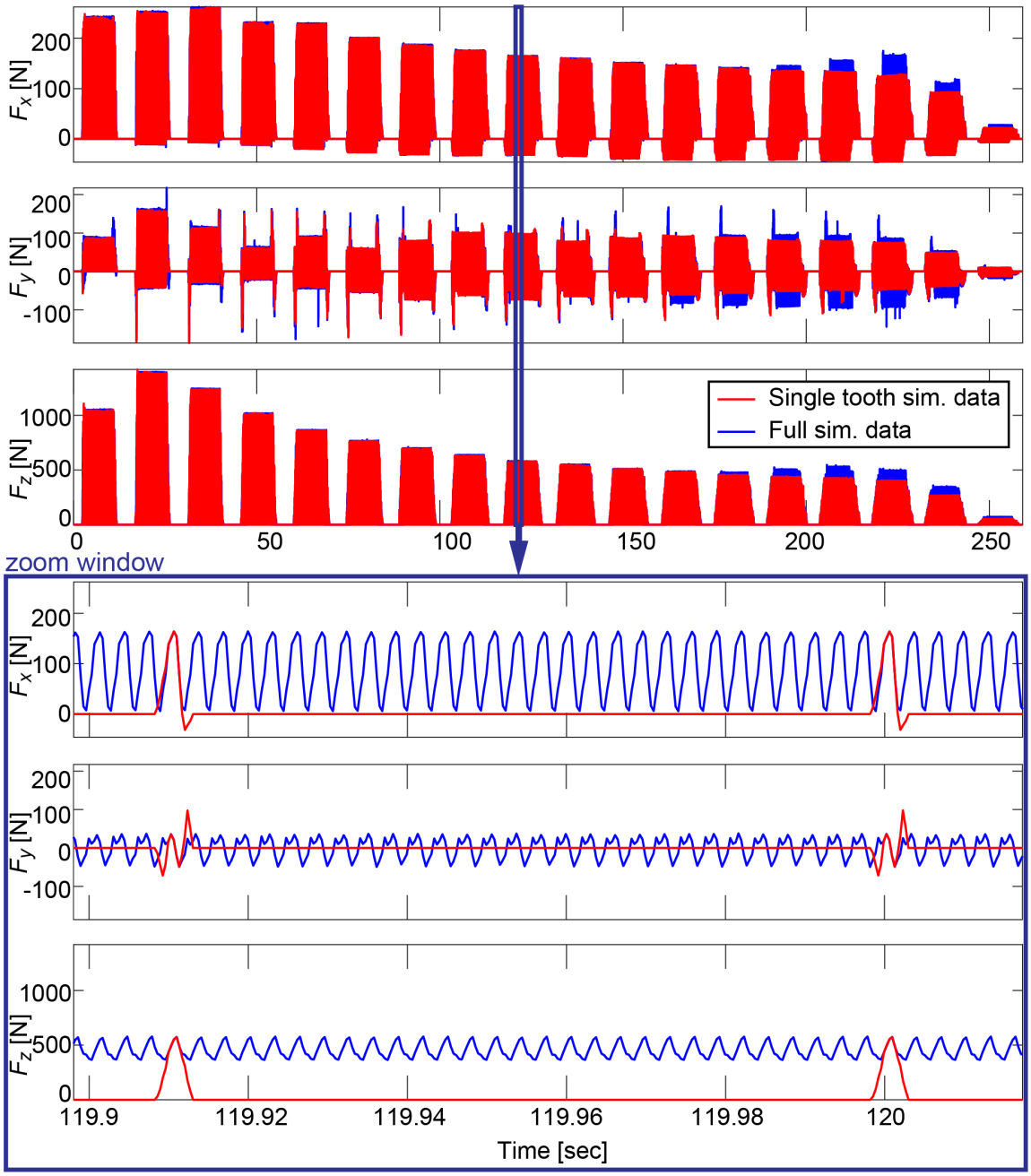

Figure 5.2: Comparison of cutting force predictions from partial and full workpiece simulation for Trial 8.

However, during a pass, the cutting tool is not fully engaged as it enters and as it exits the workpiece, resulting in a region of transient behaviour for the cutting forces. To better capture these effects, linear relationships are established between each data point for the partial workpiece simulation ($F|_{t=t_i}$) and its associated point on the proceeding tooth pass ($F|_{t=t_i+t_g}$), when the cutter is at the same rotary position during the cut. First, the difference in cutting force between points is found:

$$\Delta F_i = F|_{t=t_i+t_g} - F|_{t=t_i} \tag{5.3}$$

A linear relationship is established between the data point and the proceeding associated point, as seen in Figure 5.3a. The estimated forces for the unmodelled tooth gaps are then derived by interpolating between the two nominal points using a linear relationship, with the result of Equation (5.3) being used to derive the slope:

$$F_i' = F_i + \frac{\Delta F_i t_p k}{N_g}, \quad k = 1, 2, \ldots, N_g - 1 \tag{5.4}$$

Figure 5.3b shows the resulting data points for a single point-to-point interpolation. These intermediate points are used to create the cutting force data profiles for the unmodelled portion of the workpiece.

The cutting force profiles from each of the repeated instances of the single-tooth cutting force data are then summed together, creating a final estimation of the cutting forces from a complete workpiece, as shown in Figure 5.3c.

5.2.3 Results of Partial Workpiece Simulation

Cutting force predictions from simulations using the partial workpiece closely match those resulting from a full simulation, as can be observed in Figure 5.4. In the steady-state portion of cutting, where the cutting tool is fully engaged with the workpiece, the difference between the two simulations is around 2–7%. Much of this error is due to the transient portions of the cut at the start and end of a pass, when the cutter is not fully engaged with the workpiece. Furthermore, trials with lower axial feed rates (ie., Trial 1, Trial 3, Trial 4, Trial 5, etc.), and thus with

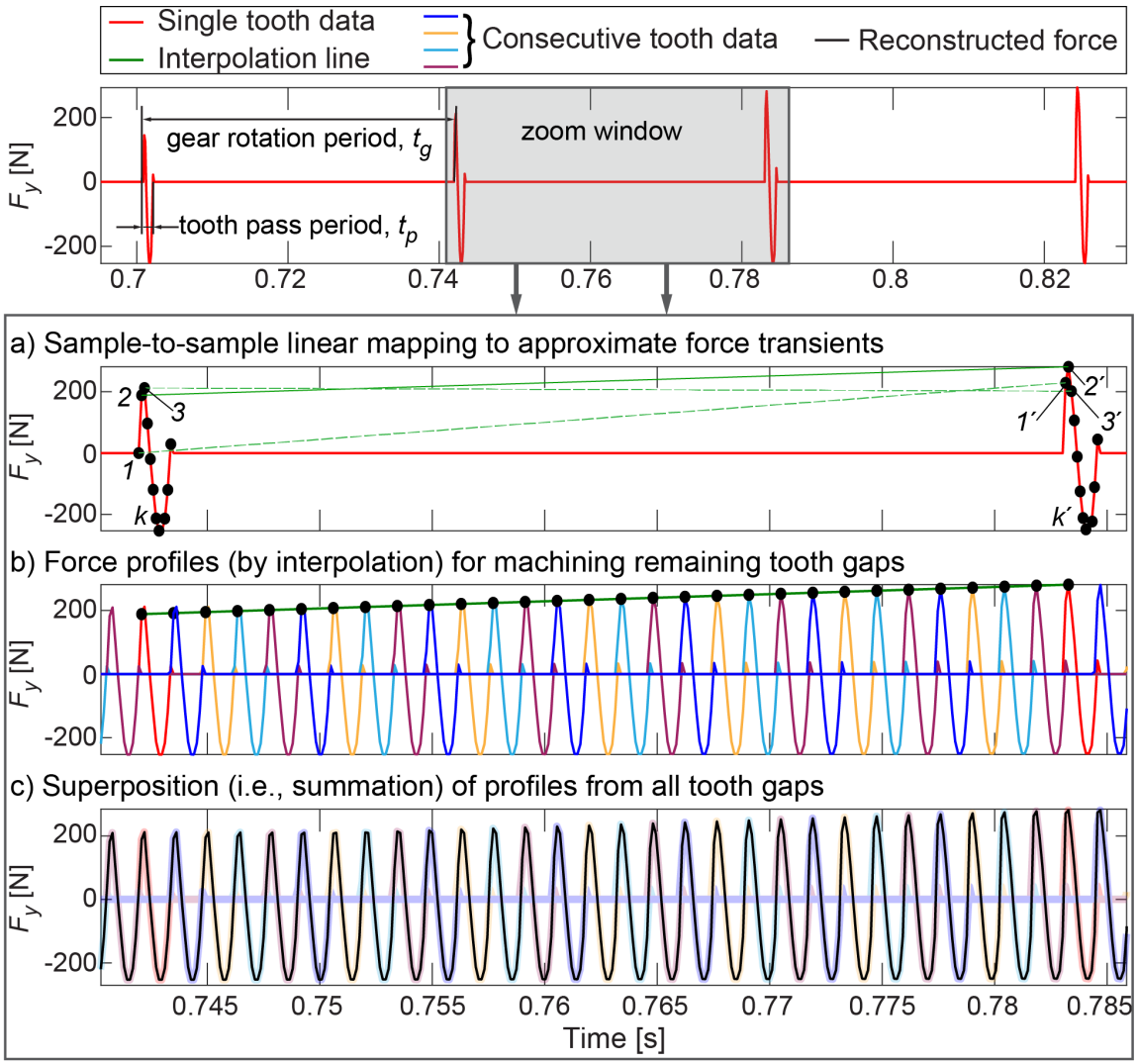

Figure 5.3: Method of using partial simulation to estimate full simulation cutting force results.

smaller chip thicknesses, showed a larger amount of variation. This is likely due to the fact that, in order to compare the cutting times, the full workpiece simulations were performed at lower than desired time and dexel resolutions, resulting in more numerical instability in finding the uncut chip geometry of a thinner chip. Table 5.1 summarizes the differences between cutting force prediction using each of the two approaches for a number of cases.

As a result of the reduced CWE engagement calculations, simulations using a partial workpiece reduced the total simulation time by 93–94% compared to simulations with a full workpiece. A comparison of simulation times for a number of cases is presented in Table 5.3.

The partial workpiece method for predicting cutting forces is useful for the planning and improvement of power skiving processes, as the large reduction in simulation time allows for more rapid iteration of the process parameters. However, while the method allows for the faster prediction of nominal cutting forces in a given process, additional effects such as elastic tool deformation and vibration are not possible. Therefore, a stable cut with negligible tool or workpiece deflection must be assumed when using the partial workpiece geometry simulation, and further investigation into form error and process stability must be performed with a different approach.

5.3 Process Planning Using Gradual Radial Feed

An important use of virtual process models is the ability to plan a machining operation without running numerous real-world tests. This saves the time and cost of using the machine to run repetitive trials in order to observe the effects of changing operating parameters. Furthermore, a robust virtual model will be able to adjust process parameters such as the depth of cut or chip load in order to limit adverse effects such as tool wear.

Using the developed power skiving model, an initial attempt at a process planning module was created. The planning of a power skiving process uses the results of a simulation to characterize the cutting forces in response to the cutting depth. This

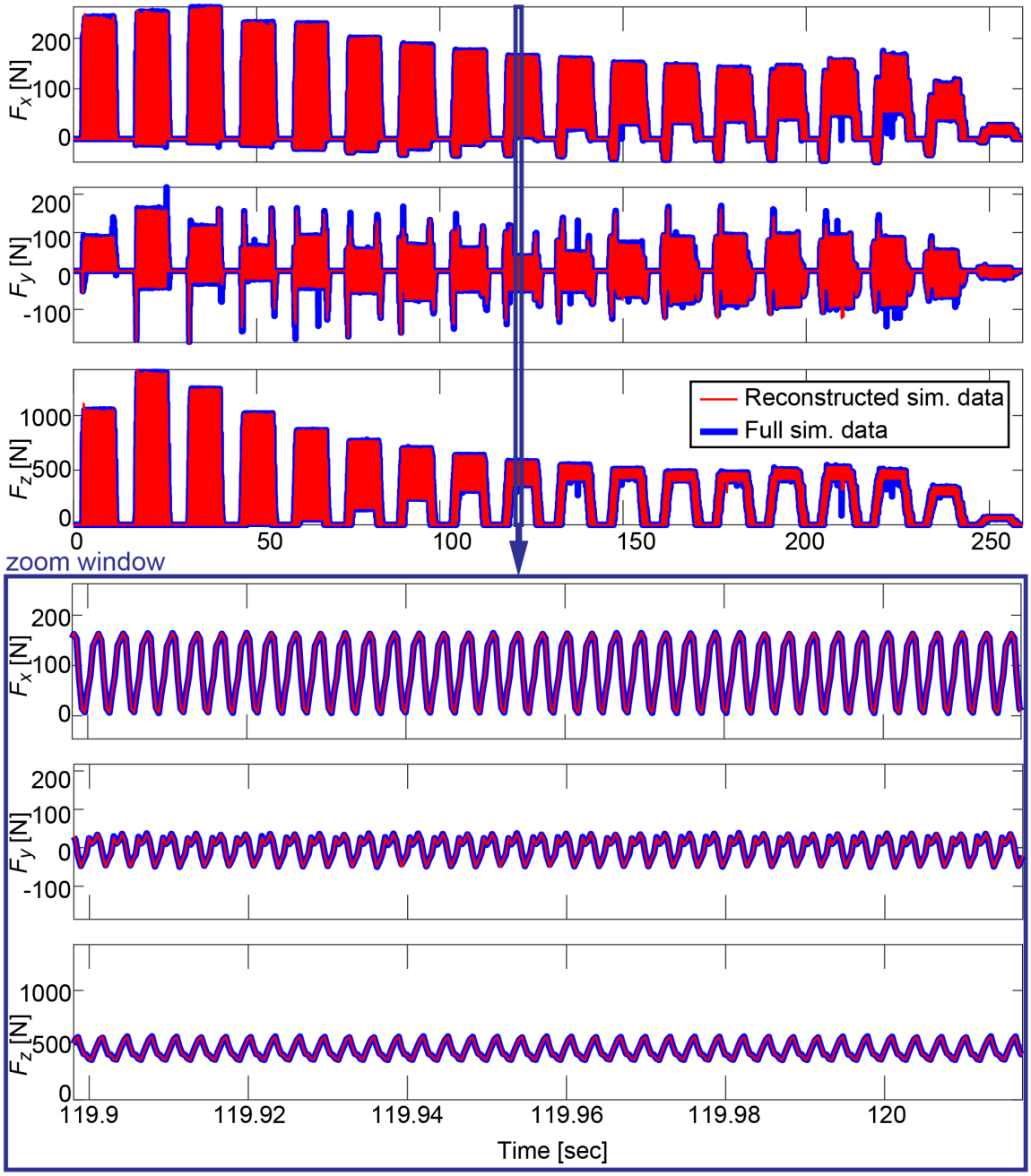

Figure 5.4: Comparison of cutting force predictions from full and partial workpiece simulations for Trial 8.

Table 5.1: Prediction differences due to partial workpiece simulation.

	Avg. RMS error [N]		
Test case	x axis	y axis	z axis
Trial 1	11.18 (7.80%)	11.18 (7.32%)	22.54 (6.89%)
Trial 2	12.38 (2.52%)	12.38 (2.54%)	26.02 (2.09%)
Trial 3	14.96 (8.56%)	14.96 (8.93%)	37.89 (7.84%)
Trial 4	8.08 (7.16%)	8.08 (7.52%)	18.01 (6.63%)
Trial 5	14.55 (7.91%)	14.54 (8.43%)	34.78 (8.03%)
Trial 6	14.14 (2.22%)	14.15 (2.22%)	34.26 (1.90%)
Trial 7	12.87 (2.69%)	12.88 (2.70%)	26.68 (2.21%)
Trial 8	13.32 (2.58%)	13.31 (2.57%)	29.96 (2.17%)
Trial 9	14.74 (2.74%)	14.76 (2.75%)	32.98 (2.18%)
Trial 10	15.82 (2.70%)	15.87 (2.72%)	37.67 (2.30%)
Trial 11	12.01 (2.25%)	12.00 (2.27%)	25.29 (2.24%)
Trial 12	13.68 (7.61%)	13.69 (7.41%)	25.97 (7.09%)
Trial 13	7.04 (6.45%)	7.04 (6.20%)	11.19 (4.72%)
Trial 14	13.44 (2.57%)	13.45 (2.55%)	28.40 (2.76%)
Trial 15	12.96 (7.08%)	12.96 (6.85%)	24.19 (5.88%)
Trial 16	7.41 (6.49%)	7.41 (6.76%)	12.10 (5.20%)
Trial 17	13.30 (2.49%)	13.31 (2.52%)	27.18 (2.43%)
Trial 18	12.88 (7.11%)	12.88 (7.57%)	23.55 (6.43%)
Trial 19	6.74 (6.28%)	6.74 (6.03%)	10.67 (5.68%)
Trial 20	13.59 (2.19%)	13.61 (2.11%)	31.20 (2.28%)
Trial 21	15.62 (7.74%)	15.61 (8.05%)	31.94 (7.62%)
Trial 22	13.75 (2.21%)	13.75 (2.26%)	31.10 (2.27%)
Trial 23	15.71 (7.78%)	15.71 (7.36%)	30.57 (7.28%)
Trial 24	13.52 (2.18%)	13.52 (2.20%)	31.11 (2.27%)
Trial 25	15.47 (7.96%)	15.48 (8.44%)	30.22 (7.05%)

Table 5.3: Comparison of full and partial simulation times.

Test case	Full sim. time [sec]	Partial sim. time [sec]	Time reduction [%]
Trial 1	17339	1097.01	93.67
Trial 2	6944.88	459.95	93.38
Trial 3	10690.80	689.62	93.55
Trial 4	32389.00	1698.57	94.76
Trial 5	9828.61	627.06	93.62
Trial 6	4651.93	282.22	93.93
Trial 7	6813.43	439.87	93.54
Trial 8	5215.13	341.26	93.46
Trial 9	4600.70	319.77	93.05
Trial 10	3825.17	281.24	92.64
Trial 11	6011.83	324.81	94.60
Trial 12	16402.10	1023.04	93.76
Trial 13	47534.50	2584.85	94.56
Trial 14	5528.79	343.2	93.79
Trial 15	17196.60	928.12	93.60
Trial 16	45578.00	2333.72	94.88
Trial 17	5843.03	343.29	94.12
Trial 18	14582.50	834.72	94.28
Trial 19	34131.30	1947.90	94.29
Trial 20	3391.54	238.85	92.96
Trial 21	10674.30	712.47	93.32
Trial 22	4233.68	266.89	93.70
Trial 23	8330.47	571.03	93.14
Trial 24	4136.65	269.52	93.48
Trial 25	8765.49	585.87	93.32

simulation uses a wide workpiece and a radial depth of cut feed that alternates between a gradual slope into the workpiece and a constant depth of cut. The data from that simulation is used to create a relationship between the resultant aspects of the process (such as the cutting force) and the incremental depth of cut with respect to the previous cutting depth. From this, a limit is set to the cutting force, and a set of cutting depths is created so that the limit is not exceeded during cutting.

5.3.1 Gradual Radial Feed Simulation

For each pass in a typical power skiving process, a radial depth of cut is set (the incremental depth of cut Δd_j) which has a direct effect on the chip load and cutting forces present during cutting. However, the cutting behaviour is also influenced by the previous total depth of cut ($d_{0,j}$) achieved by the preceding passes. Combining the two results in a total depth of cut for a pass (d_j). Attempting to simulate each combination of incremental and total previous depth of cut for every pass in a power skiving process would take a prohibitively large amount of time.

A simulation approach was created to develop trends relating, for example, cutting force to the incremental and total cutting depths for a pass. Figure 5.5a shows that for a given depth of cut, the cutting tool is first fed in a "ramping" manner, meaning that the depth of cut is increased with the axial movement of the tool until the specified cutting depth is reached at the end of the axial stroke. The tool then performs a cutting pass at the same specified depth without the incremental feed (Figure 5.5b). Therefore, at each time step, the tool will be cutting at an incremental depth of cut, while the workpiece will have been cut to a given total depth. This method was termed a "ramp-in" simulation.

In this approach, each "pass" is considered as a pair of ramping-in and constant-depth passes and is set to have the same incremental cut depth for consistency. This depth is calculated using the required total cutting depth for the cutter-workpiece pair (d_t) and an integer number of passes (N_{pass}, generally selected to be between 6

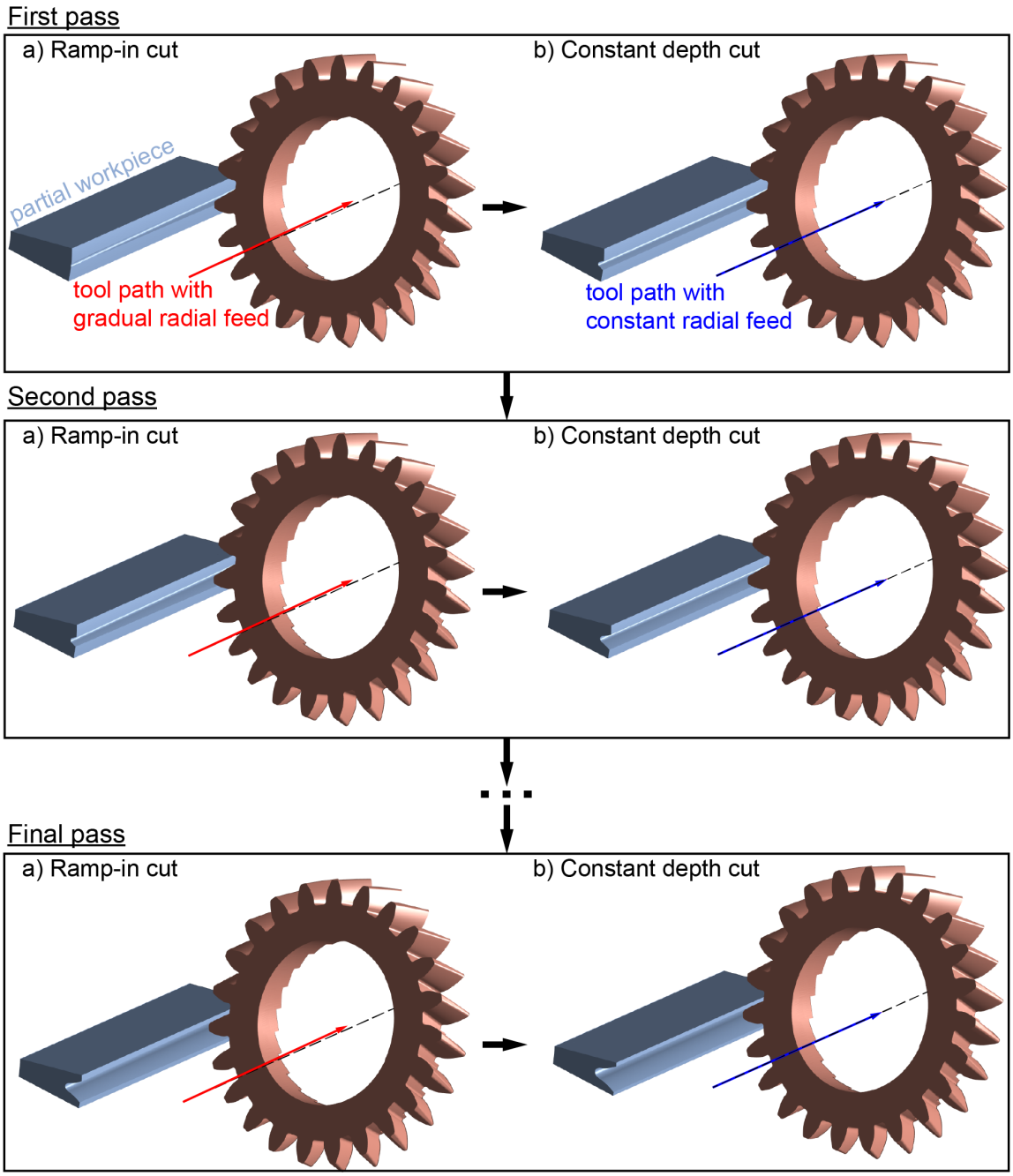

Figure 5.5: Radial feed scheme for process planning.

and 10) as follows:

$$\Delta d_j = \Delta d_{\text{ramp-in}} = \frac{d_t}{N_{\text{pass}}} \tag{5.5}$$

To reduce the effect of the incremental radial feed, a wide workpiece is used in the gradual radial feed simulations. To approximate a steady-state cut without the ramping movement by minimizing the influence of the radial feed, the angle between the ramp-in radial feed (or the incremental depth of cut for the current pass Δd_j) and the stroke length (L) of the pass is kept below 1°, as shown in the following equation:

$$\tan^{-1} \frac{\Delta d_j}{L} \leq 1^\circ \tag{5.6}$$

Since the workpiece is widened for this approach, there is an increased number of CWE calculations required to fully cut the workpiece in the virtual model. To reduce the time taken to perform the study, a partial workpiece is normally used for the simulation, as outlined in Section 5.2.

5.3.2 Interpretation of Results

The results generated from a simulation using the ramp-in radial cutting depth method are used to characterize the effect of the cutting depth on the cutting conditions for a given power skiving setup. Figure 5.6 demonstrates that the magnitude and rate of change of the total cutting force are both affected as the cutting depths are altered. For this study, the kinematic parameters from Trial 6 were used, with the total depth of cut of 9.36mm being divided into eight incremental cut depths for the ramp-in simulation.

The cutting force (and other) results from the ramp-in simulation can be plotted as a function of both the total preceding cut depth and the current incremental cut depth. Figure 5.7 shows an example three-dimensional plot of the total average cutting force with the two cutting depth parameters. It is clearly demonstrated that as the total depth of cut increases, the incremental cutting depth causes the total cutting force to increase more rapidly. This necessitates less aggressive cuts as the power skiving process proceeds.

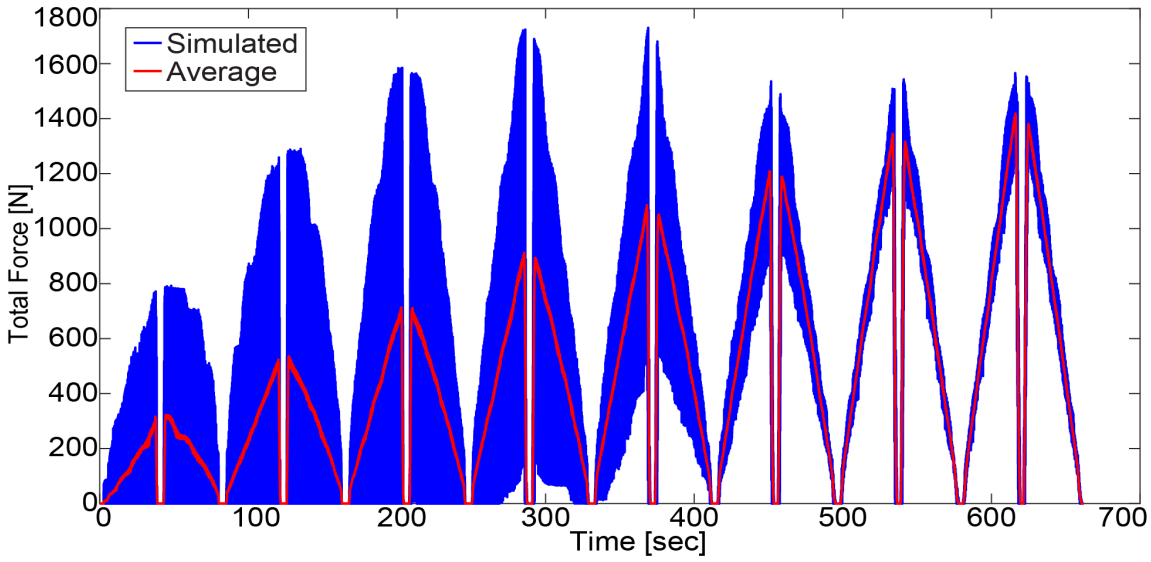

Figure 5.6: Total cutting force during ramp-in simulation.

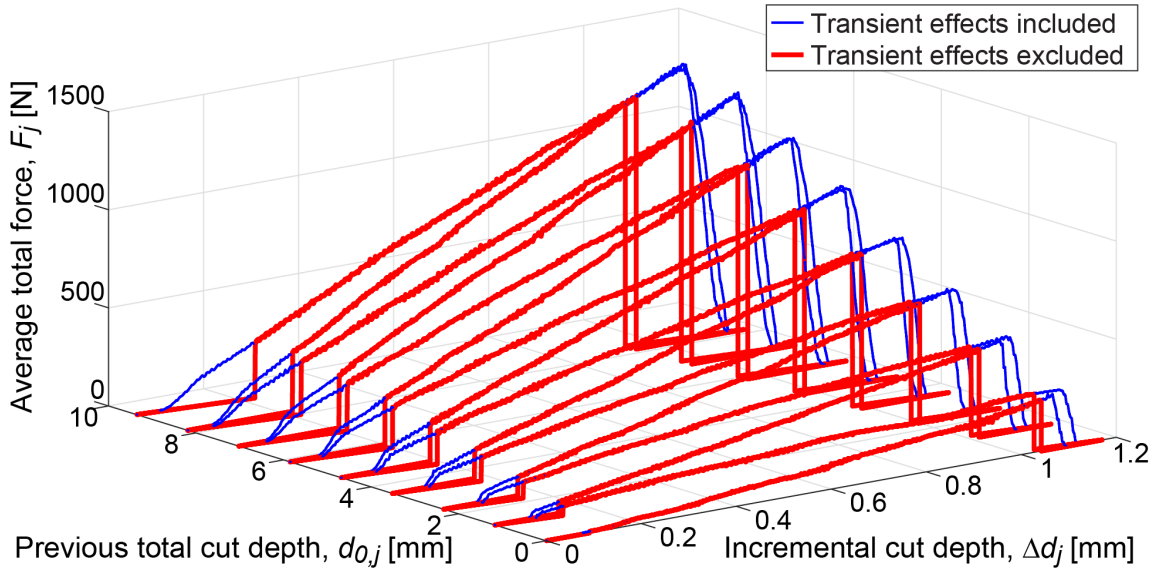

Figure 5.7: Average total cutting force results from process study.

Regions of transient cutting force behaviour occur at the start and end of the cutting during each pass, when the cutting tool is not fully engaged with the work-piece. For simplification, the analysis of the results considers only the regions where the cutter is fully engaged. A simplified equation for the axial movement needed for the tool to be fully engaged during a given pass is used:

$$z_e = \sqrt{r_{ac}^2 - (r_{ac} - d_{0,j})^2}\sin\Sigma \tag{5.7}$$

The data is only considered for cases where the tool is within the engagement position at the start and end of the cutting pass. Cutting force measurements for a given pass are therefore only taken for the following range of the tool's z-axis position:

$$z_e^- \leq z \leq z_e^+, \quad \text{where} \begin{cases} z_e^- = -w_g + z_e \\ z_e^+ = -z_e \end{cases} \tag{5.8}$$

The resulting data can be expressed as a function of only the incremental cutting depth, as shown in Figure 5.8, by separating the data by passes and assigning a single initial cutting depth to each. For the constant cutting depth passes, where the preceding cutting depth was not constant, the average initial cutting depth was used instead.

The results can be expressed in a more general form by selecting an appropriate fitting function that can estimate the data for each pass, and then solving for the fit coefficients for each pass. For the average total force, the fit of the data can assumed to be linear. For each pass, the ramp-in data and constant depth data is first fit separately. Coefficients for the ramp-in (A_j, B_j) and constant depth (C_j, D_j) data for each pass j in the ramp-in simulation can be established assuming the form:

$$\begin{aligned} F_j\left(\Delta d_j\right) &= A_j \Delta d_j + B_j, \quad \text{ramp-in data} \\ F_j\left(\Delta d_j\right) &= C_j \Delta d_j + D_j, \quad \text{constant depth data} \end{aligned} \tag{5.9}$$

Using least squares regression, the coefficients of the fitting function for the two parts of each pass can be solved, as seen in Figure 5.9. In the case of the linear fit

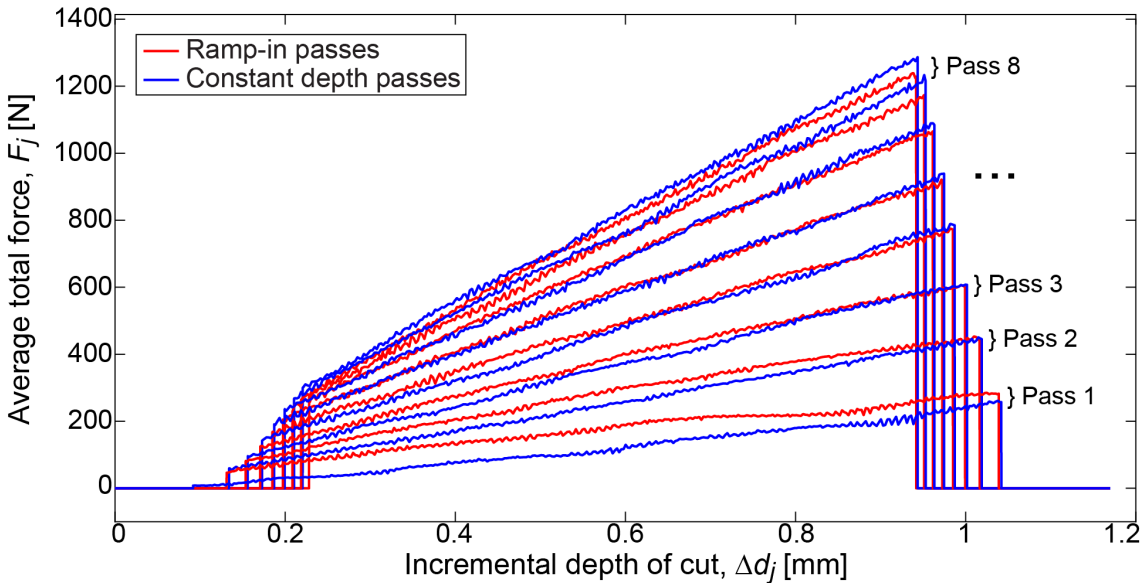

Figure 5.8: Average total cutting force as a function of incremental cutting depth.

for the average total cutting force, the solution is as follows:

$$\begin{bmatrix} A_j \\ B_j \end{bmatrix} = \text{pinv} \left\{ \begin{bmatrix} \Delta d_{1,j} & 1 \\ \Delta d_{2,j} & 1 \\ \vdots & \vdots \\ \Delta d_{n,j} & 1 \end{bmatrix} \right\} \begin{bmatrix} F_{1,j} \\ F_{2,j} \\ \vdots \\ F_{n,j} \end{bmatrix}, \quad \text{ramp-in data}$$
$$\begin{bmatrix} C_j \\ D_j \end{bmatrix} = \text{pinv} \left\{ \begin{bmatrix} \Delta d_{1,j} & 1 \\ \Delta d_{2,j} & 1 \\ \vdots & \vdots \\ \Delta d_{n,j} & 1 \end{bmatrix} \right\} \begin{bmatrix} F_{1,j} \\ F_{2,j} \\ \vdots \\ F_{n,j} \end{bmatrix}, \quad \text{ramp-in data} \tag{5.10}$$

As a result of the sloping radial feed during the ramp-in simulation, there is some discrepancy between the resulting cutting engagement and that of an average power skiving process with constant radial distances each pass. As a result, it is advantageous to create fit lines for each pass based on the average fit determined for each component of the pass. The average fitting coefficients for a given pass ($\bar{A}_j$ and $\bar{B}_j$) are calculated using the two sets of fit coefficients, and the average previous

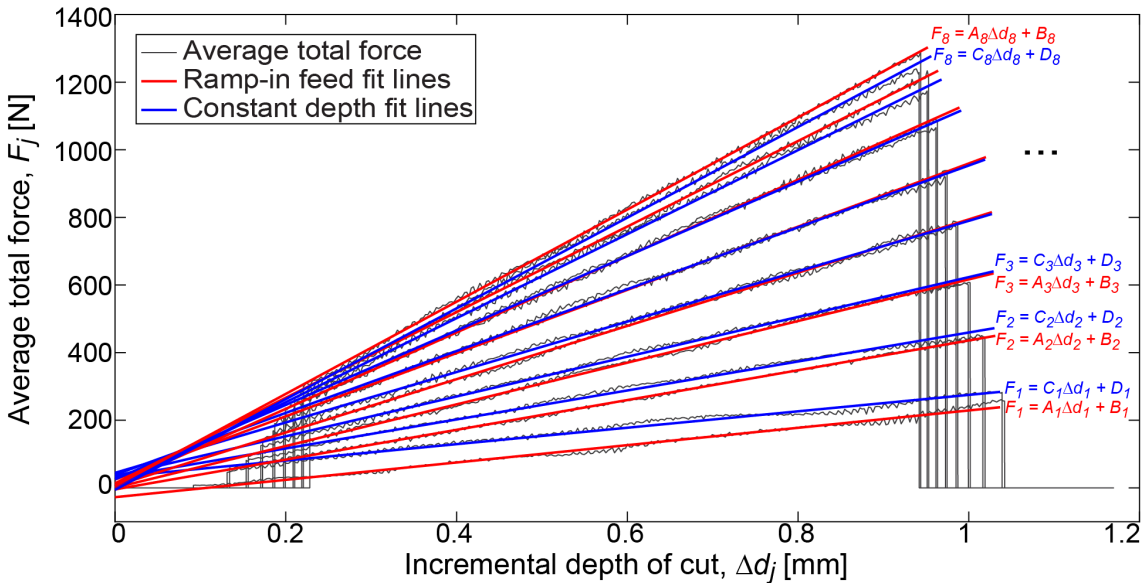

Figure 5.9: Linear fit of ramp-in and constant depth data.

cutting depth ($\Delta\bar{d}_j$) is based on the average previous cutting depth from the ramp-in and constant depth data as follows:

$$\bar{A}_j = \frac{A_j + C_j}{2}, \quad \bar{B}_j = \frac{B_j + D_j}{2}, \quad \Delta\bar{d}_j = \frac{\Delta d_{j,\text{ramp-in}} + \Delta d_{j,\text{const}}}{2} \tag{5.11}$$

The resulting average linear fits are shown in Figure 5.10. In comparison to the paired fits, they display much more consistent progression as the radial depth of cut increases, which is more suitable when used as the basis for planning processes.

5.3.3 Force-Limited Process Planning

The results from the ramp-in radial feed simulation have been used to plan power skiving processes with a limitation on the average total cutting force experienced by the cutter. This was motivated by observations made during testing that the traditionally planned processes (ie., processes planned using an iterative trial-and-error approach) showed a wide array in measured cutting forces associated with each pass (see Figure 5.11). The process was stable and effective at machining the gears;

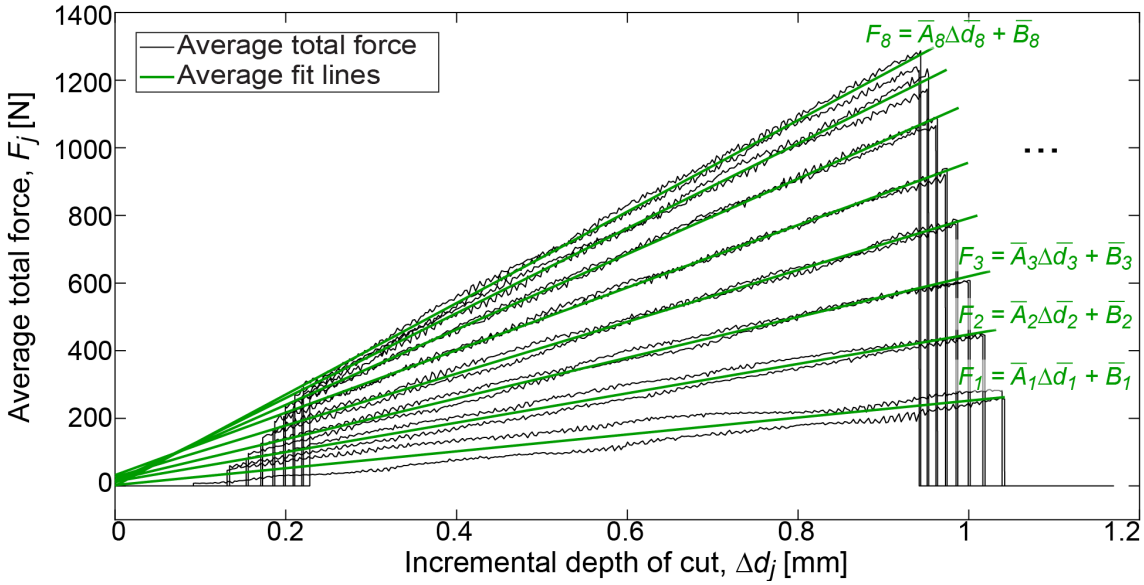

Figure 5.10: Average linear fits for ramp-in simulation data.

however, it was theorized that the high forces present in some of the passes could be the cause of premature tool wear. Therefore, in setting a limit on these forces, the tool would theoretically experience a more consistent load during each pass, thus reducing tool wear.

Figure 5.12 shows an overview of the method used to establish the cutting depths of the force-limited process. For each developed pass, the previous total cutting depth is unlikely to align with those created from the analysis of the ramp-in simulation. Therefore, a linear interpolation or extrapolation of the fit coefficients is used to generate new fit lines for each developed pass in order to find each incremental depth of cut for the target average total cutting force. First, the previous total depth of cut for the new pass is established by summing the incremental depths of cut from the previous passes (in other words, the total depth of cut of the previous pass d'_{k-1}):

$$d'_{0,k} = \Delta d'_1 + \Delta d'_2 + \cdots + \Delta d'_{k-1} = d'_{k-1} \tag{5.12}$$

The new previous depth value ($d'_{0,k}$) is used to create an associated fit line with new coefficients (A'_k and B'_k). To accomplish this, a consecutive pair of fit lines from

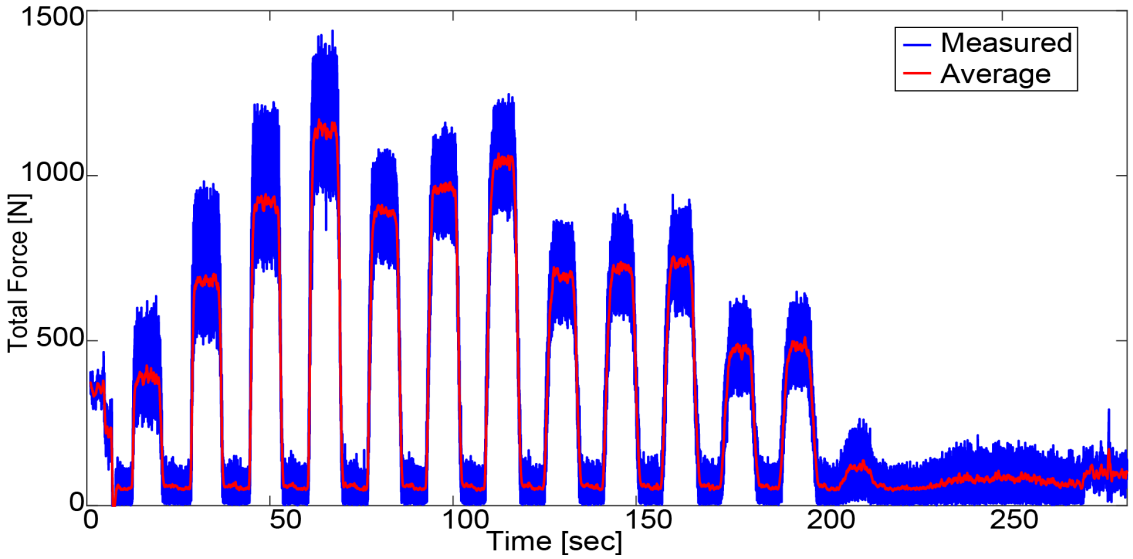

Figure 5.11: Total cutting force during a traditionally-planned process (Trial 6).

the ramp-in simulation are selected based on their previous total cutting depth values ($\bar{d}_{0,j}$, $\bar{d}_{0,j+1}$). The fit lines are selected if the value of $d'_{0,k}$ is between their respective d_0 values, where possible. If the new previous depth value is either less than or greater than all the d_0 values from the ramp-in simulation, then the first or last two fit lines are selected, respectively. The coefficients of the selected fitting lines ($\bar{A}_j$, $\bar{B}_j$ and $\bar{A}_{j+1}$, $\bar{B}_{j+1}$) are then used to develop a new theoretical fitting line with its own set of coefficients (A'_k and B'_k). This is done either through linear interpolation, if the new previous depth value falls between the previous depth values of the selected fitting lines, or through linear extrapolation otherwise:

$$\left.\begin{aligned} A'_k &= \bar{A}_j + \left(d'_{0,k} - \bar{d}_{0,j}\right) \frac{\bar{A}_{j+1} - \bar{A}_j}{\bar{d}_{0,j+1} - \bar{d}_{0,j}} \\ B'_k &= \bar{B}_j + \left(d'_{0,k} - \bar{d}_{0,j}\right) \frac{\bar{B}_{j+1} - \bar{B}_j}{\bar{d}_{0,j+1} - \bar{d}_{0,j}} \end{aligned}\right\}, \quad \text{where } \bar{d}_{0,j} < d'_{0,k} < \bar{d}_{0,j+1}$$

$$\left.\begin{aligned} A'_k &= \bar{A}_j + \left(\bar{A}_{j+1} - \bar{A}_j\right) \frac{d'_{0,k} - \bar{d}_{0,j}}{\bar{d}_{0,j+1} - \bar{d}_{0,j}} \\ B'_k &= \bar{B}_j + \left(\bar{B}_{j+1} - \bar{B}_j\right) \frac{d'_{0,k} - \bar{d}_{0,j}}{\bar{d}_{0,j+1} - \bar{d}_{0,j}} \end{aligned}\right\}, \quad \begin{aligned} &\text{where } d'_{0,k} < \bar{d}_{0,j} < \bar{d}_{0,j+1} \\ &\text{or where } \bar{d}_{0,j} < \bar{d}_{0,j+1} < d'_{0,k} \end{aligned} \tag{5.13}$$

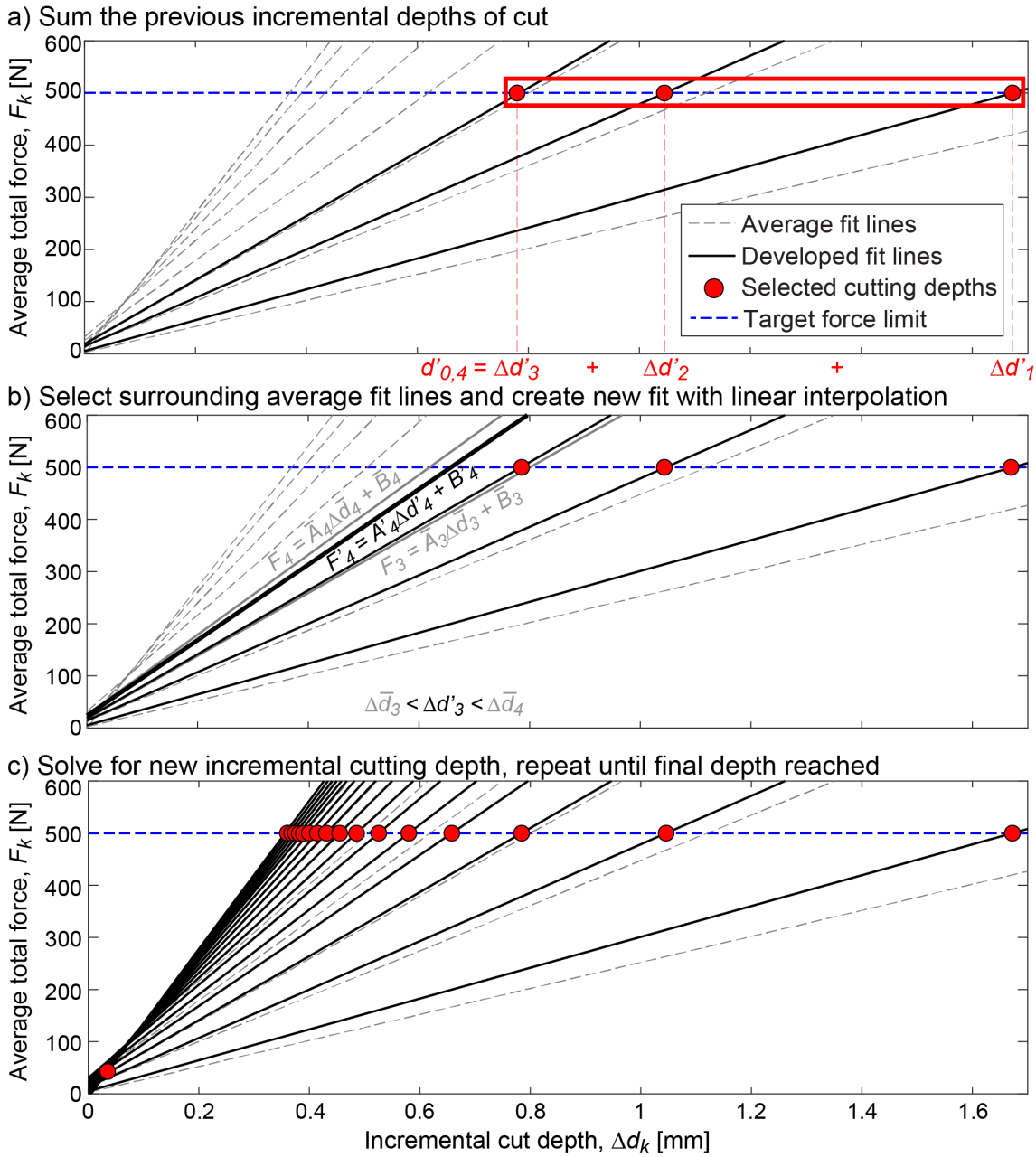

Figure 5.12: Procedure to develop a force-limited cutting scheme.

To plan the depths of cut for each pass of a force-limited trial, a target average total force must be chosen (F_{targ}). The incremental depth of cut for each new pass ($\Delta d'_k$) is found by using Equation (5.14) with the newly calculated fitting coefficients for the new pass.

$$\Delta d'_k = \frac{F_{\text{targ}} - B'_k}{A_k} \tag{5.14}$$

The total depth of cut is then calculated (d'_k) and used as the previous total depth of cut for a new pass ($d'_{0,k+1}$). The process for finding a new incremental depth of cut is then repeated until the full cutting depth for the gear is reached or exceeded. In the case of a pass that would exceed the total required cutting depth, the incremental depth is reduced accordingly.

While the method demonstrated for planning a process for a limited average total force, it can be used for any desired process limit, as long as a fit line can be generated for the relationship between the target parameter and the incremental depth of cut. In the case of multiple constraints, multiple incremental cutting depths are generated, and the smallest is chosen as the cutting depth of the pass.

5.3.4 Results

The process planning method outlined in this chapter was used to create the cutting depth schemes for experimental Trials 7–25 using various average total cutting force limits, as well as an additional cutting force per chip width constraint added for Trials 11–25. The cutting depths developed can be found in Tables A.3 and A.4 of Appendix A.

Figure 5.13 shows the measured total forces for Trial 8. The average total cutting force target when planning the process for the trial was set at 500N. As can be observed, the latter passes of the process have measured forces close to that of the target force, with the discrepancy likely being due to the measurement noise of the SPIKE system. However, the first three passes show an elevated total cutting force. This is due to an error in the original process planning code, which caused the first pass to be cut much more aggressively and ultimately resulted in excess

Table 5.4: Example limits used for process planning.

Trial	Limit(s)
7	400N avg. total force
8	500N avg. total force
9	600N avg. total force
10	700N avg. total force
11–19	500N avg. total force
	100N/mm force per chip width
20–25	700N avg. total force
	150N/mm force per chip width

total cutting force. This error has since been corrected. Disregarding that issue, the forces in Trial 8 are shown to be much more consistent compared to those of Trial 6 (see Figure 5.11), indicating the effectiveness of the process planning method. Furthermore, the planning process using the virtual model was performed in less than one hour, compared to the many hours of operator labour and material costs associated with traditional process planning methods for power skiving.

Figure 5.14 shows the measured total forces for Trial 20, which was planned with an average total force target of 700N. The process again shows consistent total force levels among passes. For the planning of this trial, an additional constraint of total force per chip width of 150N/mm was added. The constraint was added in response to the fact that, as the radial depths of cut for the passes increases, the width of the chip increases and the total force is dispersed across the cutting edge. It was theorized that the earlier passes were therefore overloading the tip of the cutting tool's teeth. The additional constraint is used to plan the process using the previously described method in parallel with the total force constraint. When planning the process, two incremental cuts for each pass are generated (one from each constraint) and the smaller incremental value is chosen. This methodology can also be used to add an arbitrary number of constraints, with the incremental depth of cut always being the minimum of the depths generated by each of the constraints.

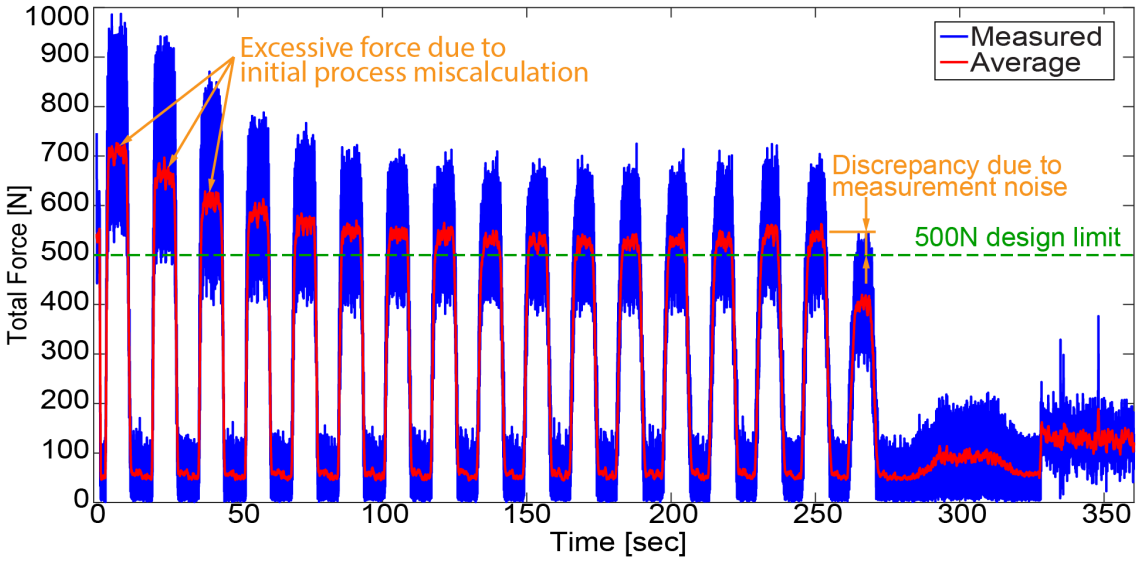

Figure 5.13: Total cutting force from planned force-limited processes (Trial 8).

It should be noted that the pass parameters for Trial 20 were designed with a cutting speed of 812rpm. However, during the experimental trials, it was found that this tool speed resulted in forced-vibration behaviour of the tool. The tool speed was increased to 957rpm to avoid inducing vibrations, and as a result the cutting forces measured were under the target set during the process planning phase.

5.4 Conclusions

The chapter presented the methodology with which process planning has been accomplished using the power skiving model. By reducing the simulation to only the partial workpiece and then reconstructing the cutting forces of a full workpiece simulation, a 93% reduction in total simulation time was achieved, while still accurately capturing the forces. This partial workpiece simulation has also been used to implement a ramp-in simulation, the results from which are used to plan the cutting depths for a power skiving process. The data is used to establish relationships between the incremental cutting depth and the average total force (and other process parameters)

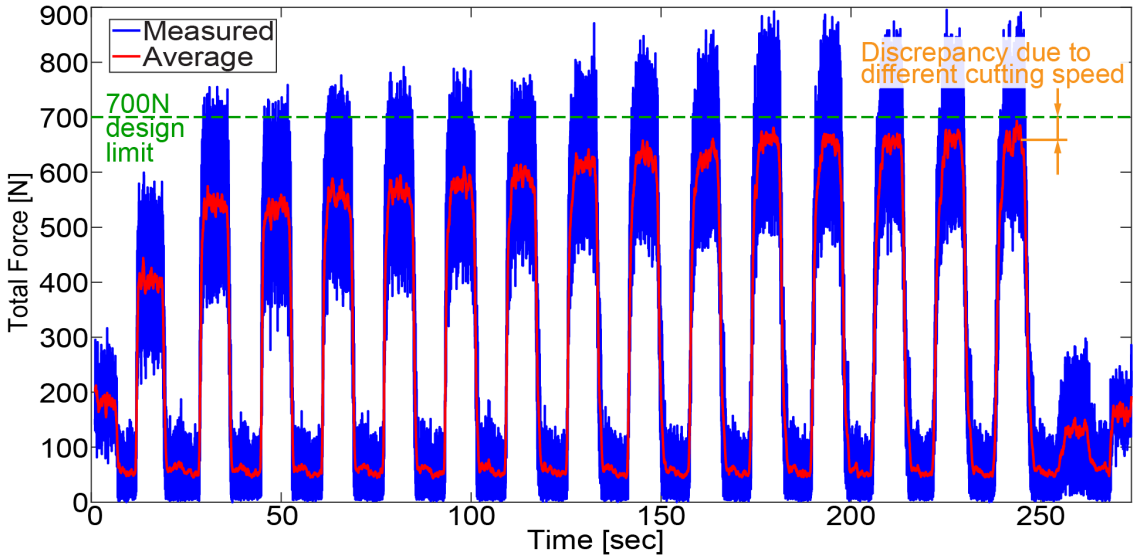

Figure 5.14: Total cutting force from planned force-limited processes with force-per-chip-width constraint (Trial 20).

which are based on the previous total cutting depth. The relationships are used to calculate new target cutting depths based on desired process limits. The processes developed using this method were successfully implemented during the experimental trials, and achieved much more consistent total cutting forces.

Chapter 6

Conclusions and Future Work

6.1 Conclusions

In this thesis, the successful development of a mechanistic model of power skiving is presented. The kinematics to describe the motion and cutting action of the tool-workpiece pair are developed, the relationship between the major coordinate systems is established, and the relative velocity of the cutting edge with respect to the workpiece is shown. From trials performed on a DMG NT5400 DCG mill-turn machine, the CNC tool position signals from the FANUC controller are compared to the simulated position for the same trial. It is found that, after accounting for differences in coordinate systems and for the return strokes that the virtual model's kinematics match that of the mill-turn machine.

The kinematics are used as a basis for predicting cutting forces. By integrating the kinematics into a multi-dexel-based CWE calculation engine, ModuleWorks, and simulating the modelled tool and workpiece movements in the WCS, the uncut chip geometry is extracted in dexel form. A point cloud created by intersecting the dexels and the developed outer contours with the rake geometry of the represented tool, and the 2D chip geometry is created using a Delaunay triangulation method with a modified alpha shape threshold on the point cloud. Nodes along the discretized cutting edge of the tool are then associated with the triangles closest to them to

calculate incremental chip geometry. Finally, by applying the oblique cutting model and the calculated cutting force coefficients to each node and summing the total, a cutting force prediction is made for each time step in a simulation. The measured and predicted cutting forces for a number of trials of the power skiving of a spur gear were compared, and for the Dathan tool cases where the tool geometry is known, the normalized RMS for the average forces match with 4–10% error, and for the peak forces within 10–15%. With the Sandvik tool, which has additional profile modifications, the error is around 6–9% for the average force, and 20–22% for the peak forces. Discrepancies between the measured and predicted forces are theorized to be caused by tool geometry adjustments by the manufacturers, the noise of the measurement system, and inexact force coefficients for the variation of local rake angles, inclination angles, and cutting speeds along the discretized cutting edge.

Finally, the model is extended to support the development of power skiving processes. First, a partial workpiece simulation method was developed in which a portion of the workpiece representing one tooth gap is machined. The cutting forces from this simulation are then used to predict the cutting forces of a full prediction using sample-to-sample linear mapping and superposition. This reduced simulation times by around 93–94% by making the model more computationally efficient, thus increasing the practicality of its use as a process planning tool. The reconstruction method resulted in $< 3\%$ discrepancy from the full simulation in cases where numerical precision was not a major factor of error. This partial simulation method was then used to incorporate a ramp-in radial feed simulation method, with alternating passes with gradual radial feeds and constant radial depths that developed a relationship between the average total cutting force, the incremental depth of cut of a pass, and the previous total depth of cut. This data is used to create multiple average fit lines associated with a particular previous depth of cut to correlate a new incremental depth of cut with an average total cutting force. Fit lines for any previous depth of cut can then be created through linear interpolation (or extrapolation, as necessary), and these lines are used to develop new power skiving processes by solving for incremental cutting depths with a target average total force. This methodology was successfully implemented to plan a number of processes which resulted in more

consistent total force readings. Trials 7–25 were all developed using this method of process planning.

6.2 Future Work

There are a number of areas in which the developed model can be extended as a part of future endeavours for simulating power skiving processes. Specifically, additional validation with measured cutting force data, the modelling of in-process tool deformation, the prediction of vibrations and stability, and further improvements to the process planning module are all potential subjects of future work in power skiving modelling.

In this thesis, validation is only presented for the case of machining an external spur gear, albeit using two different tools. To ensure the accuracy of the cutting force predictions for all cases, additional trials could be performed with internal gear geometry and helical gear geometry. Though the other gear cases are not anticipated to have a great influence on the efficacy of the mechanistic approach, the resultant change in the nature of the cutter-workpiece engagement may require adjustments to the model in order to correctly predict the cutting forces.

Future work will also include the modelling of static (or quasi-static) tool deflection during cutting. As of writing, the model is capable of simulating the deflection of the skiving tool due to forces when given modal data. These deflections are reflected in the final geometry of the workpiece, which will have form errors as a result. In order to validate the functionality of this module, however, the measured geometry of machined workpieces must be acquired for comparison purposes.

One of the most common difficulties in power skiving is creating a stable process with minimal vibrations. While a time-domain simulation with dynamic deflections and regenerating force as outlined by Smith and Tlusty [28] and Schmitz and Smith [128] could be implemented for skiving, it would be computationally expensive. Therefore, future work for vibrations and stability in skiving should be focused creating a more analytical method of predicting the stability of a given process.

Finally, the process planning presented in this thesis used a simplified method of establishing a force threshold. However, the optimization of a process for part quality, tool life, and speed is a much more nuanced area of study. Therefore, more work should be done to investigate the main parameters of interest and their ideal limits when planning a power skiving process.

References

[1] W. von Pittler, "Verfahren zum Schneiden von Zahnrädern mittels eines zahnradartigen, an den Stirnflächen der Zähne mit Schneidkanten versehenen Schneidwerkzeugs," German Patent 243 514, 1910.

[2] K.-D. Bouzakis, E. Lili, N. Michailidis, and O. Friderikos, "Manufacturing of cylindrical gears by generating cutting processes: A critical synthesis of analysis methods," *CIRP Annals*, vol. 57, no. 2, p. 676–696, 2008.

[3] O. Winkel, "Skiving^3 - The Liebherr Approach," in *7th WZL Gear Conference in the USA 2017*, July 2017.

[4] E. McClarence. (2016, Aug) Power skiving for greater productivity. Sankvik Coromant. [Online]. Available: https://www.sandvik.coromant.com/en-us/mww/pages/t_powerskiving.aspx

[5] 34 exclusive DMG MORI technology cycles. DMG MORI. [Online]. Available: https://ca-en.dmgmori.com/resource/blob/44740/7866e5623985b22298cfbf2f178e4988/ps0uk-dmg-mori-technology-cycles-pdf-data.pdf

[6] H. J. Stadtfeld, "Power skiving of cylindrical gears on different machine platforms," *Gear Technology*, pp. 52–62, Jan/Feb 2014.

[7] Y. Altintas, P. Kersting, D. Biermann, E. Budak, B. Denkena, and I. Lazoglu, "Virtual process systems for part machining operations," *CIRP Annals*, vol. 63, no. 2, p. 585–605, 2014.

[8] B. Schleich, N. Anwer, L. Mathieu, and S. Wartzack, "Shaping the digital twin for design and production engineering," *CIRP Annals*, vol. 66, no. 1, p. 141–144, 2017.

[9] M. E. Merchant, "Mechanics of the metal cutting process. I. orthogonal cutting and a type 2 chip," *Journal of Applied Physics*, vol. 16, no. 5, p. 267–275, 1945.

[10] E. Budak, A. Y., and E. J. A. Armarego, "Prediction of milling force coefficients from orthogonal cutting data," *Journal of Manufacturing Science and Engineering*, vol. 118, no. 2, pp. 216–224, 1996.

[11] W. A. Kline, R. E. DeVor, and J. R. Lindberg, "The prediction of cutting forces in end milling with application to cornering cuts," *International Journal of Machine Tool Design and Research*, vol. 22, no. 1, p. 7–22, 1982.

[12] H.-Y. Feng and C.-H. Menq, "The prediction of cutting forces in the ball-end milling process — I. model formulation and model building procedure," *International Journal of Machine Tools and Manufacture*, vol. 34, no. 5, p. 697–710, 1994.

[13] P. Lee and Y. Altintaş, "Prediction of ball-end milling forces from orthogonal cutting data," *International Journal of Machine Tools and Manufacture*, vol. 36, no. 9, p. 1059–1072, 1996.

[14] A. Lamikiz, L. N. López De Lacalle, J. A. Sánchez, and M. A. Salgado, "Cutting force integration at the cam stage in the high-speed milling of complex surfaces," *International Journal of Computer Integrated Manufacturing*, vol. 18, no. 7, p. 586–600, 2005.

[15] H. J. Fu, R. E. DeVor, and S. G. Kapoor, "A mechanistic model for the prediction of the force system in face milling operations," *Journal of Engineering for Industry*, vol. 106, no. 1, p. 81, 1984.

[16] D. A. Stephenson and J. S. Agapiou, "Calculation of main cutting edge forces and torque for drills with arbitrary point geometries," *International Journal of Machine Tools and Manufacture*, vol. 32, no. 4, p. 521–538, 1992.

[17] V. Chandrasekharan, S. G. Kapoor, and R. E. DeVor, "A mechanistic approach to predicting the cutting forces in drilling: With application to fiber-reinforced composite materials," *Journal of Engineering for Industry*, vol. 117, no. 4, pp. 559–570, 1995.

[18] E. Armarego and P. Samaranayake, "Performance prediction models for turning with rounded corner plane faced lathe tools. I. theoretical development," *Machining Science and Technology*, vol. 3, no. 2, p. 143–172, 1999.

[19] R. G. Reddy, S. G. Kapoor, and R. E. DeVor, "A mechanistic force model for contour turning," *Journal of Manufacturing Science and Engineering*, vol. 122, no. 3, pp. 398–405, 2000.

[20] F. Atabey, I. Lazoglu, and Y. Altintas, "Mechanics of boring processes – part I," *International Journal of Machine Tools and Manufacture*, vol. 43, pp. 463–476, 2003.

[21] M. Kaymakci, Z. M. Kilic, and Y. Altintas, "Unified cutting force model for turning, boring, drilling and milling operations," *International Journal of Machine Tools and Manufacture*, vol. 54-55, p. 34–45, 2012.

[22] M. R. Khoshdarregi and Y. Altintas, "Generalized modeling of chip geometry and cutting forces in multi-point thread turning," *International Journal of Machine Tools and Manufacture*, vol. 98, p. 21–32, 2015.

[23] O. M. Ozturk, Z. M. Kilic, and Y. Altintas, "Mechanics and dynamics of orbital drilling operations," *International Journal of Machine Tools and Manufacture*, vol. 129, p. 37–47, 2018.

[24] E. Ozturk and E. Budak, "Modeling of 5-axis milling processes," *Machining Science and Technology*, vol. 11, pp. 287–311, October 2007.

[25] A. Comak and Y. Altintas, "Mechanics of turn-milling operations," *International Journal of Machine Tools and Manufacture*, vol. 121, p. 2–9, 2017.

[26] J. W. Sutherland and R. E. DeVor, "An improved method for cutting force and surface error prediction in flexible end milling systems," *Journal of Engineering for Industry*, vol. 108, no. 4, p. 269–279, 1986.

[27] E. J. A. Armarego and N. P. Deshpande, "Computerized end-milling force predictions with cutting models allowing for eccentricity and cutter deflections," *CIRP Annals*, vol. 40, no. 1, p. 25–29, 1991.

[28] S. Smith and J. Tlusty, "An overview of modeling and simulation of the milling process," *Journal of Engineering for Industry*, vol. 113, no. 2, p. 169, 1991.

[29] E. Budak and Y. Altintas, "Peripheral milling conditions for improved dimensional accuracy," *International Journal of Machine Tools and Manufacture*, vol. 34, no. 7, p. 907–918, 1994.

[30] Y. Altintas, D. Montgomery, and E. Budak, "Dynamic peripheral milling of flexible structures," *Journal of Engineering for Industry*, vol. 114, pp. 137–145, 1992.

[31] E. Budak and Y. Altintas, "Analytical prediction of chatter stability in milling—part I: General formulation," *Journal of Dynamic Systems, Measurement, and Control*, vol. 120, pp. 22–30, March 1998.

[32] S. Tobias, *"Machine Tool Vibrations"*. J. Wiley, 1965.

[33] J. Tlusty and F. Ismail, "Special aspects of chatter in milling," *Journal of Vibration Acoustics Stress and Reliability in Design*, vol. 105, no. 1, p. 24–32, 1983.

[34] J. Tlusty, W. Zaton, and F. Ismail, "Stability lobes in milling," *CIRP Annals*, vol. 32, no. 1, p. 309–313, 1983.

[35] Y. Altintas and E. Budak, "Analytical prediction of stability lobes in milling," *CIRP Annals*, vol. 44, no. 1, p. 357–362, 1995.

[36] Y. Altintas and P. Lee, "A general mechanics and dynamics model for helical end mills," *CIRP Annals*, vol. 45, no. 1, p. 59–64, 1996.

[37] Y. Altıntass, E. Shamoto, P. Lee, and E. Budak, "Analytical prediction of stability lobes in ball end milling," *Journal of Manufacturing Science and Engineering*, vol. 121, no. 4, p. 586–592, 1999.

[38] Y. Altintas and S. Engin, "Generalized modeling of mechanics and dynamics of milling cutters," *CIRP Annals*, vol. 50, no. 1, p. 25–30, 2001.

[39] J. C. Roukema and Y. Altintas, "Generalized modeling of drilling vibrations. part I: Time domain model of drilling kinematics, dynamics and hole formation," *International Journal of Machine Tools and Manufacture*, vol. 47, no. 9, p. 1455–1473, 2007.

[40] E. Ozlu and E. Budak, "Analytical modeling of chatter stability in turning and boring operations—part I: Model development," *Journal of Manufacturing Science and Engineering*, vol. 129, no. 4, p. 726–732, 2007.

[41] A. Comak and Y. Altintas, "Dynamics and stability of turn-milling operations with varying time delay in discrete time domain," *Journal of Manufacturing Science and Engineering*, vol. 140, no. 10, pp. 101 013–1–101 013–14, 2018.

[42] M. R. Khoshdarregi and Y. Altintas, "Dynamics of multipoint thread turning—part I: General formulation," *Journal of Manufacturing Science and Engineering*, vol. 140, no. 6, pp. 061 003–1–061 003–11, 2018.

[43] I. Lazoglu, F. Atabey, and Y. Altintas, "Dynamics of boring processes: Part III-time domain modeling," *International Journal of Machine Tools and Manufacture*, vol. 42, no. 14, p. 1567–1576, 2002.

[44] Z. M. Kilic and Y. Altintas, "Generalized mechanics and dynamics of metal cutting operations for unified simulations," *International Journal of Machine Tools and Manufacture*, vol. 104, p. 1–13, 2016.

[45] S. D. Merdol and Y. Altintas, "Multi frequency solution of chatter stability for low immersion milling," *Journal of Manufacturing Science and Engineering*, vol. 126, no. 3, p. 459–466, 2004.

[46] C. Eksioglu, Z. M. Kilic, and Y. Altintas, "Discrete-time prediction of chatter stability, cutting forces, and surface location errors in flexible milling systems," *Journal of Manufacturing Science and Engineering*, vol. 134, no. 6, pp. 061 006–1–061 006–13, 2012.

[47] W. P. Wang and K. K. Wang, "Geometric modeling for swept volume of moving solids," *IEEE Computer Graphics and Applications*, vol. 6, no. 12, p. 8–17, 1986.

[48] A. Spence, Y. Altintas, and D. Kirkpatrick, "Direct calculation of machining parameters from a solid model," *Computers in Industry*, vol. 14, no. 4, p. 271–280, 1990.

[49] A. D. Spence and Y. Altintas, "A solid modeller based milling process simulation and planning system," *Journal of Engineering for Industry*, vol. 116, no. 1, p. 61–69, 1994.

[50] T. Surmann and D. Biermann, "The effect of tool vibrations on the flank surface created by peripheral milling," *CIRP Annals*, vol. 57, no. 1, p. 375–378, 2008.

[51] K. Weinert, P. Kersting, T. Surmann, and D. Biermann, "Modeling regenerative workpiece vibrations in five-axis milling," *Production Engineering*, vol. 2, no. 3, p. 255–260, 2008.

[52] B. M. Imani and M. A. Elbestawi, "Geometric simulation of ball-end milling operations," *Journal of Manufacturing Science and Engineering*, vol. 123, no. 2, p. 177–184, 2001.

[53] J. Limido, C. Espinosa, M. Salaün, and J. Lacome, "Sph method applied to high speed cutting modelling," *International Journal of Mechanical Sciences*, vol. 49, no. 7, p. 898–908, 2007.

[54] E. Budak, L. T. Tunç, S. Alan, and H. N. Özgüven, "Prediction of workpiece dynamics and its effects on chatter stability in milling," *CIRP Annals*, vol. 61, no. 1, p. 339–342, 2012.

[55] X. Jin and Y. Altintas, "Prediction of micro-milling forces with finite element method," *Journal of Materials Processing Technology*, vol. 212, no. 3, p. 542–552, 2012.

[56] P. Kersting and D. Biermann, "Modeling techniques for simulating workpiece deflections in nc milling," *CIRP Journal of Manufacturing Science and Technology*, vol. 7, no. 1, p. 48–54, 2014.

[57] G. M. Kim, P. J. Cho, and C. N. Chu, "Cutting force prediction of sculptured surface ball-end milling using z-map," *International Journal of Machine Tools and Manufacture*, vol. 40, no. 2, p. 277–291, 2000.

[58] S.-K. Lee and S.-L. Ko, "Development of simulation system for machining process using enhanced z map model," *Journal of Materials Processing Technology*, vol. 130-131, p. 608–617, 2002.

[59] B. K. Fussell, R. B. Jerard, and J. G. Hemmett, "Modeling of cutting geometry and forces for 5-axis sculptured surface machining," *Computer-Aided Design*, vol. 35, no. 4, p. 333–346, 2003.

[60] K. C. Hui, "Solid sweeping in image space—application in nc simulation," *The Visual Computer*, vol. 10, no. 6, p. 306–316, 1994.

[61] V. Boess, C. Ammermann, D. Niederwestberg, and B. Denkena, "Contact zone analysis based on multidexel workpiece model and detailed tool geometry representation," *Procedia CIRP*, vol. 4, p. 41–45, 2012.

[62] L. Berglind, D. Plakhotnik, and E. Ozturk, "Discrete cutting force model for 5-axis milling with arbitrary engagement and feed direction," *Procedia CIRP*, vol. 58, p. 445–450, 2017.

[63] A. M. Abood, "Dynamic analysis of the cutting forces in gear hobbing," Ph.D. dissertation, University of Newcastle upon Tyne, 2002.

[64] K.-D. Bouzakis, S. Kombogiannis, A. Antoniadis, and N. Vidakis, "Gear hobbing cutting process simulation and tool wear prediction models," *Journal of Manufacturing Science and Engineering*, vol. 124, no. 1, p. 42–51, 2002.

[65] M. Komori, M. Sumi, and A. Kubo, "Simulation of hobbing for analysis of cutting edge failure due to chip crush," *Gear Technology*, p. 64–69, 2004.

[66] K.-D. Bouzakis, O. Friderikos, and I. Tsiafis, "Fem-supported simulation of chip formation and flow in gear hobbing of spur and helical gears," *CIRP Journal of Manufacturing Science and Technology*, vol. 1, no. 1, p. 18–26, 2008.

[67] N. Tapoglou and A. Antoniadis, "Hob3d: A novel gear hobbing simulation software," in *Proceedings of the World Congress on Engineering 2011*, vol. 1, 2011.

[68] X. Dong, C. Liao, Y. C. Shin, and H. H. Zhang, "Machinability improvement of gear hobbing via process simulation and tool wear predictions," *The International Journal of Advanced Manufacturing Technology*, vol. 86, no. 9-12, p. 2771–2779, 2016.

[69] F. Klocke, C. Gorgels, G.-T. Weber, and R. Schalaster, "Prognosis of the local tool wear in gear finish hobbing," *Production Engineering*, vol. 5, no. 6, p. 651–657, 2011.

[70] F. Klocke, C. Gorgels, R. Schalaster, and A. Stuckenberg, "An innovative way of designing gear hobbing processes," *Gear Technology*, p. 48–53, May 2012.

[71] F. Klocke, C. Brecher, C. Löpenhaus, and M. Krömer, "Calculating the workpiece quality using a hobbing simulation," *Procedia CIRP*, vol. 41, p. 687–691, 2016.

[72] F. Klocke, B. Döbbeler, S. Goetz, and T. D. Viek, "Model-based online tool monitoring for hobbing processes," *Procedia CIRP*, vol. 58, p. 601–606, 2017.

[73] K. Erkorkmaz, A. Katz, Y. Hosseinkhani, D. Plakhotnik, M. Stautner, and F. Ismail, "Chip geometry and cutting forces in gear shaping," *CIRP Annals*, vol. 65, no. 1, p. 133–136, 2016.

[74] A. Katz, K. Erkorkmaz, and F. Ismail, "Virtual model of gear shaping—part i: Kinematics, cutter–workpiece engagement, and cutting forces," *Journal of Manufacturing Science and Engineering*, vol. 140, no. 7, 2018.

[75] A. Katz, "Cutting mechanics of the gear shaping process," Master's thesis, University of Waterloo, 2017.

[76] A. Katz, K. Erkorkmaz, and F. Ismail, "Virtual model of gear shaping—part ii: Elastic deformations and virtual gear metrology," *Journal of Manufacturing Science and Engineering*, vol. 140, no. 7, 2018.

[77] F. Klocke, M. Brumm, and J. Reimann, "Modeling of surface zone influences in generating gear grinding," *Procedia CIRP*, vol. 8, p. 21–26, 2013.

[78] C. Brecher, M. Brumm, and F. Hübner, "Approach for the calculation of cutting forces in generating gear grinding," *Procedia CIRP*, vol. 33, p. 287–292, 2015.

[79] F. Hübner, F. Klocke, C. Brecher, and C. Löpenhaus, "Development of a cutting force model for generating gear grinding," *Volume 10: ASME 2015 Power Transmission and Gearing Conference; 23rd Reliability, Stress Analysis, and Failure Prevention Conference*, 2015.

[80] C. Brecher, T. Röthlingshöfer, and C. Gorgels, "Manufacturing simulation of beveloid gears for the use in a general tooth contact analysis software," *Production Engineering*, vol. 3, no. 1, p. 103–109, 2008.

[81] C. Brecher, F. Klocke, C. Gorgels, and A. Hardjosuwito, "Manufacturing simulation of bevel gear cutting - simulation based approach for tool wear analysis," *Proceedings of 1st International Conference on Simulation and Modeling Methodologies, Technologies and Applications*, p. 513–520, 2011.

[82] C. Brecher, F. Klocke, M. Brumm, and A. Hardjosuwito, "Simulation based model for tool life prediction in bevel gear cutting," *Production Engineering*, vol. 7, no. 2-3, p. 223–231, Dec 2012.

[83] J. W. Sutherland, E. J. Salisbury, and F. W. Hoge, "A model for the cutting force system in the gear broaching process," *International Journal of Machine Tools and Manufacture*, vol. 37, no. 10, pp. 1409–1421, 1997.

[84] F. Klocke and S. Tobias, "Gear shaving: Simulation and technological studies," *Volume 4: 9th International Power Transmission and Gearing Conference, Parts A and B*, 2003.

[85] M. Svahn, C. Andersson, and L. Vedmar, "Prediction and experimental verification of the cutting forces in gear form milling," *The International Journal of Advanced Manufacturing Technology*, vol. 82, no. 1-4, p. 111–121, 2015.

[86] M. Habibi and Z. C. Chen, "An accurate and efficient approach to undeformed chip geometry in face-hobbing and its application in cutting force prediction," *Journal of Mechanical Design*, vol. 138, no. 2, pp. 023 302–1–023 302–11, 2015.

[87] T. Bergs, "Cutting force model for gear honing," *CIRP Annals*, vol. 67, no. 1, p. 53–56, 2018.

[88] E. Guo, R. Hong, X. Huang, and C. Fang, "Research on the design of skiving tool for machining involute gears," *Journal of Mechanical Science and Technology*, vol. 28, no. 12, p. 5107–5115, 2014.

[89] ——, "A correction method for power skiving of cylindrical gears lead modification," *Journal of Mechanical Science and Technology*, vol. 29, no. 10, p. 4379–4386, 2015.

[90] Z. Guo, S.-M. Mao, X.-E. Li, and Z.-Y. Ren, "Research on the theoretical tooth profile errors of gears machined by skiving," *Mechanism and Machine Theory*, vol. 97, p. 1–11, 2016.

[91] Y.-P. Shih and Y.-J. Li, "A novel method for producing a conical skiving tool with error-free flank faces for internal gear manufacture," *Journal of Mechanical Design*, vol. 140, no. 4, p. 043302, 2018.

[92] C.-Y. Tsai, "Mathematical model for design and analysis of power skiving tool for involute gear cutting," *Mechanism and Machine Theory*, vol. 101, p. 195–208, 2016.

[93] F. Zheng, M. Zhang, W. Zhang, and X. Guo, "Research on the tooth modification in gear skiving," *Journal of Mechanical Design*, vol. 140, no. 8, p. 084502, 2018.

[94] Z. Guo, S.-M. Mao, X.-F. Du, and Z.-Y. Ren, "Influences of tool setting errors on gear skiving accuracy," *The International Journal of Advanced Manufacturing Technology*, vol. 91, no. 9-12, p. 3135–3143, 2017.

[95] T. Tachikawa, N. Kurita, M. Nakamura, D. Iba, and I. Moriwaki, "Calculation model for internal gear skiving with a pinion-type cutter having pitch deviation and a run-out," *Volume 10: ASME 2015 Power Transmission and Gearing Conference; 23rd Reliability, Stress Analysis, and Failure Prevention Conference*, 2015.

[96] M. Kojima and K. Nishijima, "Gear skiving of involute internal spur gear : (part 1. on the tooth profile)," *Bulletin of JSME*, vol. 17, no. 106, p. 511–518, Apr 1974.

[97] C.-Y. Tsai and P. D. Lin, "Gear manufacturing using power-skiving method on six-axis cnc turn-mill machining center," *The International Journal of Advanced Manufacturing Technology*, vol. 95, no. 1-4, p. 609–623, 2017.

[98] Z. Guo, S.-M. Mao, L. Huyan, and D.-S. Duan, "Research and improvement of the cutting performance of skiving tool," *Mechanism and Machine Theory*, vol. 120, p. 302–313, 2018.

[99] I. Moriwaki, T. Osafune, M. Nakamura, M. Funamoto, K. Uriu, T. Murakami, E. Nagata, N. Kurita, T. Tachikawa, Y. Kobayashi, and et al., "Cutting tool parameters of cylindrical skiving cutter with sharpening angle for internal gears," *Journal of Mechanical Design*, vol. 139, no. 3, p. 033301, 2017.

[100] K. Uriu, T. Osafune, T. Murakami, M. Nakamura, D. Iba, M. Funamoto, and I. Moriwaki, "Effects of shaft angle on cutting tool parameters in internal gear skiving," *Journal of Mechanical Science and Technology*, vol. 31, no. 12, p. 5665–5673, 2017.

[101] E. Guo, R. Hong, X. Huang, and C. Fang, "Research on the cutting mechanism of cylindrical gear power skiving," *The International Journal of Advanced Manufacturing Technology*, vol. 79, no. 1-4, p. 541–550, 2015.

[102] E. K. Guo, R. J. Hong, X. D. Huang, and C. G. Fang, "Power skiving process for cylindrical gears manufacturing," *Applied Mechanics and Materials*, vol. 799-800, p. 382–387, 2015.

[103] V. Schulze, C. Kühlewein, and H. Autenrieth, "3d-fem modeling of gear skiving to investigate kinematics and chip formation mechanisms," *Advanced Materials Research*, vol. 223, p. 46–55, 2011.

[104] S. Kimme, R. Bauer, W.-G. Drossel, and M. Putz, "Simulation of error-prone continuous generating production processes of helical gears and the influence on the vibration excitation in gear mesh," *Procedia CIRP*, vol. 62, p. 256–261, 2017.

[105] N. Tapoglou, "Calculation of non-deformed chip and gear geometry in power skiving using a cad-based simulation," *The International Journal of Advanced Manufacturing Technology*, 2018.

[106] D. Spath and A. Hühsam, "Skiving for high-performance machining of periodic structures," *CIRP Annals*, vol. 51, no. 1, p. 91–94, 2002.

[107] T. Tachikawa, D. Iba, N. Kurita, M. Nakamura, and I. Moriwaki, "Basic study on calculation of cutting forces useful for reducing vibration in skiving," *Journal of Mechanical Design*, vol. 139, no. 10, p. 104501, 2017.

[108] F. Klocke, C. Brecher, C. Löpenhaus, P. Ganser, J. Staudt, and M. Krömer, "Technological and simulative analysis of power skiving," *Procedia CIRP*, vol. 50, p. 773–778, 2016.

[109] L. F. Lvovic and A. Fuentes, *Gear geometry and applied theory.* Cambridge University Press, 2011.

[110] *ISO 53:1998, Cylindrical gears for general and heavy engineering – Standard basic rack tooth profile*, International Organization for Standardization Std., 1998.

[111] Power skiving tools. Gleason Corporation. [Online]. Available: https://www.gleason.com/en/products/tools/cylindrical/power-skiving/power-skiving-tools

[112] NT 5400 DCG. DMG Mori. [Online]. Available: https://ca-en.dmgmori.com/products/machines/turning/turn-mill/nt/nt-5400-dcg

[113] Y. Altintas, *"Manufacturing Automation, Second Edition".* Cambridge University Press, 2012.

[114] E. J. A. Armarego and R. C. Whitfield, "Computer based modelling of popular machining operations for force and power prediction," *CIRP Annals*, vol. 34, no. 1, p. 65–69, 1985.

[115] G. V. Stabler, "The chip flow law and its consequences," *Proceedings of 5th Machine Tool Design and Research Conference*, pp. 243–251, 1964.

[116] O. Kienzle, "Die Bestimmung von Kräften und Leistungen an spänden Werkzeugen und Werkzeugmaschinen," in *Z-VDI 94*, 1951.

[117] ModuleWorks GmbH. ModuleWorks GmbH. [Online]. Available: https://www.moduleworks.com/

[118] T. Van Hook, "Real-time shaded nc milling display," in *Proceedings of the 13th annual conference on Computer graphics and interactive techniques - SIGGRAPH 86*, vol. 20, no. 4, Aug 1986, p. 15–20.

[119] M. O. Benouamer and D. Michelucci, "Bridging the gap between csg and brep via a triple ray representation," in *Proceedings of the fourth ACM symposium on Solid modeling and applications - SMA 97*, 1997, p. 68–79.

[120] E. W. Weisstein. Newton's method. MathWorld – A Wolfram Alpha Resource. [Online]. Available: http://mathworld.wolfram.com/NewtonsMethod.html

[121] E. Gullotti. (2015) Line-cone intersection. Illusion Catalyst. [Online]. Available: http://www.illusioncatalyst.com/notes_files/mathematics/line_cone_intersection.php

[122] W. Zhang and M. C. Leu, "Surface reconstruction using dexel data from three sets of orthogonal rays," *Journal of Computing and Information Science in Engineering*, vol. 9, pp. 011 008–1–011 008–12.

[123] H. Edelsbrunner, D. G. Kirkpatrick, and R. Seidel, "On the shape of a set of points in the plane," *IEEE Transactions on Information Theory*, vol. 29, no. 4, pp. 551–559, July 1983.

[124] E. W. Weisstein. Circumcircle. MathWorld – A Wolfram Alpha Resource. [Online]. Available: http://mathworld.wolfram.com/Circumcircle.html

[125] D. F. Watson, "Computing the n-dimensional Delaunay tessellation with application to Voronoi polytopes," *The Computer Journal*, vol. 24, no. 2, pp. 167–172, 1981.

[126] E. W. Weisstein. Heron's formula. MathWorld – A Wolfram Alpha Resource. [Online]. Available: http://mathworld.wolfram.com/HeronsFormula.html

[127] CutPro Simulation Software. Manufacturing Automation Laboratories. [Online]. Available: https://www.malinc.com/products/cutpro/

[128] T. L. Schmitz and K. S. Smith, *Machining Dynamics: Frequency Response to Improved Productivity*. Springer, 2019.

Appendix A

Summary of Experimental Trial Parameters

Table A.1: Workpiece parameters for power skiving trials.

Parameter	Value
Normal module m_n [mm]	3.9
No. of teeth	29
Addendum diameter d_{ag} [mm]	120.9
Gear width b [mm]	22.75
Helix angle β_g [°]	0
Material	EN24T (AISI 4340) Steel

Table A.2: Tool parameters of experimental power skiving trials.

Parameter	Dathan Tool	Sandvik Tool
Number of teeth N_c	23	21
Module m_n [mm]	3.9	3.9
Pressure angle γ_n [°]	20	20
Helix angle β_c [°]	20	20
Addendum radius r_ac [mm]	106.377	93.82
Rake angle α_r [°]	5	10
Length on SPIKE l_t [mm]	196.085	200.593
Trials used	1–10	11–25
Material	HSS	HSS
Coating	Alcrona	Alcrona

Table A.3: Kinematic parameters of power skiving trials using Dathan tool.

Trial #	Pass #	Incr. cut depth Δd_i [mm]	Total cut depth d_i [mm]	Axial feed v_f $[\frac{\text{mm}}{\text{WPR}}]$	Tool speed ω_c [rpm]	Workpiece speed ω_g [rpm]
	1	0.80	0.80			
	2	0.80	1.60			
	3	0.80	2.40			
	4	0.80	3.20			
	5	0.60	3.80			
	6	0.60	4.40			
	7	0.60	5.00			
	8	0.60	5.60			
	9	0.40	6.00			
	10	0.40	6.40			
	11	0.40	6.80			
1	12	0.40	7.20	0.12	841.00	667.00
	13	0.30	7.50			
	14	0.30	7.80			
	15	0.30	8.10			
	16	0.30	8.40			
	17	0.20	8.60			
	18	0.20	8.80			
	19	0.20	9.00			
	20	0.20	9.20			
	21	0.10	9.30			
	22	0.03	9.33	0.12		
	23	0.03	9.36	0.07		

Table A.3: Dathan tool trial parameters (continued).

Trial #	Pass #	Δd_i [mm]	d_i [mm]	v_f [$\frac{\text{mm}}{\text{WPR}}$]	ω_c [rpm]	ω_g [rpm]
	1	0.80	0.80			
	2	0.80	1.60			
	3	0.80	2.40			
	4	0.80	3.20			
	5	0.60	3.80			
	6	0.60	4.40			
	7	0.60	5.00			
	8	0.60	5.60			
	9	0.40	6.00			
	10	0.40	6.40			
	11	0.40	6.80			
2	12	0.40	7.20	0.25	841.00	667.00
	13	0.30	7.50			
	14	0.30	7.80			
	15	0.30	8.10			
	16	0.30	8.40			
	17	0.20	8.60			
	18	0.20	8.80			
	19	0.20	9.00			
	20	0.20	9.20			
	21	0.10	9.30			
	22	0.03	9.33	0.12		
	23	0.03	9.36	0.07		

Table A.3: Dathan tool trial parameters (continued).

Trial #	Pass #	Δd_i [mm]	d_i [mm]	v_f [$\frac{\text{mm}}{\text{WPR}}$]	ω_c [rpm]	ω_g [rpm]
3	1	1.20	1.20	0.12	841.00	667.00
	2	1.20	2.40			
	3	1.20	3.60			
	4	1.20	4.80			
	5	0.80	5.60			
	6	0.80	6.40			
	7	0.80	7.20			
	8	0.50	7.70			
	9	0.50	8.20			
	10	0.50	8.70			
	11	0.30	9.00			
	12	0.30	9.30			
	13	0.03	9.33			
	14	0.03	9.36	0.07		
4	1	1.20	1.20	0.07	841.00	667.00
	2	1.20	2.40			
	3	1.20	3.60			
	4	1.20	4.80			
	5	0.80	5.60			
	6	0.80	6.40			
	7	0.80	7.20			
	8	0.50	7.70			
	9	0.50	8.20			
	10	0.50	8.70			
	11	0.30	9.00			
	12	0.30	9.30			
	13	0.03	9.33			
	14	0.03	9.36			

Table A.3: Dathan tool trial parameters (continued).

Trial #	Pass #	Δd_i [mm]	d_i [mm]	v_f [$\frac{\text{mm}}{\text{WPR}}$]	ω_c [rpm]	ω_g [rpm]
5	1	1.20	1.20	0.12	1073.00	851.00
	2	1.20	2.40			
	3	1.20	3.60			
	4	1.20	4.80			
	5	0.80	5.60			
	6	0.80	6.40			
	7	0.80	7.20			
	8	0.50	7.70			
	9	0.50	8.20			
	10	0.50	8.70			
	11	0.30	9.00			
	12	0.30	9.30			
	13	0.03	9.33			
	14	0.03	9.36	0.07		
6	1	1.20	1.20	0.25	841.00	667.00
	2	1.20	2.40			
	3	1.20	3.60			
	4	1.20	4.80			
	5	0.80	5.60			
	6	0.80	6.40			
	7	0.80	7.20			
	8	0.50	7.70			
	9	0.50	8.20			
	10	0.50	8.70			
	11	0.30	9.00			
	12	0.30	9.30			
	13	0.03	9.33	0.12		
	14	0.03	9.36	0.07		

Table A.3: Dathan tool trial parameters (continued).

Trial #	Pass #	Δd_i [mm]	d_i [mm]	v_f [$\frac{\text{mm}}{\text{WPR}}$]	ω_c [rpm]	ω_g [rpm]
	1	1.53	1.53			
	2	0.85	2.38			
	3	0.66	3.04			
	4	0.55	3.59			
	5	0.49	4.08			
	6	0.44	4.52			
	7	0.41	4.93			
	8	0.38	5.31			
	9	0.36	5.67			
	10	0.34	6.01			
	11	0.33	6.34			
7	12	0.32	6.66	0.25	841.00	667.00
	13	0.31	6.97			
	14	0.30	7.27			
	15	0.29	7.56			
	16	0.28	7.84			
	17	0.28	8.12			
	18	0.28	8.40			
	19	0.27	8.67			
	20	0.27	8.94			
	21	0.27	9.21			
	22	0.10	9.31			
	23	0.05	9.36	0.07		

Table A.3: Dathan tool trial parameters (continued).

Trial #	Pass #	Δd_i [mm]	d_i [mm]	v_f [$\frac{\text{mm}}{\text{WPR}}$]	ω_c [rpm]	ω_g [rpm]
8	1	1.80	1.80	0.25	841.00	667.00
	2	0.98	2.78			
	3	0.75	3.53			
	4	0.63	4.16			
	5	0.55	4.71			
	6	0.50	5.21			
	7	0.47	5.68			
	8	0.44	6.12			
	9	0.41	6.53			
	10	0.40	6.93			
	11	0.38	7.31			
	12	0.37	7.68			
	13	0.36	8.04			
	14	0.35	8.39			
	15	0.35	8.74			
	16	0.34	9.08			
	17	0.23	9.31			
	18	0.05	9.36	0.07		

Table A.3: Dathan tool trial parameters (continued).

Trial #	Pass #	Δd_i [mm]	d_i [mm]	v_f [$\frac{\text{mm}}{\text{WPR}}$]	ω_c [rpm]	ω_g [rpm]
9	1	2.16	2.16	0.25	841.00	667.00
	2	1.06	3.22			
	3	0.81	4.03			
	4	0.68	4.71			
	5	0.61	5.32			
	6	0.56	5.88			
	7	0.52	6.40			
	8	0.48	6.88			
	9	0.46	7.34			
	10	0.44	7.78			
	11	0.43	8.21			
	12	0.42	8.63			
	13	0.41	9.04			
	14	0.27	9.31			
	15	0.05	9.36	0.07		
10	1	2.53	2.53	0.25	841.00	667.00
	2	1.13	3.66			
	3	0.87	4.53			
	4	0.74	5.27			
	5	0.66	5.93			
	6	0.60	6.53			
	7	0.56	7.09			
	8	0.53	7.62			
	9	0.51	8.13			
	10	0.50	8.63			
	11	0.48	9.11			
	12	0.20	9.31			
	13	0.05	9.36	0.07		

Table A.4: Kinematic parameters of power skiving trials using Sandvik tool.

Trial #	Pass #	Incr. cut depth Δd_i [mm]	Total cut depth d_i [mm]	Axial feed v_f $[\frac{\text{mm}}{\text{WPR}}]$	Tool speed ω_c [rpm]	Workpiece speed ω_g [rpm]
11	1	0.69	0.69	0.25	812.00	588.00
	2	0.71	1.40			
	3	0.57	1.97			
	4	0.52	2.49			
	5	0.48	2.97			
	6	0.46	3.43			
	7	0.44	3.87			
	8	0.42	4.29			
	9	0.41	4.70			
	10	0.40	5.10			
	11	0.39	5.49			
	12	0.39	5.88			
	13	0.38	6.26			
	14	0.37	6.63			
	15	0.36	6.99			
	16	0.36	7.35			
	17	0.35	7.70			
	18	0.35	8.05			
	19	0.35	8.40			
	20	0.34	8.74			
	21	0.34	9.08			
	22	0.28	9.36			

Table A.4: Sandvik tool trial parameters (continued).

Trial #	Pass #	Δd_i [mm]	d_i [mm]	v_f [$\frac{\text{mm}}{\text{WPR}}$]	ω_c [rpm]	ω_g [rpm]
12	1	0.69	0.69	0.12	812.00	588.00
	2	0.71	1.40			
	3	0.57	1.97			
	4	0.52	2.49			
	5	0.48	2.97			
	6	0.46	3.43			
	7	0.44	3.87			
	8	0.42	4.29			
	9	0.41	4.70			
	10	0.40	5.10			
	11	0.39	5.49			
	12	0.39	5.88			
	13	0.38	6.26			
	14	0.37	6.63			
	15	0.36	6.99			
	16	0.36	7.35			
	17	0.35	7.70			
	18	0.35	8.05			
	19	0.35	8.40			
	20	0.34	8.74			
	21	0.34	9.08			
	22	0.28	9.36			

Table A.4: Sandvik tool trial parameters (continued).

Trial #	Pass #	Δd_i [mm]	d_i [mm]	v_f [$\frac{\text{mm}}{\text{WPR}}$]	ω_c [rpm]	ω_g [rpm]
13	1	0.69	0.69	0.07	812.00	588.00
	2	0.71	1.40			
	3	0.57	1.97			
	4	0.52	2.49			
	5	0.48	2.97			
	6	0.46	3.43			
	7	0.44	3.87			
	8	0.42	4.29			
	9	0.41	4.70			
	10	0.40	5.10			
	11	0.39	5.49			
	12	0.39	5.88			
	13	0.38	6.26			
	14	0.37	6.63			
	15	0.36	6.99			
	16	0.36	7.35			
	17	0.35	7.70			
	18	0.35	8.05			
	19	0.35	8.40			
	20	0.34	8.74			
	21	0.34	9.08			
	22	0.28	9.36			

Table A.4: Sandvik tool trial parameters (continued).

Trial #	Pass #	Δd_i [mm]	d_i [mm]	v_f [$\frac{\text{mm}}{\text{WPR}}$]	ω_c [rpm]	ω_g [rpm]
14	1	0.69	0.69	0.25	957.00	683.00
	2	0.71	1.40			
	3	0.57	1.97			
	4	0.52	2.49			
	5	0.48	2.97			
	6	0.46	3.43			
	7	0.44	3.87			
	8	0.42	4.29			
	9	0.41	4.70			
	10	0.40	5.10			
	11	0.39	5.49			
	12	0.39	5.88			
	13	0.38	6.26			
	14	0.37	6.63			
	15	0.36	6.99			
	16	0.36	7.35			
	17	0.35	7.70			
	18	0.35	8.05			
	19	0.35	8.40			
	20	0.34	8.74			
	21	0.34	9.08			
	22	0.28	9.36			

Table A.4: Sandvik tool trial parameters (continued).

Trial #	Pass #	Δd_i [mm]	d_i [mm]	v_f [$\frac{\text{mm}}{\text{WPR}}$]	ω_c [rpm]	ω_g [rpm]
15	1	0.69	0.69	0.12	957.00	683.00
	2	0.71	1.40			
	3	0.57	1.97			
	4	0.52	2.49			
	5	0.48	2.97			
	6	0.46	3.43			
	7	0.44	3.87			
	8	0.42	4.29			
	9	0.41	4.70			
	10	0.40	5.10			
	11	0.39	5.49			
	12	0.39	5.88			
	13	0.38	6.26			
	14	0.37	6.63			
	15	0.36	6.99			
	16	0.36	7.35			
	17	0.35	7.70			
	18	0.35	8.05			
	19	0.35	8.40			
	20	0.34	8.74			
	21	0.34	9.08			
	22	0.28	9.36			

Table A.4: Sandvik tool trial parameters (continued).

Trial #	Pass #	Δd_i [mm]	d_i [mm]	v_f [$\frac{\text{mm}}{\text{WPR}}$]	ω_c [rpm]	ω_g [rpm]
16	1	0.69	0.69	0.07	957.00	683.00
	2	0.71	1.40			
	3	0.57	1.97			
	4	0.52	2.49			
	5	0.48	2.97			
	6	0.46	3.43			
	7	0.44	3.87			
	8	0.42	4.29			
	9	0.41	4.70			
	10	0.40	5.10			
	11	0.39	5.49			
	12	0.39	5.88			
	13	0.38	6.26			
	14	0.37	6.63			
	15	0.36	6.99			
	16	0.36	7.35			
	17	0.35	7.70			
	18	0.35	8.05			
	19	0.35	8.40			
	20	0.34	8.74			
	21	0.34	9.08			
	22	0.28	9.36			

Table A.4: Sandvik tool trial parameters (continued).

Trial #	Pass #	Δd_i [mm]	d_i [mm]	v_f [$\frac{\text{mm}}{\text{WPR}}$]	ω_c [rpm]	ω_g [rpm]
17	1	0.69	0.69	0.25	1102.00	798.00
	2	0.71	1.40			
	3	0.57	1.97			
	4	0.52	2.49			
	5	0.48	2.97			
	6	0.46	3.43			
	7	0.44	3.87			
	8	0.42	4.29			
	9	0.41	4.70			
	10	0.40	5.10			
	11	0.39	5.49			
	12	0.39	5.88			
	13	0.38	6.26			
	14	0.37	6.63			
	15	0.36	6.99			
	16	0.36	7.35			
	17	0.35	7.70			
	18	0.35	8.05			
	19	0.35	8.40			
	20	0.34	8.74			
	21	0.34	9.08			
	22	0.28	9.36			

Table A.4: Sandvik tool trial parameters (continued).

Trial #	Pass #	Δd_i [mm]	d_i [mm]	v_f [$\frac{\text{mm}}{\text{WPR}}$]	ω_c [rpm]	ω_g [rpm]
18	1	0.69	0.69	0.12	1102.00	798.00
	2	0.71	1.40			
	3	0.57	1.97			
	4	0.52	2.49			
	5	0.48	2.97			
	6	0.46	3.43			
	7	0.44	3.87			
	8	0.42	4.29			
	9	0.41	4.70			
	10	0.40	5.10			
	11	0.39	5.49			
	12	0.39	5.88			
	13	0.38	6.26			
	14	0.37	6.63			
	15	0.36	6.99			
	16	0.36	7.35			
	17	0.35	7.70			
	18	0.35	8.05			
	19	0.35	8.40			
	20	0.34	8.74			
	21	0.34	9.08			
	22	0.28	9.36			

Table A.4: Sandvik tool trial parameters (continued).

Trial #	Pass #	Δd_i [mm]	d_i [mm]	v_f [$\frac{\text{mm}}{\text{WPR}}$]	ω_c [rpm]	ω_g [rpm]
19	1	0.69	0.69	0.07	1102.00	798.00
	2	0.71	1.40			
	3	0.57	1.97			
	4	0.52	2.49			
	5	0.48	2.97			
	6	0.46	3.43			
	7	0.44	3.87			
	8	0.42	4.29			
	9	0.41	4.70			
	10	0.40	5.10			
	11	0.39	5.49			
	12	0.39	5.88			
	13	0.38	6.26			
	14	0.37	6.63			
	15	0.36	6.99			
	16	0.36	7.35			
	17	0.35	7.70			
	18	0.35	8.05			
	19	0.35	8.40			
	20	0.34	8.74			
	21	0.34	9.08			
	22	0.28	9.36			

Table A.4: Sandvik tool trial parameters (continued).

Trial #	Pass #	Δd_i [mm]	d_i [mm]	v_f [$\frac{\text{mm}}{\text{WPR}}$]	ω_c [rpm]	ω_g [rpm]
20	1	1.04	1.04	0.25	957.00	693.00
	2	0.93	1.97			
	3	0.75	2.72			
	4	0.67	3.39			
	5	0.63	4.02			
	6	0.60	4.62			
	7	0.57	5.19			
	8	0.56	5.75			
	9	0.54	6.29			
	10	0.53	6.81			
	11	0.51	7.33			
	12	0.50	7.83			
	13	0.50	8.33			
	14	0.49	8.82			
	15	0.48	9.30			
	16	0.06	9.36			

Table A.4: Sandvik tool trial parameters (continued).

Trial #	Pass #	Δd_i [mm]	d_i [mm]	v_f [$\frac{\text{mm}}{\text{WPR}}$]	ω_c [rpm]	ω_g [rpm]
21	1	1.04	1.04	0.12	957.00	693.00
	2	0.93	1.97			
	3	0.75	2.72			
	4	0.67	3.39			
	5	0.63	4.02			
	6	0.60	4.62			
	7	0.57	5.19			
	8	0.56	5.75			
	9	0.54	6.29			
	10	0.53	6.81			
	11	0.51	7.33			
	12	0.50	7.83			
	13	0.50	8.33			
	14	0.49	8.82			
	15	0.48	9.30			
	16	0.06	9.36			

Table A.4: Sandvik tool trial parameters (continued).

Trial #	Pass #	Δd_i [mm]	d_i [mm]	v_f [$\frac{\text{mm}}{\text{WPR}}$]	ω_c [rpm]	ω_g [rpm]
22	1	1.04	1.04	0.25	1479.00	1071.00
	2	0.93	1.97			
	3	0.75	2.72			
	4	0.67	3.39			
	5	0.63	4.02			
	6	0.60	4.62			
	7	0.57	5.19			
	8	0.56	5.75			
	9	0.54	6.29			
	10	0.53	6.81			
	11	0.51	7.33			
	12	0.50	7.83			
	13	0.50	8.33			
	14	0.49	8.82			
	15	0.48	9.30			
	16	0.06	9.36			

Table A.4: Sandvik tool trial parameters (continued).

Trial #	Pass #	Δd_i [mm]	d_i [mm]	v_f [$\frac{\text{mm}}{\text{WPR}}$]	ω_c [rpm]	ω_g [rpm]
23	1	1.04	1.04	0.12	1479.00	1071.00
	2	0.93	1.97			
	3	0.75	2.72			
	4	0.67	3.39			
	5	0.63	4.02			
	6	0.60	4.62			
	7	0.57	5.19			
	8	0.56	5.75			
	9	0.54	6.29			
	10	0.53	6.81			
	11	0.51	7.33			
	12	0.50	7.83			
	13	0.50	8.33			
	14	0.49	8.82			
	15	0.48	9.30			
	16	0.06	9.36			

Table A.4: Sandvik tool trial parameters (continued).

Trial #	Pass #	Δd_i [mm]	d_i [mm]	v_f [$\frac{\text{mm}}{\text{WPR}}$]	ω_c [rpm]	ω_g [rpm]
24	1	1.04	1.04	0.25	2146.00	1554.00
	2	0.93	1.97			
	3	0.75	2.72			
	4	0.67	3.39			
	5	0.63	4.02			
	6	0.60	4.62			
	7	0.57	5.19			
	8	0.56	5.75			
	9	0.54	6.29			
	10	0.53	6.81			
	11	0.51	7.33			
	12	0.50	7.83			
	13	0.50	8.33			
	14	0.49	8.82			
	15	0.48	9.30			
	16	0.06	9.36			

Table A.4: Sandvik tool trial parameters (continued).

Trial #	Pass #	Δd_i [mm]	d_i [mm]	v_f [$\frac{\text{mm}}{\text{WPR}}$]	ω_c [rpm]	ω_g [rpm]
25	1	1.04	1.04	0.12	2146.00	1554.00
	2	0.93	1.97			
	3	0.75	2.72			
	4	0.67	3.39			
	5	0.63	4.02			
	6	0.60	4.62			
	7	0.57	5.19			
	8	0.56	5.75			
	9	0.54	6.29			
	10	0.53	6.81			
	11	0.51	7.33			
	12	0.50	7.83			
	13	0.50	8.33			
	14	0.49	8.82			
	15	0.48	9.30			
	16	0.06	9.36			